Plasma Assisted Ignition at High Pressures and Low Temperatures. PAI Kinetics and Fast Gas Heating

Dr. Svetlana Starikovskaya

Ecole Polytechnique
Laboratory for Plasma Physics
Route de Saclay
Palaiseau 91128 FRANCE

Report Date: May 2014

Final Report from 1 November 2009 to 31 October 2013

Air Force Research Laboratory
Air Force Office of Scientific Research
European Office of Aerospace Research and Development
Unit 4515, APO AE 09421-4515

96REPORT DOCUMENTATION PAGE	Form Approved OMB No. 0704-0188

1. REPORT DATE *(DD-MM-YYYY)*	2. REPORT TYPE	3. DATES COVERED *(From – To)*
6 May 2014	Final Report	1 November 2009 – 31 October 2013

4. TITLE AND SUBTITLE

Plasma Assisted Ignition at High Pressures and Low Temperatures. PAI Kinetics and Fast Gas Heating

5a. CONTRACT NUMBER

FA8655-10-1-3018

5b. GRANT NUMBER

Grant 10-3018

5c. PROGRAM ELEMENT NUMBER

61102F

6. AUTHOR(S)

Dr. Svetlana Starikovskaya

5d. PROJECT NUMBER

5d. TASK NUMBER

5e. WORK UNIT NUMBER

7. PERFORMING ORGANIZATION NAME(S) AND ADDRESS(ES)
Ecole Polytechnique
Laboratory for Plasma Physics
Route de Saclay
Palaiseau 91128 FRANCE

8. PERFORMING ORGANIZATION REPORT NUMBER

N/A

9. SPONSORING/MONITORING AGENCY NAME(S) AND ADDRESS(ES)

EOARD
Unit 4515
APO AE 09421-4515

10. SPONSOR/MONITOR'S ACRONYM(S)

AFRL/AFOSR/IOE (AFOSR)

11. SPONSOR/MONITOR'S REPORT NUMBER(S)

AFRL-AFOSR-UK-TR-2014-0013

12. DISTRIBUTION/AVAILABILITY STATEMENT

Distribution A: Approved for public release; distribution is unlimited.

13. SUPPLEMENTARY NOTES

14. ABSTRACT

This is the final report for this three year effort with the most important results presented herein. These are: (i) experiments and modeling of the fast gas heating at low (3–9 mbar) pressures at high reduced electric fields E/N = 200-400 and specific deposited energy up to 0.1 eV/molecule in synthetic air; (ii) experiments and modeling of the fast gas heating at moderate (up to 60 mbar) pressures at high electric fields and specific deposited energy more than 1 eV/molecule leading to dissociation degree up to 100%; (iii) experiments on measurements of a density of metastable N_2 molecules in the afterglow of the pulsed nanosecond discharge by technique of a cavity ring–down spectroscopy; (iv) experiments on electric field measurements in nanosecond high–voltage surface dielectric barrier discharge in air together with analysis of the combustion initiation by this type of discharge in $C_2H_6:O_2$ stoichiometric mixture at P = 1 atm.

15. SUBJECT TERMS

EOARD, ignition, Combustion, Plasma Combustion

16. SECURITY CLASSIFICATION OF:			17. LIMITATION OF ABSTRACT	18, NUMBER OF PAGES	19a. NAME OF RESPONSIBLE PERSON
a. REPORT UNCLAS	**b. ABSTRACT** UNCLAS	**c. THIS PAGE** UNCLAS	SAR	97	Gregg Abate
					19b. TELEPHONE NUMBER *(Include area code)* +44 (0)1895 616021

Standard Form 298 (Rev. 8/98)
Prescribed by ANSI Std. Z39-18

Plasma Assisted Ignition at High Pressures and Low Temperatures.
PAI Kinetics and Fast Gas Heating

PI: Dr. Svetlana STARIKOVSKAIA,
Laboratory for Plasma Physics (LPP), CNRS UMR 7648
Ecole Polytechnique
Route de Saclay, 91128 Palaiseau, France
Phone (+33)–1–69–33–59–45
E–mail: svetlana.starikovskaya@lpp.polytechnique.fr
URL: http://www.lpp.fr

Co–PI: Prof. Christophe LAUX,
Laboratoire d'Energtique Moleculaire et Macroscopique,
Combustion (EM2C), CNRS UPR 288, Ecole Centrale
Grande Voie des Vignes, 92290 Chatenay–Malabry, France
Phone: (+33)–1–41–13–10–44
E–mail: christophe.laux@em2c.ecp.fr
URL: http://www.em2c.ecp.fr

Contents

Chapter 1

Abstract

The most important results obtained during three years of the Project are presented in the Report, namely (i) experiments and modeling of the fast gas heating at low (3–9 mbar) pressures at high reduced electric fields $E/N = 200 - -400$ and specific deposited energy up to 0.1 eV/molecule in synthetic air; (ii) experiments and modeling of the fast gas heating at moderate (up to 60 mbar) pressures at high electric fields and and specific deposited energy more than 1 eV/molecule leading to dissociation degree up to 100%; (iii) experiments on measurements of a density of metastable $N_2(A^3\Sigma_u^+)$ molecules in the afterglow of the pulsed nanosecond discharge by technique of a cavity ring–down spectroscopy; (iv) experiments on electric field measurements in nanosecond high–voltage surface dielectric barrier discharge in air together with analysis of the combustion initiation by this type of discharge in C_2H_6:O_2 stoichiometric mixture at $P = 1$ atm.

Chapter 2

Fast gas heating in the afterglow of a volume nanosecond discharge at moderate pressures.

2.1 Introduction

So–called fast gas heating, which is the energy release in the discharge or post–discharge due to the relaxation of energy stored in electronic degrees of freedom and in ionization, has been investigated for decades. Interest in this phenomenon comes from the optimization of laser systems and chemical reactors: this type of energy release is important for governing the stable stage of self-sustained volume discharges as well as for the propagation of microwave discharges in electric fields below breakdown and so on. A kinetic mechanism describing fast gas heating has been suggested and verified [1] for pulsed discharges in air of duration 100 μs and more, current densities of $0.1 - 10$ A/cm^2, reduced electric fields less than 100 Td, gas pressures of $0.4 - 6$ Torr.

During the few last years, renewed interest in fast energy transfer from electronic degrees of freedom to gas heating is explained by plasma applications for combustion initiation [2] and flow control [3]-[5]. Indeed, to initiate the combustion process, it is necessary to provide an efficient dissociation and production of radicals, but it is also important to heat the gas as fast as possible to allow the chain reaction development [6, 7]. For plasma assisted aerodynamics, the efficiency of a concentrated heat release resulting in shock waves [4] or vortex [5] formation to rearrange the flow near the surface has been demonstrated by various authors.

The experimental evidence of a fast energy release has been demonstrated experimentally in the near afterglow of nanosecond pulsed discharges at atmospheric pressure [4, 8, 9]. It should be noted that nanosecond discharges, due to their significant overvoltage on the electrodes and short duration, may provide significant (hundreds of Td) electric fields, where the main part of discharge energy goes to excitation of electronic degrees of freedom (see, for example, analysis in [10]). Reduced electric fields, reported for surface nanosecond discharge, may be even higher and reach values up to kTd [4, 11].

It has been shown [4] that significant gas heating in surface nanosecond DBD in asymmetric plasma actuator geometry takes place approximately 1 μs after the nanosecond pulse is applied. From the velocity of shock wave propagation the authors obtained val-

ues for gas temperature of 70, 200, and 400 K in the plasma layer for 7, 12, and 50 ns pulse durations, respectively (voltage amplitudes ranged from 10–50 kV). The emerging shock wave together with the secondary vortex flows disturbed the main flow and caused flow rearrangement. Measurements of gas temperature using nitrogen emission gave values up to 400 K for pulse duration 25 ns at time $t = 1$ μs.

Paper [8] gives measurements of temperature dynamics under gas excitation by a pulsed discharge in atmospheric pressure air preheated to 1000 K and flowing at 0.5-2.6 m/s. The pulse duration was 30 ns, the pulse amplitude did not exceed $6 - 8.5$ kV, and the discharge was initiated in pin–to–pin geometry with the interelectrode space being equal to 5 mm with a frequency of 30 kHz. The gas temperature was determined using measured emission of $N_2(C^3\Pi_u, v' = 0) \rightarrow N_2(B^3\Pi_g, v'' = 0)$ transition. The authors report the gas temperature increase by several thousand Kelvin in the span of about 15-20 ns after the application of the high-voltage pulse. It should be noted that the highest temperature values obtained in the experiments [8] correspond to the near afterglow phase, when additional non–direct processes of $N_2(C^3\Pi_u, v' = 0)$ population may influence rotational distribution of the upper state, and, consequently, the obtained temperature value.

The gas density decrease in the near afterglow of a pulsed positive streamer in air in pin–to–plate geometry at 13 mm between the electrodes was studied in dry and humid air [9] by means of time–resolved shadography combined with optical emission. The authors demonstrated that the gas density decreases in two steps. The first, fast step, in the author's opinion, is connected with gas heating owing to electron impact onto molecules, and the second step is explained by vibrational-translational (VT) energy transfer.

A few mechanisms describing fast gas heating in nitrogen-oxygen mixtures have been recently suggested [12, 13]. Paper [12] gives detailed numerical analysis of the comparative roles of different processes for a field range of $50 - 400$ Td for gas pressure equal to 1 atm without comparison with experiments. Only paper [13] presents analysis of experiments [14], where shock wave propagation through air at $P \approx 20$ Torr preliminary excited by a volume nanosecond discharge has been studied, and results of experiments in a surface nanosecond dielectric barrier discharge (SDBD) in air at atmospheric pressure have been presented together with a computational model. To explain high values of temperature increase at a given energy input, the authors [13] suggest that at high electric fields and high pressures all the energy released in ion–molecular reactions and in ion–ion recombination is spent on gas heating and leads to significant temperature increase. The scale of fast gas heating in very high electric fields ($600 - 1000$ Td) is reported and demonstrates a good coincidence between the experiments and the model. Still, work [13] leaves a few questions connected with the complexity of experiments at high E/N; they are, for example, the accuracy of calculations of temperature and estimates of the electric field in single–shot shock tube experiments, and the accuracy of measurements of specific deposited energy for spatially non–uniform SDBD discharge.

Thus, the mechanism for fast gas heating at electric fields higher than 200 Td still remains a questionable issue and needs additional experimental and computational verification. The aim of our study is to develop an experimental approach to measuring key fast gas heating parameters and to verify a model proposed by [1] for the range of higher electric fields. To study the fast energy release in the afterglow of a pulsed discharge at high electric field, a high–voltage nanosecond discharge in the form of a fast ionization

wave (FIW) was used. The main reasons for using FIW are the spatial uniformity of the discharge, high values of reduced electric field during the discharge development, short duration of the discharge allowing separation of the discharge action and of the relaxation process; and the fact that FIW is well studied and characterized [15, 16]. The chapter reports electric current, specific energy input and reduced electric field measurements at a nanosecond time scale, combined with temperature measurements at the microsecond time scale in a spatially uniform configuration of a nanosecond discharge at moderate pressures. Analysis of main processes responsible for fast gas heating is given and the relative role of different processes is discussed.

2.2 Experimental setup

A discharge system has been developed that allows measurements of the current through the discharge setup, distribution of the potential along the discharge gap and emission from the discharge with nanosecond resolution, as well as measurements of the main active species responsible for kinetics in early afterglow.

The discharge is initiated in a quartz tube of 200 mm length with 9 mm inner diameter and 1 mm wall thickness. Semi–conical electrodes with 5 mm diameter axial openings are placed at the ends of the quartz tube. Traditionally, FIW experiments use flat [15, 16] or conical [17] electrodes to facilitate local electric field enhancement near the electrodes for discharge stabilization at low pressures. In this experiment, however, it is necessary for the electrodes to be hollow in order to allow optical probing along the longitudinal axis of the tube. For the sake of simplicity both the high and low voltage electrodes are identical in design. An Oriel deuterium lamp is used to stabilize the discharge initiation by focusing the light onto the high–voltage electrode with a UV lens. The discharge tube is surrounded by a grounded screen of 6 cm diameter. Two glass side tubes of 10 mm in diameter are connected to the electrodes (see figure 2.1) so that the total length of the system is equal to 78 cm. This is to create a laser cavity for cavity ring–down spectroscopy (CRDS) measurements of $N_2(A^3\Sigma_u^+)$ density in the FIW afterglow. Details of the laser system and preliminary results of CRDS measurements are described in [18].

The discharge tube was pumped with a XDS5 rotary pump; gas flow in a range of $10-30$ sccm was used so that the gas was recycled between subsequent high voltage pulses. Gas pressure was varied from 1 to 15 mbar in order to check the discharge propagation in this type of a FIW system and to compare the characteristics of the discharge for regimes corresponding to different reduced electric field (E/N) values. Synthetic air ($N_2:O_2 = 8:2$) or nitrogen with a purity of 99.999% were used for experiments.

Pulses with negative polarity, 22 kV amplitude on the high voltage electrode, 4 ns rise time, and 28 ns FWHM were applied at 2 Hz frequency from a FID FPG 10–1MKS20 pulse generator through a 25-m coaxial 50 ohm RG213 cable. The low voltage electrode was connected to a coaxial cable 100 or 200 m in length. Two coaxial calibrated current shunts were installed into a cable shield at a distances 12.5 m before and 12.5 m after the discharge tube. Each shunt was composed of 13 low–inductive resistors connected in parallel. A calibrated capacitive detector was installed into a slit of the screen of the discharge tube. Figure 2.2 represents a scheme of the experimental setup and typical signal from back current shunts.

In the present configuration of the experimental setup, three successive high–voltage
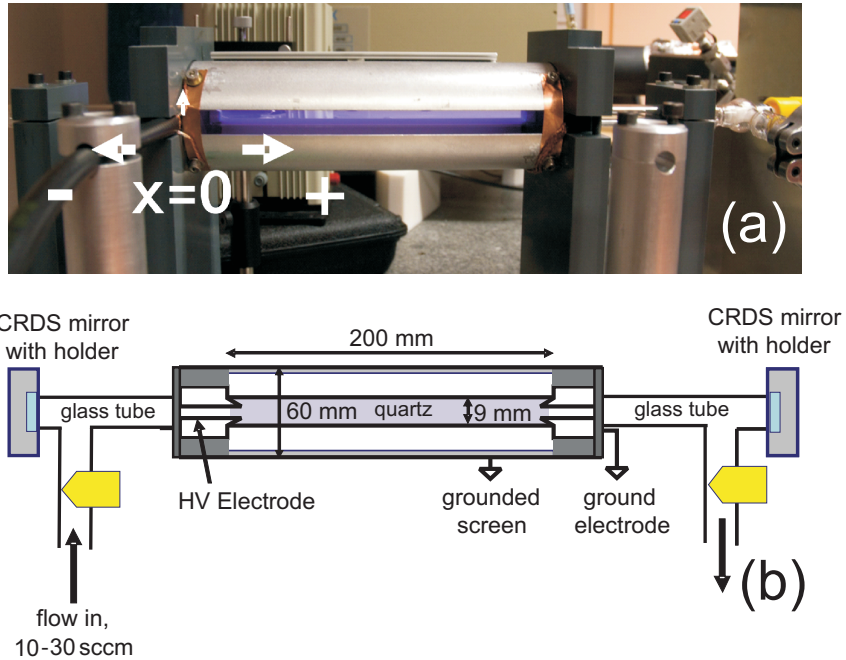
Figure 2.1: Photo (a) and scheme (b) of the discharge tube.

pulses were observed in the system due to reflections of the pulse from the discharge tube and then from the generator. These three pairs of pulses (incident–reflected from the discharge tube) and three correlated transmitted pulses are clearly seen in figure 2.2 in the time interval $0 - 0.7$ μs. The time between pulses is determined by a cable length between the current shunt and/or the high voltage generator/discharge tube.

The current and energy delivered to the discharge were deduced from analysis of the incident, reflected, and transmitted pulses recorded using the current shunts and a LeCroy WR44Xi Oscilloscope with 0.5 ns resolution.

The dynamics of the potential drop along the discharge tube starting from the cathode toward the anode over distance $L = 140$ mm was measured in 5 mm increment by a capacitive detector. Reduced electric field vs time was derived from these measurements for different positions along the discharge tube. Details of the measurement procedure can be found everywhere [19].

The present work is a first attempt to study parameters of a FIW in a system with hollow electrodes and side tubes. The amplitude of emission of the second positive system of molecular nitrogen ($N_2(C^3\Pi_u, v' = 0) \rightarrow N_2(B^3\Pi_g, v'' = 1)$, $\lambda =357.7$ nm) along the discharge tube and distribution of electric potential along the tube were measured in preliminary experiments. It was found that (i) neither emission, nor electric potential is observed in the side tube connected to low–voltage electrode; (ii) strong emission and some potential drop is observed between the high–voltage and low–voltage electrodes depending upon gas pressure; (iii) some emission is observed from the side tube close to the high–voltage electrode (region $x < 0$ in figure 2.1) while the electric potential in this part of the tube is always close to the potential of the high–voltage electrode. Statement (iii) was true whether a side tube without metal parts or a side tube with a CRDS mirror at floating potential were used.
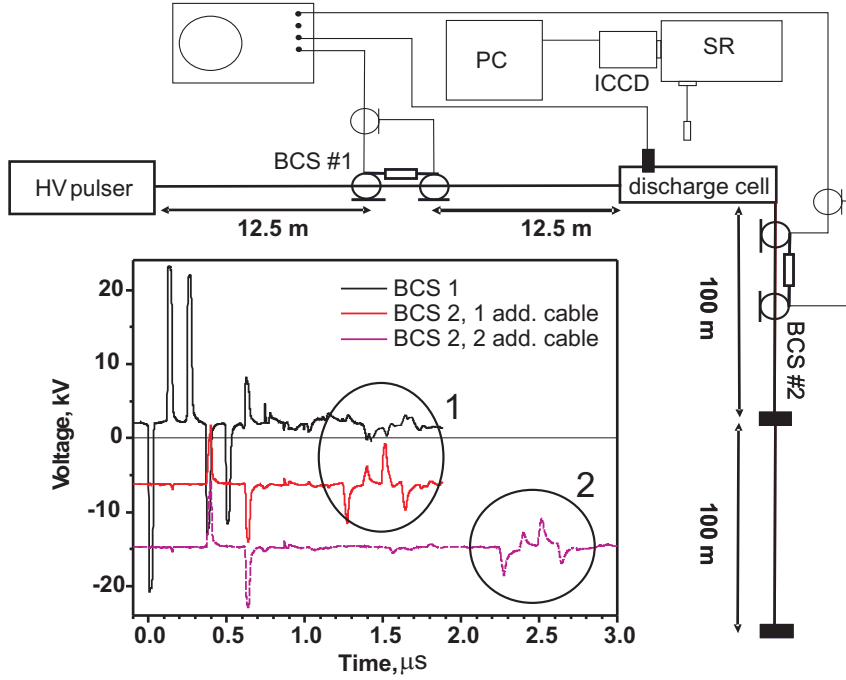
Figure 2.2: Scheme of the experimental setup and typical shape of signals from the back current shunts. Circles 1,2 designate additional reflections from the cable end used to excite $N_2(C^3\Pi_u)$ emission (see text for the detailed explanations).

Figure 2.3 presents the distribution of emission between the main discharge zone and side tube for the tube with a CRDS mirror. It is clearly seen that emission in the side tube is at least one order of magnitude less intense than in the interelectrode space. To check the energy losses, the discharge tube was disassembled and the deposited energy measured with and without a side tube adjacent to the high–voltage electrode. It was concluded that the difference in energy release in the gas for two used configurations does not exceed 10%. We therefore believe that the discharge develops primarily between the two metal electrodes and the energy release in the side tubes may be neglected for the purposes of this work.

It should be noted that the discharge cell used in the present work was characterized by a somewhat complicated discharge start. The main difference compared to a traditionally used geometry are the 5 mm openings in the electrodes and the two side tubes. Special experiments were therefore performed to check the discharge development.

It is known that for a typical voltage amplitude of 20 kV on the electrode in discharge tubes $2 - 5$ cm in diameter and $20 - 60$ cm in length, the nanosecond discharge starts with high stability for repetitive frequencies starting from a few Hz with flat or conical high–voltage electrodes [16, 20, 19]. The discharge develops uniformly in space within a pressure range of $1 - 15$ mbar, with a maximum energy input at about $4 - 6$ mbar.

By contrast, in our case the discharge was not stable even with UV–preionization. In a special set of experiments to analyze the discharge stability, 100 successive oscillograms from the current shunts were taken for each regime and deposited energy was calculated. The results of statistical analysis for a pressure 9 mbar are given by figure 2.4. It is clearly

9
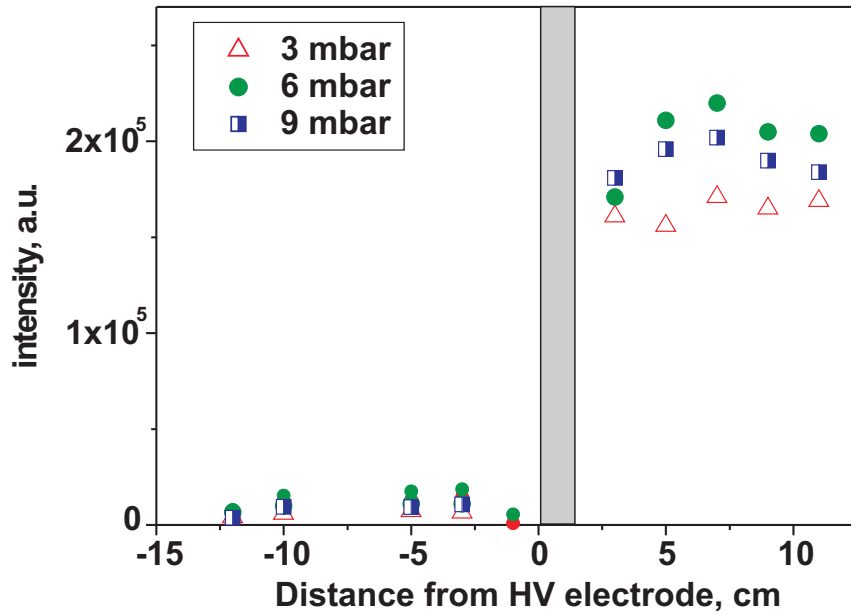
Figure 2.3: Analysis of discharge development. Peak emission intensity (λ =357.7 nm) between the electrodes ($x > 0$) and in the side tube ($x < 0$).

seen that about 70 % of shots give repetitive data. Therefore for all the experiments we first made a statistical analysis, and then only the data from quasi–stationary part (events $1-70$ in the figure 2.4) were taken to provide for stability of all the parameters analyzed.

Emission spectra were measured with a UV fiber optic–fed Andor SR–303i spectrometer (grating with 2400 l/mm, operating range $190-700$ nm, reverse linear dispersion 2.6 nm/mm) and Andor iStar DH734-18U-03 ICCD camera (spectral range $115-900$ nm). The spectrograph was calibrated using an Ocean Optics Hg–Ar lamp. In order to capture the entirety of the emission, a 100 ns gate was used. The ICCD camera gate monitor and voltage pulse waveforms were measured simultaneously with the oscilloscope in order to ensure timing accuracy. Emission measurements were taken in a few time instants, so that the camera gate was synchronized either with pulses from the generator or with pulses reflected from a 100 or 200 m cable used as a delay line. These reflections are marked with circles 1 and 2 in figure 2.2, respectively. They provide the delay of emission measurements relative to the discharge within a range $1-2$ μs.

To derive a gas temperature, the rotational spectra of the emission of the $0-1$ transition of the second positive system of N_2 (λ =357.7 nm) were measured. Specair code [21] was used to simulate spectra with the slit function determined experimentally on the basis of the Hg line.

In the case when rotational relaxation of the electronically excited state is slow comparing to the life time, it is important that the population takes place due to direct electron impact. Under this condition, the rotational distribution of the upper electronic state reproduces the rotational distribution of the ground state. The life time

10
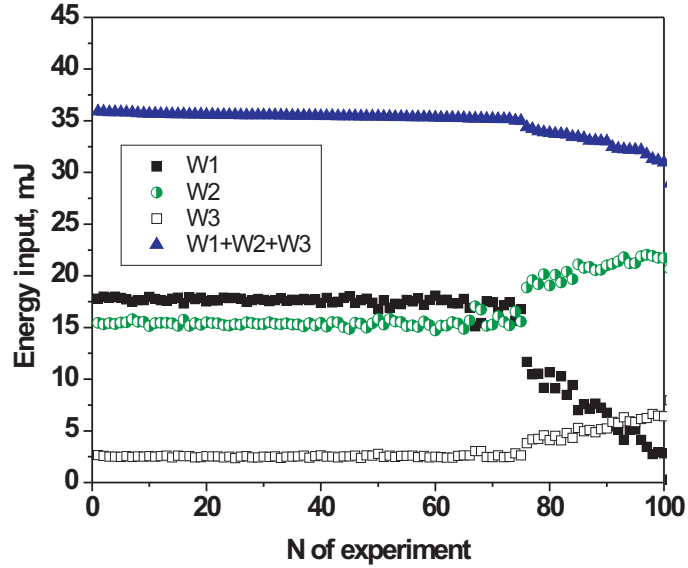
Figure 2.4: Statistical analysis of stability of a FIW start. Typical data obtained for N_2:O_2=80:20 mixture, pressure 9 mbar.

of $N_2(C^3\Pi_u)$state is about 40 ns [22], which is smaller than a typical time of rotational relaxation, so special experimental efforts were taken to ensure that it is possible to neglect additional stray emission caused by pooling processes ($N_2(A^3\Sigma_u^+)$ + $N_2(A^3\Sigma_u^+)$ $\rightarrow$ $N_2(C^3\Pi_u)$+ N_2, $N_2(C^3\Pi_u)\rightarrow N_2(B^3\Pi_g)$ + $h\nu$).

Figure 2.5 gives an example of nitrogen emission at λ =357.7 nm for two test cases. The solid line represents the emission in the additional pulse when the additional discharge is initiated 1.5 μs after the first high–voltage pulse (100 m cable is connected to the low–voltage electrode). The dashed line represents the emission in the same time instant when the additional pulse is absent (the 200 m cable is connected to the low–voltage electrode). It is clearly seen that the background emission of the second positive system of N_2 is still observed but the amplitude of the emission is orders of magnitude lower. If the temperature were determined on the basis of the background emission caused by pooling processes, it would be roughly 700 K. Temperature, determined from the emission excited by the additional pulse, gives values about 400 K. Thus, every time the measurements were performed in the afterglow, we checked that the background emission is significantly lower in amplitude than the emission caused by an additional high–voltage pulse.

2.3   Experimental results

Preliminary experiments show that under given experimental conditions the optimal pressure range for the development of a nanosecond discharge is $1-15$ mbar. For the analysis of fast gas heating, a set of experiments at 3, 6 and 9 mbar has been performed. For each pressure, electric current, deposited energy, and electric field versus time have been measured at a nanosecond time scale. Temperature was measured in 5 time instants within

the time interval of 30 ns–3 μs.
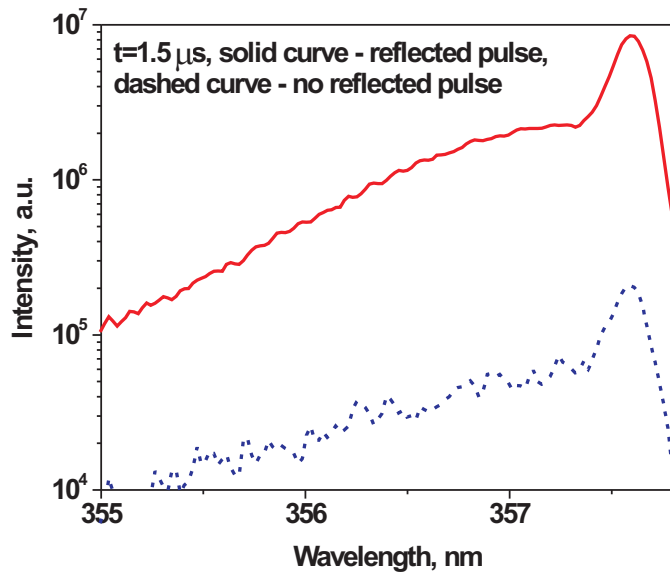
Figure 2.5: N_2:O_2=80:20, $P = 6$ mbar. An example of emission initiated by an additional pulse (solid curve) and emission present in the afterglow at time instant 1.5 μs due to pooling processes.

The distribution of deposited energy between different pulses is given by figure 2.6. It is clearly seen that the energy input in the third pair of pulses is less than 10% of the energy of the incident pulse. For 3 mbar, the bulk of the energy is deposited in the second pair of pulses. For 6 and 9 mbar, roughly equal energy input is observed for the first and second pair of pulses.

This observed dependence is explained by the character of the breakdown and illustrated by the behavior of the reduced electric field, E/N (see figure 2.7).

For 3 mbar, we observe essentially zero energy input in the first pair of pulses (at $t = 0$). A sharp and short peak of the electric field (a few kTd during a few nanoseconds) is responsible for some initial ionization. The breakdown develops in the second pair of pulses, at $t \approx 245$ ns, as it is illustrated by figure 2.7 a.

At 6 and 9 mbar, the peak of high electric field is followed by a pulse of a few tens of nanoseconds where the field value does not exceed $400 - 500$ Td and then, 245 ns later, by a second pulse with an amplitude of $200 - 300$ Td. The first sharp peak corresponds to a fast ionization wave, which crosses the discharge gap between the electrodes, and the pulses with duration of $20 - 30$ ns correspond to a stage when the discharge gap is closed to the low voltage electrode. It is during this stage when the electric current reaches its maximum value. The second pulse of the electric field, 245 ns later, does not contain a high peak of the electric field because the ionization is still enough for the fast ionization wave to start.

The electric current behaves in a similar way. Figure 2.8 represents current measured by the first current shunt installed in a cable 12.5 m before the tube as a difference between

12
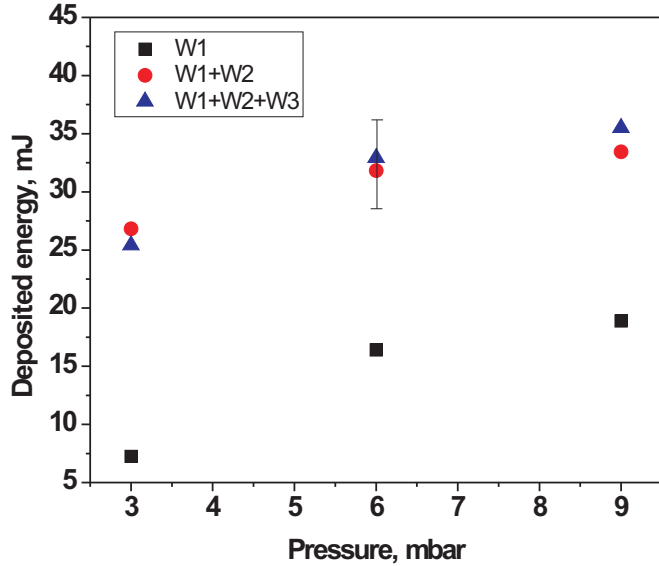
Figure 2.6: Deposited energy vs pressure. W1, first pair of pulses; W1+W2, first and second pairs of pulses; W1+W2+W3, total deposited energy. Total energy stored in the incident pulse from the generator is 55 mJ.

the incident and the reflected pulses. It should be noted that this coincides with the transmitted current measured by a current shunt 12.5 m after the discharge tube with the exception of the very first step on the current pulse (first 10 ns, see figures 2.8 b, c), which corresponds to charging the quartz tube in the process of the FIW development. Data for electric current, given by the figure 2.8, was taken as initial data for the calculations of kinetics in the discharge and gas heat release.

When calculating specific deposited energy from the signals of the current shunts (for details see the section 2.4), we assumed that the discharge was uniform between the electrodes and that no energy was deposited into the side tubes.

The results of calculations were compared to results of temperature measurements using the emission of the second positive system of molecular nitrogen.

2.4   Numerical modeling and discussion

The calculations are based on the experimentally obtained dependence of current versus time. It is assumed that the discharge gap closes fast in comparison to the total duration of the current pulse. Then, in assumption of the uniformity of the discharge parameters over the cross-section of the tube [16, 23], the electric field is calculated as

$$E = \frac{I}{e\mu_e N_e S},$$
(2.1)

where I is the discharge current value for a given time moment, μ_e is the electron mobility (it is a function of reduced electric field E/N, N is a gas density), N_e is the electron density,

13
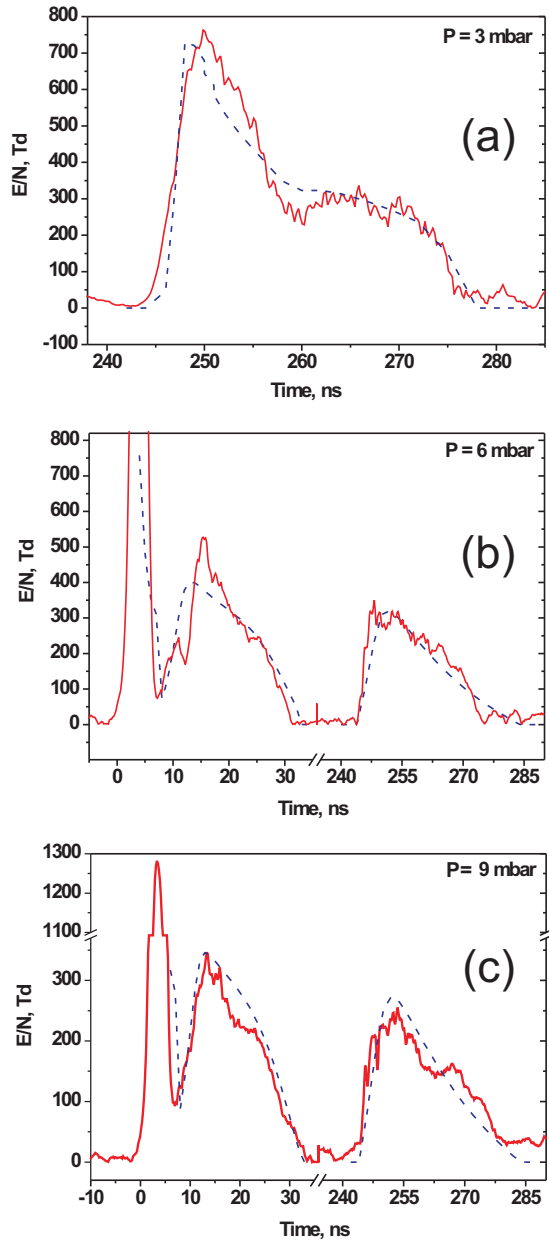
Figure 2.7: Reduced electric field *vs* time. (a) $P = 3$ mbar, (b) $P = 6$ mbar and (c) $P = 9$ mbar, the data are taken 7 cm apart from the high–voltage electrode. Solid curves are the experimental data, dashed curves are the results of calculations.

and S is the cross–section of the discharge tube.

The following equation is solved for the electron density:

$$\frac{dN_e}{dt} = N_e(\nu_{ion} - \nu_{att}) + Q_{ass} - Q_{rec} + Q_{det}. \tag{2.2}$$

Here ν_{ion} and ν_{att} are frequencies of ionization by electron impact and electron attachment respectively (both are functions of E/N), Q_{rec} is the rate of electron–ion recombi-

14
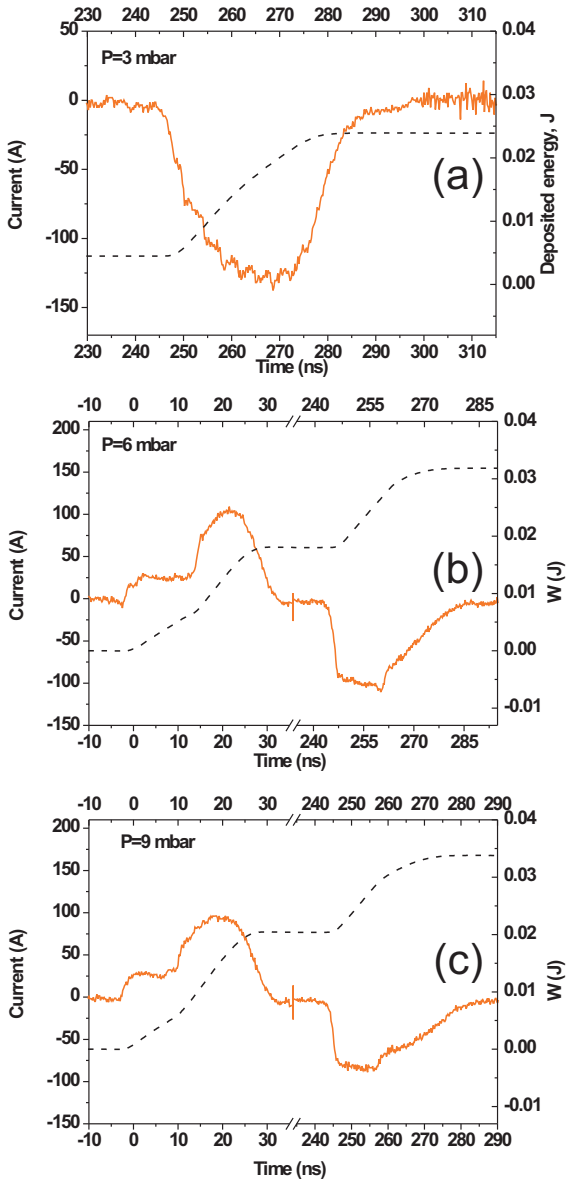
Figure 2.8: Current (solid curves) and deposited energy (dashed curves) *vs* time, experiments. (a) $P = 3$ mbar, (b) $P = 6$ mbar and (c) $P = 9$ mbar.

nation, Q_{det} is the electron detachment rate which includes all the processes of electron detachment from the negative ions, namely the processes with participation of atoms $O(^3P)$, molecules $O_2(a^1\Delta_g)$ etc. [24]; and Q_{ass} takes into account additional production of charged species due to associative ionization.

Similar balance equations have been written for all charged species; ten positive and negative ions have been taken into account: O_2^+, O_4^+, $O_2^+ \cdot N_2$, N_2^+, N_4^+, NO^+, O^-, O_2^-, O_3^-, O_4^-. The system of ion–molecular reactions suggested in [24, 25] has been taken as a basis for calculations of the kinetics of the charged species. Ionization, dissociation and excitation rates were calculated for each time instant as a function of reduced electric field

15

on the basis of the solution of the Boltzmann equation in a two-term approximation using BOLSIG+ code [26]. For the considered experimental conditions, the reduced electric fields in the region of significant energy input satisfies the condition $E/N \leq 1000$ Td, which is why it is possible to use two–term approximation of the Boltzmann equation to determine the electron energy distribution function (EEDF) [27, 28]. It was assumed that for given conditions the electronic excitation of species takes place by a direct electron impact from the ground state of molecules. The change of rates of the reactions with vibrational excitations of molecules was taken into account similar to [29]. The following neutral species were considered by the model: $N_2(X^1\Sigma_g^+)$, $N_2(A^3\Sigma_u^+)$, $N_2(B^3\Pi_g)$, $N_2(C^3\Pi_u)$, $N_2(a'^1\Sigma_u^-)$, $N(^4S)$, $N(^2D)$, $N(^2P)$, $O_2(X^3\Sigma_g^-)$, $O_2(a^1\Delta_g)$, $O(^3P)$, $O(^1D)$, $O(^1S)$. The reactions and rate constants used are given in [1, 24, 30]. To describe the gas heating in the discharge, the following processes responsible for temperature increase have been taken into account:

2.4.1 Electron recombination with molecular ions

Energy deposited in reactions of dissociative electron-ion recombination is distributed between electronic and vibrational states of particles. At the relatively low pressures of the present experiments ($P = 3 - 9$ mbar), the main positive ions are O_2^+, N_2^+, N_4^+.

The ratio of the channels of electron-ion recombination of O_2^+ and N_2^+:

$$e + O_2^+ \rightarrow Prod, \qquad k = 1.95 \cdot 10^{-7} \cdot (300/T_e)^{0.7} \text{ cm}^3/\text{s} \qquad (2.3)$$

$$e + N_2^+ \rightarrow Prod, \qquad k = 1.8 \cdot 10^{-7} \cdot (300/T_e)^{0.39} \text{ cm}^3/\text{s} \qquad (2.4)$$

is the following [31]:

$$
\begin{aligned}
e + O_2^+ \quad &\rightarrow \quad O(^3P) + O(^3P) + 6.95 \text{ eV} \quad & 32 \ \% \\
&\rightarrow \quad O(^1D) + O(^3P) + 4.99 \text{ eV} \quad & 43 \ \% \\
&\rightarrow \quad O(^1D) + O(^1D) + 3.02 \text{ eV} \quad & 20 \ \% \\
&\rightarrow \quad O(^1D) + O(^1S) + 0.80 \text{ eV} \quad & 5 \ \%
\end{aligned} \qquad (2.5)
$$

$$
\begin{aligned}
e + N_2^+ \quad &\rightarrow \quad N(^4S) + N(^4S) + 5.82 \text{ eV} \quad & 0 \ \% \\
&\rightarrow \quad N(^4S) + N(^2D) + 3.44 \text{ eV} \quad & 46 \ \% \\
&\rightarrow \quad N(^2D) + N(^2D) + 1.06 \text{ eV} \quad & 46 \ \% \\
&\rightarrow \quad N(^4S) + N(^2P) + 2.25 \text{ eV} \quad & 8 \ \%
\end{aligned} \qquad (2.6)
$$
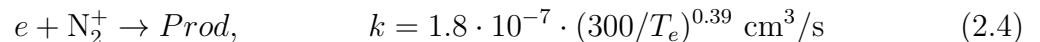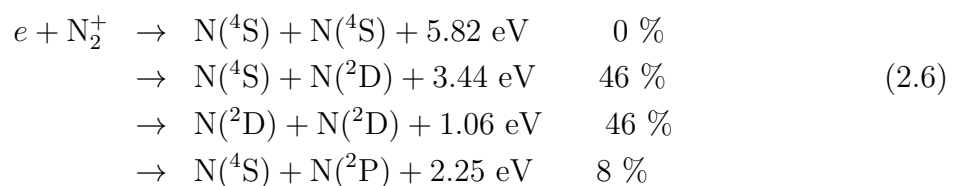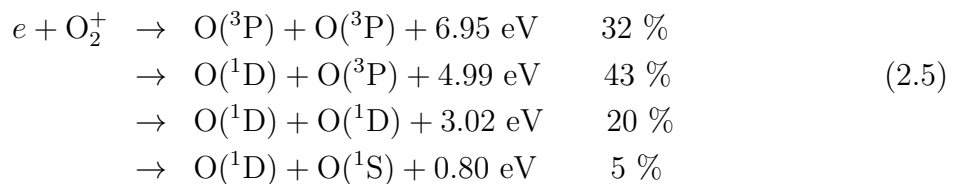
Thus, the energy which goes to gas heating due to reactions (2.2) and (2.3) comprises 5.0 eV and 2.25 eV, respectively.

It was assumed that the recombination of N_4^+ ion leads to production of excited $N_2(C^3\Pi_u)$ molecules [32], and the rest of energy goes to vibrational excitation of molecular nitrogen $N_2(X^1\Sigma_g^+, v')$:

$$N_4^+ + e \rightarrow N_2(C^3\Pi_u, v) + N_2(v').$$

In the N_2:O_2 mixture used in experiments, the density of H_2O molecules did not exceed 3 ppm. It was therefore assumed that the influence of H_2O molecules on ion composition and gas heating is negligible.

2.4.2 Oxygen and nitrogen dissociation by electron impact

$$e + N_2 \rightarrow e + N_2^*, \qquad N_2^* \rightarrow N(^4S) + N(^2D) + \varepsilon_R,$$
$$e + O_2 \rightarrow e + O_2(B^3\Sigma_u^-, v), \qquad O_2(B^3\Sigma_u^-, v) \rightarrow O(^3P) + O(^1D) + \varepsilon_R,$$
$$e + O_2 \rightarrow e + O_2(A, v), \qquad O_2(A, v) \rightarrow O(^3P) + O(^3P) + \varepsilon_R,$$

$$O_2(A) = O_2(A^3\Sigma_u^+, C^3\Delta_u, c^1\Sigma_u^-).$$
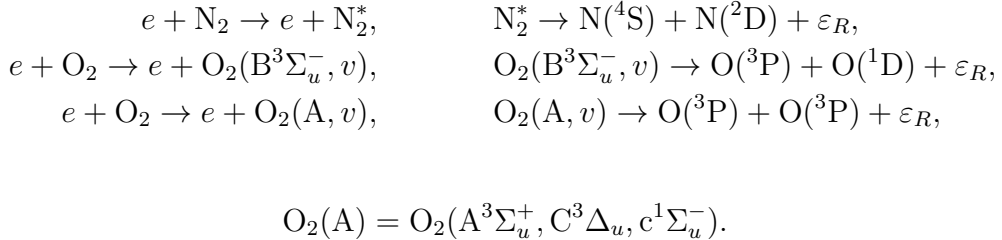
The dissociation of N_2 and O_2 molecules goes through excitation of these molecules by an electron impact and following predissociation from via electronically excited states [33, 34]. The products of predissociation can have significant kinetic energy. This energy was calculated in the following way:

$$\varepsilon_R = \varepsilon_{th} - \varepsilon_{diss}, \tag{2.7}$$

where ε_{th} is the threshold energy for excitation of a predissociated state by an electron impact, and ε_{diss} is the dissociative limit. For $O_2(A^3\Sigma_u^+, C^3\Delta_u, c^1\Sigma_u^-)$ states it was taken that $\varepsilon_R = 0.8$ eV, and for $O_2(B^3\Sigma_u^-, v)$ it was taken that $\varepsilon_R = 1.26$ eV [28].

2.4.3 Quenching of electronically excited species of nitrogen by oxygen.

Excited electronic states of molecular oxygen, such as $O_2(B^3\Sigma_u^-, v)$, $O_2(A^3\Sigma_u^+, v)$, $O_2(c^1\Sigma_u^-, v)$, can be populated due to quenching of molecular nitrogen by O_2 molecules. Predissociation of these levels leads to O_2 dissociation and energy release to kinetic energy of created oxygen atoms. Thermalization of "hot" atoms takes place during a few collisions, and the rest of energy goes to rotational excitation of molecules and directly to gas heating. In turn, rotational-translational relaxation takes place for a few tens of collisions [33, 34] and so, kinetic energy of oxygen atoms transforms to gas heating.

Table 2.1: Quenching of electronically excited nitrogen molecules in N_2:O_2 mixtures. Main reactions.

N	Reaction	k, cm^3/s	Reference
R1.	$N_2(A^3\Sigma_u^+) + O_2 \rightarrow N_2(v) + 2 \cdot O(^3P) + \varepsilon_1$	$1.7 \cdot 10^{-12}$	[1, 30]
R2.	$N_2(A^3\Sigma_u^+) + O_2 \rightarrow N_2(v) + O_2(b^1\Sigma_g^+)$	$7.5 \cdot 10^{-13}$	[1, 30]
R3.	$N_2(A^3\Sigma_u^+) + N_2(A^3\Sigma_u^+) \rightarrow N_2(v) + N_2(B^3\Pi_g)$	$7.7 \cdot 10^{-11}$	[1, 30]
R4.	$N_2(A^3\Sigma_u^+) + N_2(A^3\Sigma_u^+) \rightarrow N_2(v) + N_2(C^3\Pi_u)$	$1.6 \cdot 10^{-10}$	[1, 30]
R5.	$N_2(A^3\Sigma_u^+) + O(^3P) \rightarrow N_2(v) + O(^1S)$	$3.0 \cdot 10^{-11}$	[1, 30]
R6.	$N_2(B^3\Pi_g) + O_2 \rightarrow N_2(v) + 2 \cdot O(^3P) + \varepsilon_6$	$3.0 \cdot 10^{-10}$	[1, 24]
R7.	$N_2(B^3\Pi_g, v = 0) + N_2 \rightarrow N_2(A^3\Sigma_u^+, v) + N_2(v)$	$2.0 \cdot 10^{-13}$	[1, 24]

Table 2.1: Quenching of electronically excited nitrogen molecules in $N_2:O_2$ mixtures. Main reactions.

N	Reaction	k, cm^3/s	Reference
R8.	$N_2(a'^1\Sigma_u^-) + O_2 \rightarrow N_2(v) + O(^3P) + O(^1D) + \varepsilon_8$	$2.8 \cdot 10^{-11}$	[1, 36]
R9.	$N_2(a'^1\Sigma_u^-) + N_2 \rightarrow N_2(B^3\Pi_g) + N_2(v)$	$2.0 \cdot 10^{-13}$	[1, 36]
R10.	$N_2(C^3\Pi_u) + O_2 \rightarrow N_2(v) + 2 \cdot O + \varepsilon_{10}$	$2.5 \cdot 10^{-10}$	[22]
R11.	$N_2(C^3\Pi_u) + N_2 \rightarrow N_2(v) + N_2(B^3\Pi_g, v)$	$1.0 \cdot 10^{-11}$	[22]
R12.	$N_2(C^3\Pi_u) \rightarrow N_2(B^3\Pi_g) + h\nu$	$2.7 \cdot 10^{10}$ s^{-1}	[22]

The main reactions of quenching of electronically excited levels of molecular nitrogen are given in Table 2.1. It should be noted that the ratio of channels of dissociation and excitation of products has been investigated for the $N_2(A^3\Sigma_u^+)$ state (reactions R1-R2) only [30]. It is known that with an increase in the number of vibrational level of $N_2(A^3\Sigma_u^+, v=0)$ both reaction rate [30] and ratio of channels [35] can be changed, namely the role of O_2 dissociation increases. More than that, the energy release to gas heating in the reaction R1 depends upon the number of the vibrational level.

Reactions where energy release was taken into account, are accompanied by ε_R in the right side of the equations in the table ??. To calculate the energy release to translational degrees of freedom, ε_R, in the reactions R1, R6, R8, and R10 the model developed in [1, 28] was used. Namely, it was assumed that the probability of population of a vibrational level v of a ground state of nitrogen in the reaction

$$N_2^* + O_2 \rightarrow N_2(X^1\Sigma_g^+, v) + O(^3P) + O(^3P,^1D),$$

$$N_2^* = N_2(A^3\Sigma_u^+, v'), \ N_2(B^3\Pi_g), \ N_2(a'^1\Sigma_u^-), N_2(C^3\Pi_u)$$
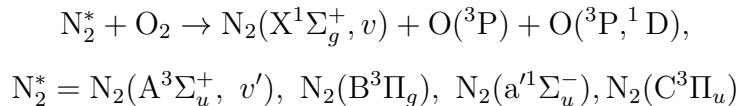
is proportional to a Frank–Condon factor q_v of a transition between initial and final state of a nitrogen molecule: $N_2^* \rightarrow N_2(X^1\Sigma_g^+, v)$. The energy release ε_R was calculated as [1, 28]

$$\varepsilon_R = \varepsilon^* - \varepsilon_{diss} - \sum_v q_v \varepsilon_v, \tag{2.8}$$

where ε^* is the energy of excited state of molecular nitrogen N_2^*, ε_{diss} is the dissociative limit of created electronic state of molecular oxygen, and ε_v is the energy of the vibrational excitation of the $N_2(X^1\Sigma_g^+, v)$ molecules. A summation is made only for the vibrational levels for which the following property holds: $\sum q_v \varepsilon_v \leq \varepsilon^* - \varepsilon_{diss}$.

It should be noted that there is a significant uncertainty in energy release to gas heating, ε_R, in the process of $N_2(C^3\Pi_u)$ quenching (reaction R10). The products of this reaction, in particular the electronic states of produced oxygen atoms, are not known [13, 28]. At the same time excitation of this electronic state is very efficient at high electric fields and its quenching must be important for mechanism of fast gas heating [13, 28]. At our experimental conditions of relatively low gas pressure, the main channel of $N_2(C^3\Pi_u)$ desactivation is radiative quenching (R12) rather than quenching by oxygen (R10), so it is possible to avoid the mentioned uncertainty.

2.4.4 Quenching of $O(^1D)$ atoms

Reactions of dissociation of molecular oxygen often lead to production of excited $O(^1D)$ atoms. In nitrogen-oxygen mixtures these atoms can be quenched in the following reac-

tions [24]:

$$
\begin{aligned}
\mathrm{O}(^1\mathrm{D}) + \mathrm{N}_2 \;&\rightarrow\; \mathrm{O}(^3\mathrm{P}) + \mathrm{N}_2(v) + \varepsilon_R, \; k = 1.8 \cdot 10^{-11} \cdot \exp(107/T) \; \mathrm{cm}^3/\mathrm{s} \qquad (2.9) \\
\mathrm{O}(^1\mathrm{D}) + \mathrm{O}_2 \;&\rightarrow\; \mathrm{O}(^3\mathrm{P}) + \mathrm{O}_2(b^1\Sigma_g^+, \; v), \; k = 2.56 \cdot 10^{-11} \cdot \exp(67/T) \; \mathrm{cm}^3/\mathrm{s} \\
\mathrm{O}(^1\mathrm{D}) + \mathrm{O}_2 \;&\rightarrow\; \mathrm{O}(^3\mathrm{P}) + \mathrm{O}_2(X^3\Sigma_g^-, \; v), \;\; k = 0.64 \cdot 10^{-11} \cdot \exp(67/T) \; \mathrm{cm}^3/\mathrm{s}
\end{aligned}
$$
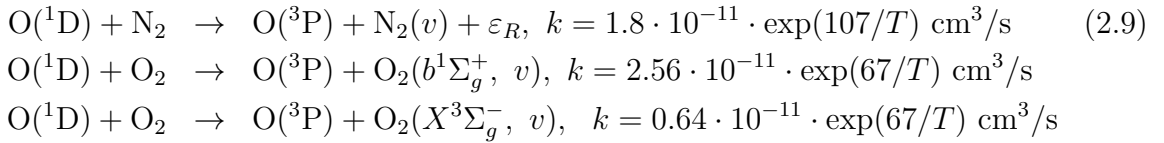
Quenching of $\mathrm{O}(^1\mathrm{D})$ by molecular nitrogen has been studied in a number of papers. It was demonstrated that this reaction goes through the intermediate complex, at this $30 \pm 10\ \%$ of energy goes to vibrational excitation of N_2 [1]. Based on this, it was assumed that $\cong 70\ \%$ of $\mathrm{O}(^1\mathrm{D})$ excitation energy is spent for gas heating, that is that for the reaction (9) $\varepsilon_R \cong 1.38$ eV.

2.4.5 Reactions of VT-relaxation of vibrationally excited $\mathrm{N}_2(v)$ molecules

An important processes of vibrational desactivation of $\mathrm{N}_2(v)$ molecules in $\mathrm{N}_2{:}\mathrm{O}_2$ mixtures is vibrational–translational (VT) relaxation on $\mathrm{O}(^3\mathrm{P})$ atoms:

$$
\mathrm{N}_2(v) + \mathrm{O}(^3\mathrm{P}) \rightarrow \mathrm{N}_2(v-1) + \mathrm{O}(^3\mathrm{P}) + \varepsilon_R.
$$
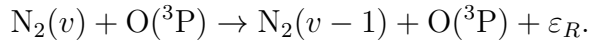
These reactions at the conditions of a relatively high dissociation degree of O_2 are significant for gas heating. To describe VT - relaxation of $\mathrm{N}_2(v)$ on $\mathrm{O}(^3\mathrm{P})$ atoms, the reaction rate constant from [37] was taken:

$$
\mathrm{N}_2(v=1) + \mathrm{O}(^3\mathrm{P}) \rightarrow \mathrm{N}_2(v=0) + \mathrm{O}(^3\mathrm{P}), \qquad k_{VT} = 4.5 \cdot 10^{-15} \cdot \left(\frac{T}{300}\right)^{2.1} \; \mathrm{cm}^3/\mathrm{s}.
$$
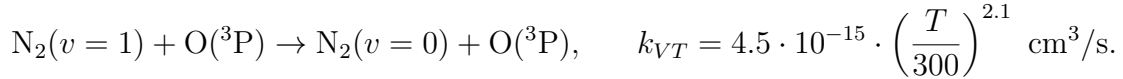
As far as for the given conditions VT - relaxation of O_2 and NO molecules is fast, vibrational temperatures of these molecules were considered to be equal to translational temperature of the gas.

Evolution of a gas temperature was described by the following equation:

$$
C_v N \cdot \frac{dT}{dt} = \frac{\varepsilon - \varepsilon_v(T)}{\tau_{VT}} + W_R, \qquad (2.10)
$$

where C_v is the specific heat capacity at constant volume, N is the gas density, ε_v is the average vibrational energy per N_2 molecule, τ_{VT} is the characteristic time of VT relaxation of $\mathrm{N}_2(v)$, and W_R is the rate of gas heating in chemical reactions.

Equation (2.10) describes gas heating in an isochore assumption, which is true for the condition of given experiments. Indeed, typical times for gas-dynamic processes are equal to $\tau_g \cong 300\ \mu$s at a tube length of $L = 20$ cm. As far as the process of fast gas heating is considered within a time scale of $t < 50 \mu s << \tau_g$, the isochore assumption is valid for the central part of the discharge tube.

Gas cooling due to the thermal conductivity is not considered by equation (2.10). It follows from estimates that at $P \geq 3$ mbar, $T \leq 450$ K and discharge tube radius $R = 0.45$ cm it is possible to disregard this process for times less than 50 μs.

Figure 2.9: Factor Θ, describing a number of inelastic collisions (solid curve), and specific deposited energy (dashed curve) *vs* time. $P = 3$ mbar.

2.5 Temperature measurements and results of numerical calculations

Temporal behavior of the discharge current was taken from experiments (see figure 2.8). All three successive pulses discussed in the section 2.3 were taken into account. The reduced electric field E/N was calculated as described in the section 2.4. Figure 2.7 represents calculated reduced electric fields (dashed curves) together with results of measurements (solid curves). It is clearly seen that for all pressures under consideration (3, 6 and 9 mbar) the coincidence between calculations and measurements is good, which provides an adequate description of ionization, dissociation and excitation by electron impact during the discharge phase. At relatively low gas pressures and fast change of E/N it is important to estimate if stationary solution of the Boltzmann equation is applicable for EEDF calculations. The Θ factor, describing a number of non–elastic collisions of electrons during a typical time of E/N change, has been calculated:

$$\Theta = \nu_u \cdot \left(\frac{1}{E} \cdot \left| \frac{dE}{dt} \right| \right)^{-1}, \tag{2.11}$$

here ν_u is the effective frequency of relaxation of energy of electrons [38]. Factor Θ versus time for our experimental conditions at $P = 3$ mbar is given by figure 2.9. It is evident that $\Theta >> 1$ for the region of a main energy input. Similar results were obtained for 6 and 9 mbar. Therefore the EEDF relaxation in the region of thresholds of non-elastic processes takes place and the use of a stationary solution of the Boltzmann equation is possible.

To summarize the energy input, table 2.2 gives a comparison of experimentally measured and calculated values for all three pulses. For present experimental conditions, the

main energy input takes place at $E/N = 200 - 400$ Td, providing efficient electronic excitation and dissociation of molecules, with the following increase of gas temperature.

Calculated kinetic curves for charged species are presented in figure 2.10. The main positive ions at our experimental conditions are N_2^+ and O_2^+. The density of N_4^+ complex ions is low because of a low overall gas density, and so it does not change the efficient coefficient of electron–ion recombination. The density of negative ions is not higher than the N_4^+ density and thus is not given in the figure. For N_2^+ ions, other important processes of recombination are charge exchange on molecular oxygen $N_2^+ + O_2 \rightarrow O_2^+ + N_2$ and conversion to $N_4^+ : N_2^+ + N_2 + M \rightarrow N_4^+ + M$.

Table 2.2: Specific deposited energy (10^{-3} eV/mol) for three pulses w_1, w_2 and w_3 for gas pressures 3, 6 and 9 mbar.

	w_1 (exp/calc)	$w_1 + w_2$ (exp/calc)	$w_1 + w_2 + w_3$ (exp/calc)
3 mbar	3.0/3.5	120.4/121.0	129.6/129.0
6 mbar	53.0/53.6	102.8/103.0	107.0/107.0
9 mbar	40.7/40.7	72.0/72.4	76.5/76.6

The results of calculations of $O(^3P)$, $N_2(A^3\Sigma_u^+)$, $N_2(B^3\Pi_g)$, and $N_2(C^3\Pi_u)$ densities at $P = 6$ mbar are shown in figure 2.11. The same figure gives (indicated with points) results of $[N_2(A^3\Sigma_u^+), \ v = 0)]$ measurements in arbitrary units. A high degree of dissociation of molecular oxygen by the discharge ($[O(^3P)]/[O_2] \approx 10$ %) should be noted.

For a pressure range of our experiments, the typical times of the discharge processes responsible for fast gas heating in the discharge afterglow are the following: quenching of the $N_2(B^3\Pi_g)$ state of nitrogen by molecular oxygen (reaction R6) takes approximately 100 ns, electron-ion recombination of N_2^+ and O_2^+ ions takes hundreds of nanoseconds, and quenching of the metastable $N_2(A^3\Sigma_u^+)$ level (reaction R1) needs tens of microseconds. Thus, at time equal to approximately 50 μs the fast energy release stops. Further increase of gas temperature can be connected with the recombination of atomic oxygen and VT–relaxation of $N_2(v)$ molecules. Under the considered conditions, these processes take place with typical times of more than tens of milliseconds, and were not considered.

Figure 2.12 presents experimental data and results of calculations of temperature increase in the discharge and near afterglow. For all three pressures, the agreement is rather good. It follows from the calculations that a significant fraction of the energy goes into gas heating at a sub–microsecond time scale immediately after each discharge pulse. As already mentioned, this is connected with quenching of excited nitrogen by molecular oxygen and quenching of excited $O(^1D)$ atoms on N_2 molecules. It should be noted that with electric field, further change of the mechanisms of fast gas heating can be observed. It was suggested in [13] that all the energy released in reactions of ion-ion recombination, is spent on gas heating and leads to significant temperature increase. In particular, reactions

$$N_2^+ + N_2 + M \rightarrow N_4^+ + M, \tag{2.12}$$

$$N_4^+ + O_2 \rightarrow O_2^+ + N_2 + N_2, \tag{2.13}$$

$$N_2^+ + O_2 \rightarrow O_2^+ + N_2, \tag{2.14}$$
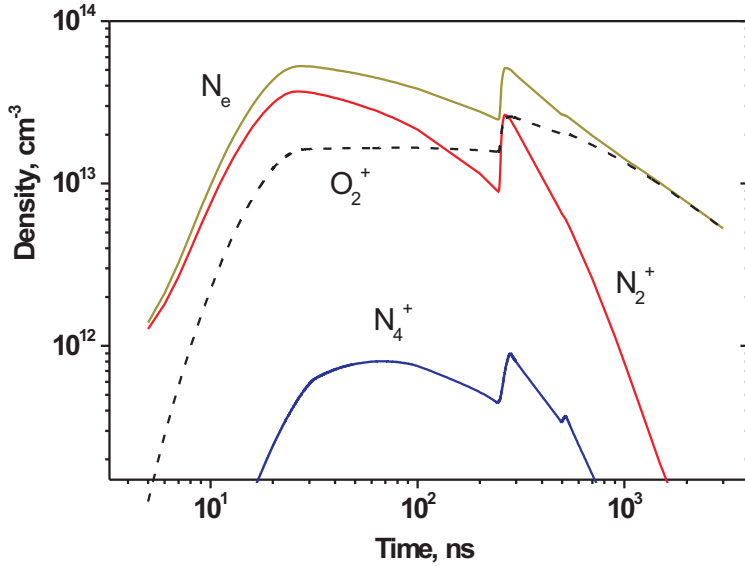
Figure 2.10: Kinetic curves for main charged species at gas pressure $P = 6$ mbar.

give 1.1 eV, 2 eV and 3.1 eV, respectively. Our experimental conditions do not allow check of the validity of the given assumption: the additional gas heating due to these processes does not exceed $2 - 3$ K because of relatively low energy release to ionization at $E/N = 200 - 400$ Td and negligible role of complex ions at $3 - 9$ mbar [28]. To affirm or refute the suggestion of [13], the pulsed discharge should be organized uniformly in space, at high pressures, with extremely high electric fields $E/N > 600 - 800$ Td in the region of main energy release, and with specific deposited energy on the level of 0.1 eV/molecule or higher. Such a discharge system is a challenge for kinetic study.

It is seen from figure 2.12 a–b that at $P = 6$ and 9 mbar at time $t = 240$ ns the gas temperature increase is equal to $30 - 35$ K. At $P = 3$ mbar energy input in the first pulse is small, and gas heating is absent. The main temperature increase takes place after the second pulse. Calculated temperatures at $P = 9$ mbar, 6 mbar and 3 mbar 3 μs after the discharge are 375 K, 400 K and 410 K, respectively. The specific deposited energy increases by 1.7 times when pressure decreases, from $w = 76.5 \cdot 10^{-3}$ eV/mol at 9 mbar to $w = 129 \cdot 10^{-3}$ eV/mol at 3 mbar. The main reason for different relative values of gas heating $(\Delta T/T)$ and specific energy input $(\Delta w/w)$ is the dynamics of fast gas heating. Indeed, figure 2.13 presents fraction of a discharge energy η_R which goes to fast gas heating for different gas pressures. It is obvious that for a fixed time the value η_R increases with pressure due to an increase in the quenching frequency of elecronically excited atoms and molecules. At a typical time $t > 40 - 50$ μs η_R reaches its quasistationary value, equal to $\eta_R \approx 24\%$.

Figure 2.14 presents the relative roles of different processes in the mechanism of fast gas heating under the considered conditions of moderate pressures and reduced electric fields within a range of $200 - 400$ Td. The main energy release takes place in reactions of the quenching of electronically excited nitrogen molecules, such as $N_2(B^3\Pi_g, C^3\Pi_u)$ by
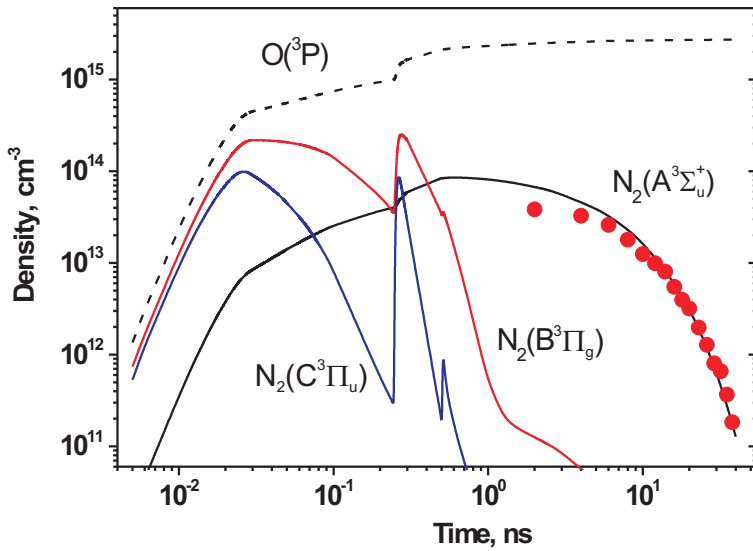
Figure 2.11: Kinetic curves for main excited species at gas pressure $P = 6$ mbar. Experimental points for $N_2(A^3\Sigma_u^+)$ are given in arbitrary units.

oxygen and the quenching of excited $O(^1D)$ atoms by N_2. These processes provide about 65% of the total gas heating. The pressure range of $3 - 9$ mbar is a boundary range, wherein the radiative quenching of the $N_2(C^3\Pi_u)$ to the $N_2(B^3\Pi_g)$ state with following collisional quenching is replaced by collisional quenching of $N_2(C^3\Pi_u)$. So, with pressure decrease, the input of the collisional quenching of the $N_2(B^3\Pi_g)$ and $N_2(C^3\Pi_u)$ states to gas heating becomes less important. At the same time, heating due to electron–ion recombination increases because of E/N increase.

According to calculations, under given experimental conditions at $50 - 100$ μs after the discharge the energy branching in the process of fast gas heating is the following: approximately 24% of the energy goes to gas heating, $43 - 47\%$ (depending upon gas pressure) to dissociation of molecular oxygen and the rest to vibrational excitation of molecular nitrogen. This distribution is determined, first of all, by dynamics of the reduced electric field (see figure 2.7). The main energy release takes place at $E/N = 200 - 400$ Td, and this leads to efficient gas heating via relaxation of electronically excited states and dissociation of molecular oxygen. It should be noted that the energy cost of atomic oxygen production is rather high: $G = 18 - 19$ (here G is a number of oxygen atoms produced for 100 eV of deposited energy), which is close to a maximum value possible for gas discharges in air.

2.6 Conclusions

Experimental studies of parameters of a spatially uniform nanosecond discharge in air in a pressure range $3 - 9$ mbar have been made. Temporal behavior of the discharge current,
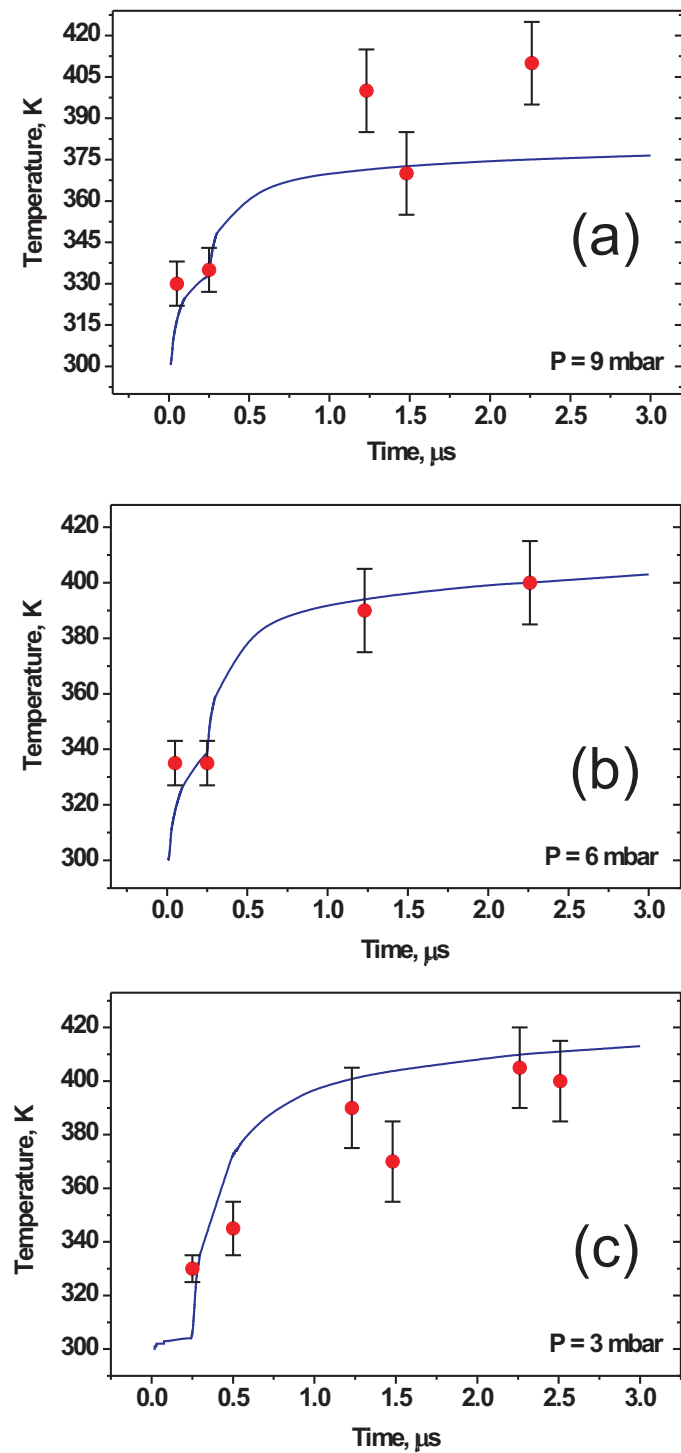
Figure 2.12: Gas temperature *vs* time. Symbols — experimental data, curves — results of calculations.
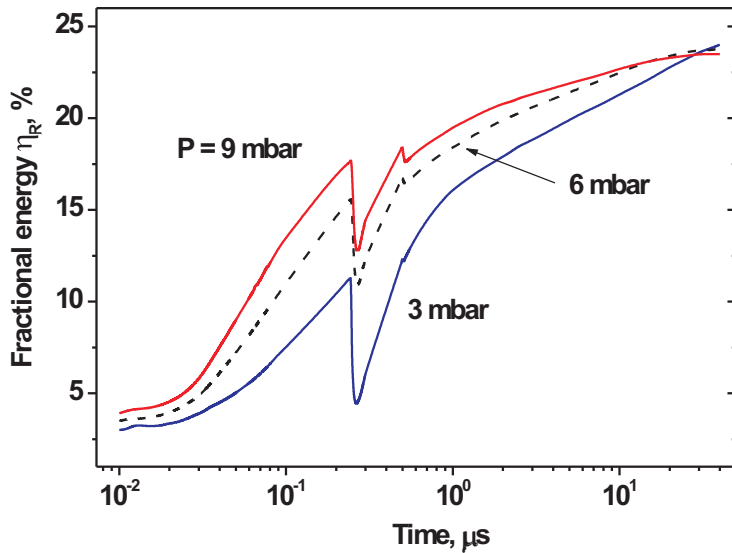
Figure 2.13: Fraction of discharge energy η_R *vs* time which goes to fast gas heating for different gas pressures.

reduced electric field E/N and specific deposited energy were measured. The data was used for development and verification of a numerical model of kinetics in the discharge. Due to the relatively small diameter of the discharge tube, the current density was high (160-200 A/cm^2). This provided high specific deposited energy $(0.1 - 0.13$ eV/molecule$)$ at reduced electric fields of $200 - 400$ Td.

The evolution of gas temperature has been studied in the discharge and in the afterglow. The temperature was measured from the rotational structure of the second positive system of molecular nitrogen. The data in the afterglow was obtained with the help of additional nanosecond pulses of relatively low intensity. Thus, fast gas heating in an N$_2$:O$_2$=4:1 mixture has been measured for the first time with well–controlled electric fields and specific energy input during the discharge stage for $E/N = 200 - 400$ Td. The results prove that the main energy input to gas heating takes place at time typical for quenching of electronically excited states of molecular nitrogen.

The results of numerical calculations based on a given experimental electric current profile versus time are presented. The calculations were carried out in the framework of a 0D kinetic model, taking into account the detailed kinetics of charged and excited species. To describe gas heating, a kinetic mechanism [1, 28] has been used. The calculated behavior of the electric field and specific deposited energy is in good agreement with the experiments, which proves that the model describes correctly electric field and processes of ionization.

There exists a set of processes with unknown percentage of energy release to fast gas heating. Among them are the reactions of N$_2$(C$^3\Pi_u$) quenching by molecular oxygen and reactions of electron–ion and ion–ion recombination. As far as the influence of these reactions decreases with pressure, study of fast gas heating at relatively low gas pressures

25
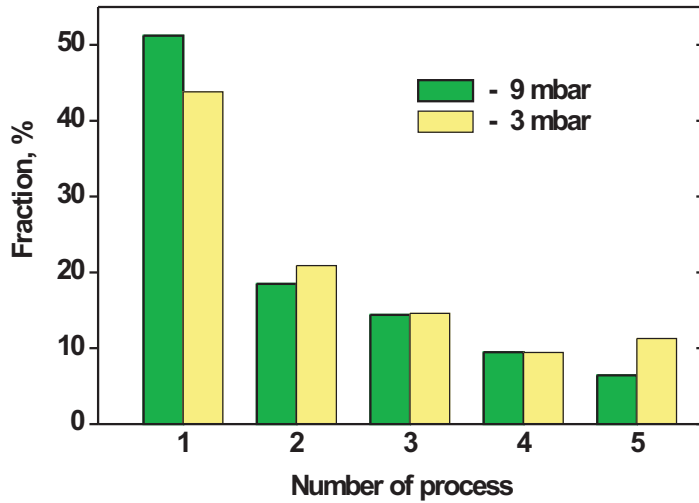
Figure 2.14: Distribution of energy release in fast gas heating between different processes under experimental conditions of the present paper: 1 — quenching of $N_2(B^3\Pi_g)$, $N_2(C^3\Pi_u)$ by O_2 (R6, R10); 2 — quenching of $O(^1D)$ by N_2; 3 — dissociation of N_2 and O_2 by an electron impact (2.10); 4 — quenching of $N_2(A^3\Sigma_u^+)$, $N_2(a'^1\Sigma_u^-)$ by O_2 (R1, R8), 5 — reactions of dissociative electron-ion recombination of N_2^+ and O_2^+ (2.6,2.7)

can be considered as a basis for verification of the models suggested.

The main energy release in the model takes place in reactions of quenching of electronically excited nitrogen molecules, such as $N_2(A^3\Sigma_u^+, B^3\Pi_g, C^3\Pi_u, a'^1\Sigma_u^-)$ by oxygen, quenching of excited $O(^1D)$ atoms by N_2, and in reactions of nitrogen and oxygen dissociation by electron impact. These processes provide more than 80% of total gas heating. An agreement between experimental data and results of calculations of gas temperature has been obtained for pressures 3, 6 and 9 mbar. The observed temperature increase in the afterglow is connected with the relaxation of electronic excitation, namely relaxation of $O(^1D)$ and $N(^2D)$ atoms and $N_2(A^3\Sigma_u^+, B^3\Pi_g, C^3\Pi_u, a'^1\Sigma_u^-)$ molecules, so the suggestion concerning the mechanism of fast gas heating in [1] is confirmed experimentally. Typical times of these reactions do not exceed a few microseconds, which is why under our experimental conditions the main energy relaxation takes place during $50 - 100$ microseconds. During this time, about 24% of the discharge energy goes to fast gas heating.

Chapter 3

Study of a fast gas heating in a capillary nanosecond discharge. Discharge parameters and temperature increase in the afterglow.

3.1 Introduction

Experimental studies and numerical calculations of parameters of a spatially uniform nanosecond discharge in air in a pressure range $3 - 9$ mbar have been made in our recently published paper [39]. Temporal behavior of the discharge current, reduced electric field E/N and specific deposited energy were measured. The data was used for development and verification of a numerical model of kinetics in the discharge. Due to the relatively small diameter of the discharge tube, the current density was high enough (160-200 A/cm^2). This provided high specific deposited energy $(0.1 - 0.13$ eV/molecule) at reduced electric fields of $200 - 400$ Td. The evolution of gas temperature has been studied in the discharge and in the afterglow. The temperature was measured from the rotational structure of the second positive system of molecular nitrogen. The data in the afterglow was obtained with the help of additional nanosecond pulses of relatively low intensity. Thus, fast gas heating in an N$_2$:O$_2$=4:1 mixture has been measured with well–controlled electric fields and specific energy input during the discharge stage for $E/N = 200 - 400$ Td. The results prove that the main energy input to gas heating takes place at time typical for quenching of electronically excited states of molecular nitrogen.

The main energy release in the model takes place in reactions of quenching of electronically excited nitrogen molecules, such as N$_2$(A$^3\Sigma_u^+$, B$^3\Pi_g$, C$^3\Pi_u$, a'$^1\Sigma_u^-$) by oxygen, quenching of excited O(^{1}D) atoms by N$_2$, and in reactions of nitrogen and oxygen dissociation by electron impact. These processes provide more than 80% of total gas heating. An agreement between experimental data and results of calculations of gas temperature has been obtained for pressures 3, 6 and 9 mbar. The observed temperature increase in the afterglow is connected with the relaxation of electronic excitation, namely relaxation of O(^{1}D) and N(^{2}D) atoms and N$_2$(A$^3\Sigma_u^+$, B$^3\Pi_g$, C$^3\Pi_u$, a'$^1\Sigma_u^-$) molecules, so the

suggestions concerning the mechanism of fast gas heating in [1, 40, 39] were confirmed experimentally. Typical times of these reactions do not exceed a few microseconds, which is why under our experimental conditions the main energy relaxation takes place during $50 - 100$ microseconds. During this time, about 24% of the discharge energy goes to fast gas heating.

A few mechanisms describing fast gas heating in nitrogen-oxygen mixtures have been recently suggested [12, 13]. Paper [13] presents results of experiments in a surface nanosecond dielectric barrier discharge (SDBD) in air at atmospheric pressure together with numerical calculations. To explain high values of temperature increase at a given energy input, the authors [13] suggest that at high electric fields and high pressures all the energy released in ion–molecular reactions and in ion–ion recombination is spent on gas heating and leads to significant temperature increase. The scale of fast gas heating in very high electric fields $(600 - 1000 \text{ Td})$ is reported and demonstrates a good coincidence between the experiments and the model. Still, work [13] leaves a few questions connected with the complexity of experiments at high E/N; in particular, the measurements of specific deposited energy for spatially non–uniform SDBD discharge at high pressure are complicated.

The aim of the present part of the work was to perform the experiments similar to [39] at higher pressures keeping as uniform geometry as possible. For that, a fast ionization wave (FIW) propagation in a capillary discharge has been studied.
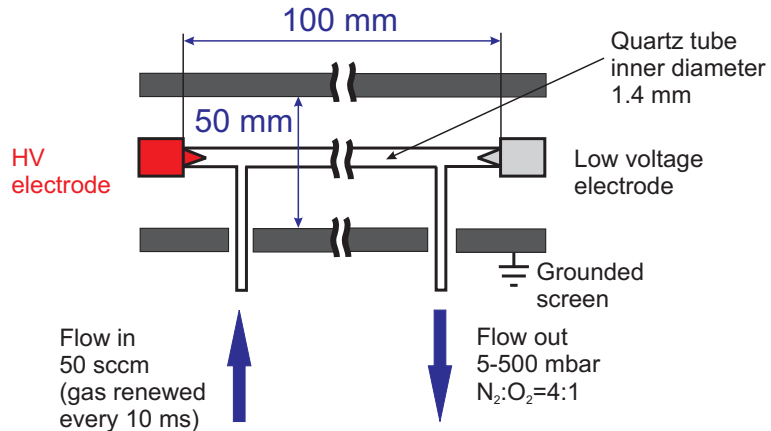
Figure 3.1: Scheme of the discharge tube.

3.1.1 Experimental setup

The present modification of the experimental setup consists of a quartz discharge capillary tube 1.4 mm inner diameter and 3.4 mm outer diameter. (see figure 3.1, for the details). Two needle gold–covered electrodes, 11 mm in length (8 mm of a cylindrical part of 1.3 mm in diameter, and 3 mm of a conical part) are placed at the ends of a capillary so that the interelectrode distance is equal to 80 mm. The electrodes are connected to the central wires of coaxial cables. The grounded cable shield is connected to two metal waveguide plates 60 mm wide, mounted above and below the quartz capillary so that the distance between the plates is equal to 56 mm.

28
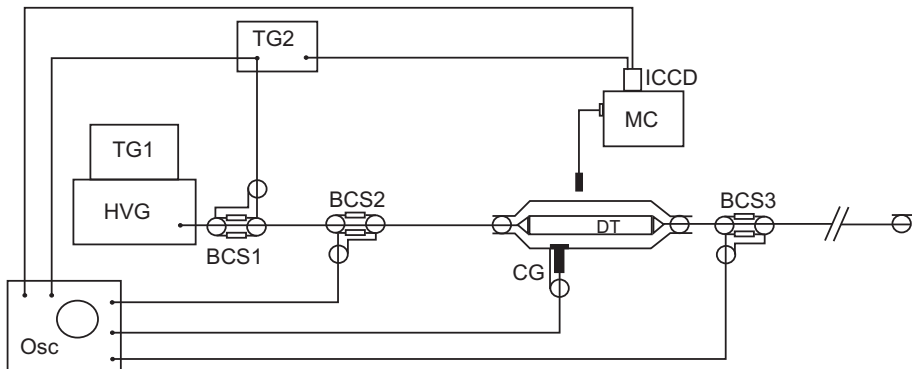
Figure 3.2: Scheme of the experimental setup. BCS1, BCS2 are the back current shunts (see text for explanations).
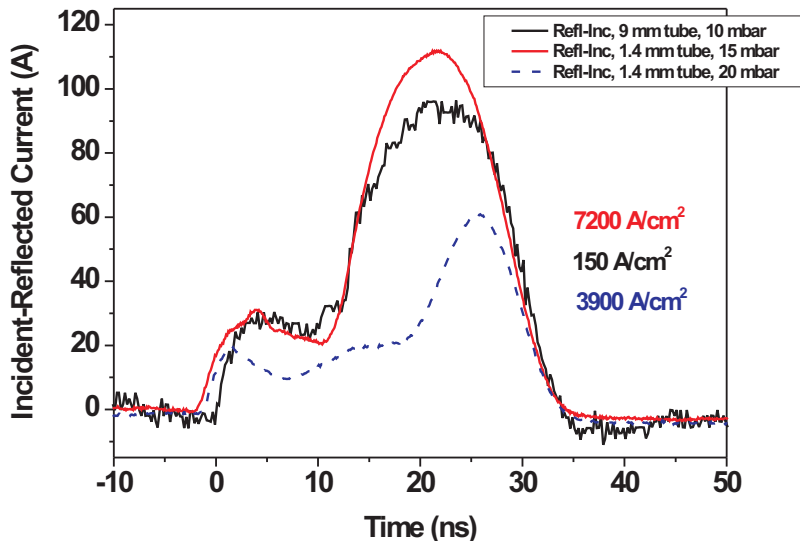

Figure 3.3: Comparison of current density observed experimentally in 9 mm and 1.4 mm diameter tubes.

Pulses with negative polarity, up to 18–20 kV amplitude on the high voltage electrode, 4 ns rise time, and 28 ns FWHM were applied to a high voltage electrode at 2–5 Hz frequency from a FID FPG 10–1MKS20 pulse generator (HVG at figure. 3.2) through a 25–m coaxial 50 Ohm RG213 cable. The low voltage electrode was connected to a coaxial cable 100 or 200 m in length used as a delay line to produce a supplementary nanosecond pulse.

Two quartz pipes 3 mm in diameter situated 10 mm apart the electrodes perpendicular to the tube axis are connected to 6 mm diameter plastic tubes and serve for a gas input and connection to the vacuum system. Synthetic air (N_2:O_2 mixture with a 99.9999% purity (Air Liquide) was used for the experiments). Experiments were carried out for gas pressures between 1 and 850 mbar, but the main set of experiments was carried out for 5, 10, 20, 30, 40 and 50 mbar. Gas flow through the discharge tube was fixed to 50 sccm, to allow the complete change of a gas between the pulses at frequency of high voltage pulses

used in the experiments.

Electric current/voltage and electric field have been measured using back current shunts installed before and after the capillary. Discharge uniformity was estimated form the preliminary experiments on ICCD measurements. Gas temperature has been measured from the discharge emission in the discharge during a sequence of a few pulses and in the afterglow, using an additional excitation of the gas by a supplementary nanosecond discharge.

Three back current shunts were installed into a cable shield breaks at the different distances from the discharge tube. The first one, BCS0 at figure 3.2, was used for the synchronization of ICCD camera (Andor iStar DH734–18U–03). The second current shunt, BCS1, installed 12 m before the capillary tube, was used to measure the incident pulse of current and the pulse of current reflected from the discharge cell. And finally the third, BCS2, installed into the cable shield brake 12 m after the discharge cell, was used to measure the transmitted current pulse. The BCS1 and BCS2 back current shunts were calibrated in time response and in amplitude, so that it was possible to find out the absolute values of current through the discharge cell and voltage on the electrode.

Comparison between the two tubes, 9 mm and 1.4 mm in diameter (see Figure 3.3) leads to the conclusion that current density is similar for the similar values of gas pressure. This means that current density is more than an order of magnitude higher for the capillary discharge.

The energy deposited into the discharge cell has been calculated according ti the following expression:

$$W = \int\limits_{inc} \frac{U^2(t)}{Z}dt - \int\limits_{refl} \frac{U^2(t)}{Z}dt - \int\limits_{trans} \frac{U^2(t)}{Z}dt, \tag{3.1}$$

where the integration takes into account the difference between the energies of the incident from the generator, reflected from the discharge cell and transmitted through the discharge cell pulses, $U(t)$ is a voltage in the cable, and Z is the wave resistance of the cable, $Z = 50$ Ohm. The attenuation of the high voltage pulse in the cable (22 V/m) has been taken into account. Calibrated capacitive probe moved in a slit made in the upper grounded metal plague was used to measure the electric potential along the capillary and finally, to calculate the axial component of the electric field. Coaxial capacitance of a small values (330 pf, RS 239-163,coaxial low inductive capacitance) were used for the capacitive probe. This allows accurate detection of the pulse front with the temporal resolution of 0.2 ns limited by the bandwidth of the oscilloscope (LeCroy WR44Xi) but differentiate the signal itself. So, the characteristic time of the capacitive probe,$\tau = 23$ nsec, was found from the following equation [?]:

$$U(t) = A \left[V(t) + \frac{1}{\tau^*} \int\limits_0^t V(t')dt' \right], \tag{3.2}$$

where $U(t)$ is the voltage pulse shape in the cable and $V(t)$ is probe signal. Efficient time constant τ^* has been found experimentally.

The ICCD images of the discharge uniformity have been taken by Andor iStar DH734–18U–03 ICCD camera with a 2 ns minimal gate. As far as the visible optics was used, the long wavelength part of a second positive system of molecular nitrogen ($N_2(C^3\Pi_u \rightarrow$
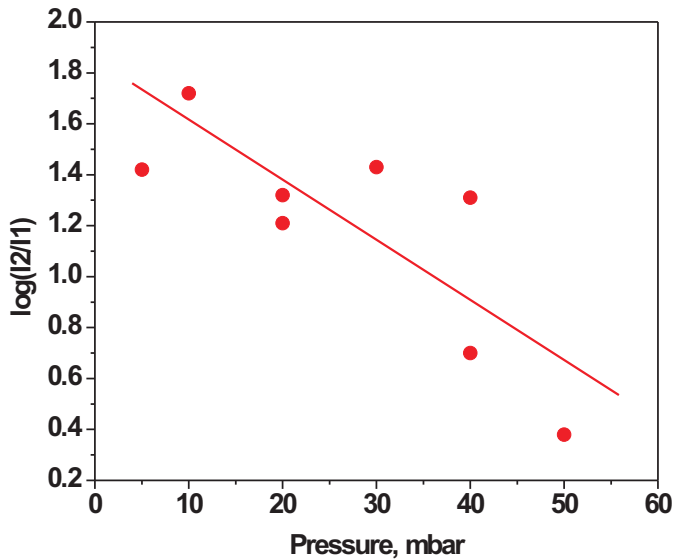
Figure 3.4: Ratio of the emission intensities inside the secondary nanosecond pulse (I2) and out of the pulse (I1) as a function of a gas pressure.
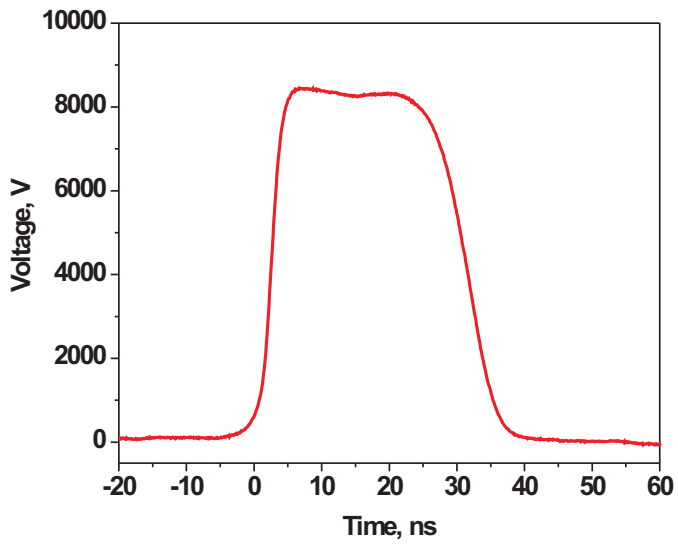

Figure 3.5: Typical incident high voltage pulse, signal from the BCS1.

$N_2(B^3\Pi_g)$)transition) was mainly collected. As far as a quenching rate constants of $N_2(C^3\Pi_u)$–state are equal to 10^{-11} cm^{-3}/s for molecular nitrogen and $2.7 \cdot 10^{-10}$ cm^{-3}/s for molecular oxygen respectively [22]. So, for the considered pressure the decay time is between tens and units of nanoseconds and, so, reflects the discharge homogeneity.

For gas temperature measurements, emission of the second positive system of molecular nitrogen has been registered for a wavelength range 347–360 nm, corresponding to

31

$0 \rightarrow 1$ at 357.7 nm, $1 \rightarrow 2$ at 353.7 nm and $2 \rightarrow 3$ vibrational transitions, . Emission spectra were measured with a UV–fiber optic–fed Andor SR303i spectrometer (grating with 2400 l/mm, operating range 190–700 nm, reverse linear dispersion 2.6 nm/mm) and Andor iStar DH734–18U–03 ICCD camera (spectral range 115–900 nm). The slit function was measured using Hg atomic line (Ocean Optics Hg–Ar lamp). In order to capture the entirety of the emission, a 50 or 100 ns gates were used. The ICCD camera gate monitor and voltage pulse waveforms were measured simultaneously with the oscilloscope in order to ensure timing accuracy. Emission measurements were taken in a few time instants, so that the camera gate was synchronized either with pulses from the generator or with secondary high voltage nanosecond pulses reflected from a 100 or 200 m cable used as a delay line. They provide the delay of emission measurements relative to the discharge within a range 1–2 μs. From 500 to 1000 accumulations were taken to get a good quality of the signal. To avoid a signal from the processes not caused by direct electron impact population of the $N_2(C^3\Pi_u)$–state, we compared the emission intensity with and without supplementary nanosecond pulse (Fig. 3.4). The Specair code [21] was used to simulate spectra with the slit function determined experimentally on the basis of the Hg line.

3.2 Results and discussion

A typical incident high voltage voltage in the cable is presented by figure **??**. In the present configuration of the experimental setup, three successive high voltage pulses were observed in the system due to reflections of the pulse from the discharge tube and then from the generator. Reflections from the generator corresponded to the end load $R_g = 0$, that is the current reflected with the same sign.

3.2.1 Transmitted current

Figure 3.6 presents, from top to bottom, three subsequent pulses of current passed through the discharge cell. The measurements are taken with the help of a back current shunt (BCS2). The gas pressure is a parameter and indicated in the figure. The highest values of current, 75–125 A, depending upon the gas pressure, are realized in the first pulse. The maximum current, 125 A in the peak corresponds to the gas pressure of 10 mbar. In the second pulse the current varies between 30 and 125 A, but the maximum of current is realized at $P = 5$ mbar. The explanation is in the fact that the first pulse was not enough for the efficient breakdown at 5 mbar, and was served rather as a source of pre-ionization. In the second pulse, current drops progressively with a gas pressure. In the third pulse the transmitted current is relatively weak, decreasing from 30 to 10 A with pressure.

3.2.2 Deposited energy and discharge spatial uniformity

The behavior of current is in a good correlation with the deposited energy. The deposited energy for the three subsequent pulses as a function of pressure is given by the Fig. 3.7. Filled and hollow symbols were obtained for the different systems of the high voltage electrodes: filled are obtained for the glued assembly of conical electrodes made of brass (the central cone is 1 mm in base diameter and 4 mm in height) while hollow symbols corresponded to the electrodes described in the section "Experimental setup" of the present
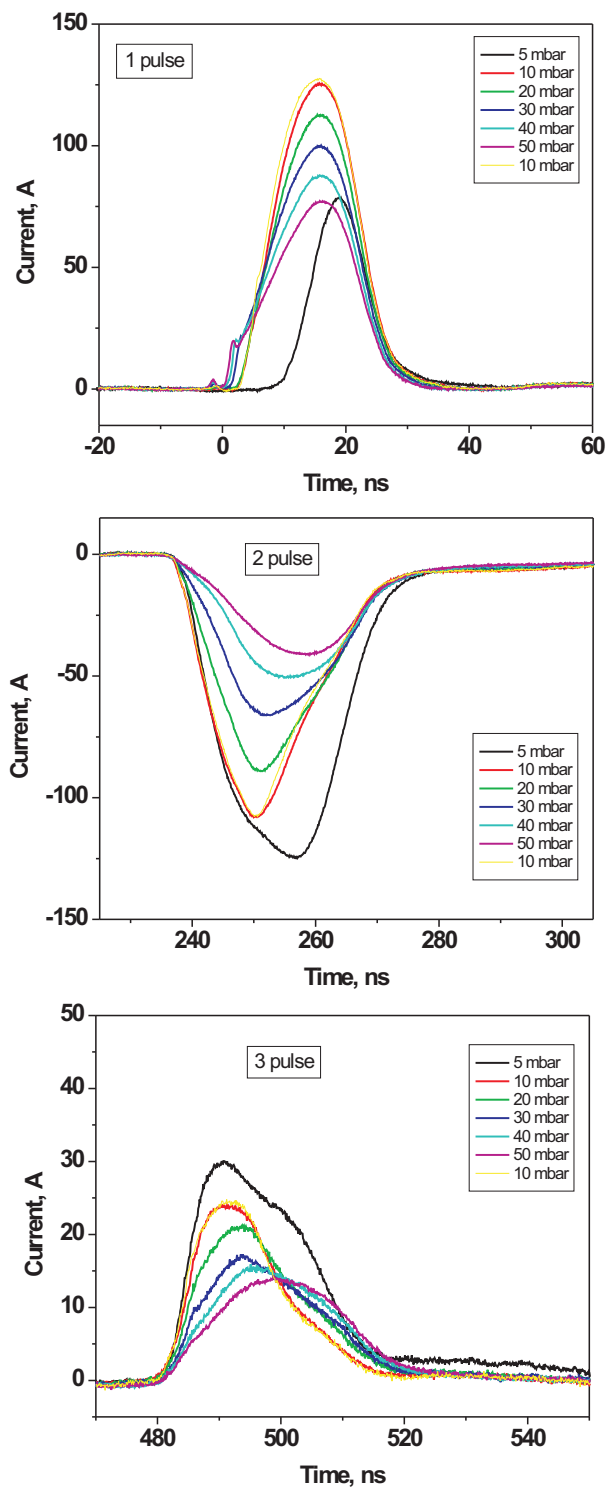
Figure 3.6: Current transmitted through the capillary tube, measured by a second back current shunt, BCS2.

Report. It is clearly seen that the difference is not significant and that the curves are
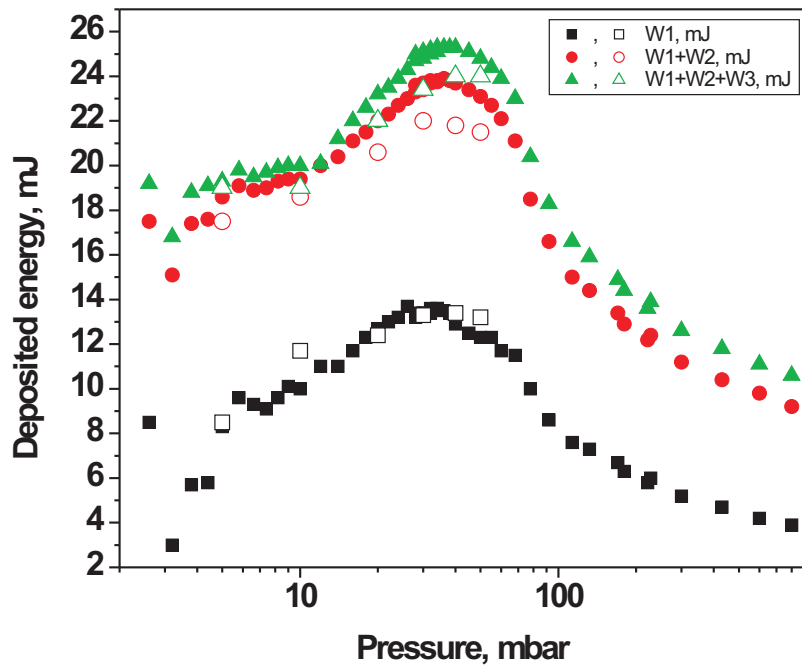
Figure 3.7: Deposited energy vs gas pressure. $W1$ is an energy deposited in the first pulse, $W1 + W2$ and $W1 + W2 + W3$ is an energy deposited in two and three successive pulses respectively (the explanations are given in the text).
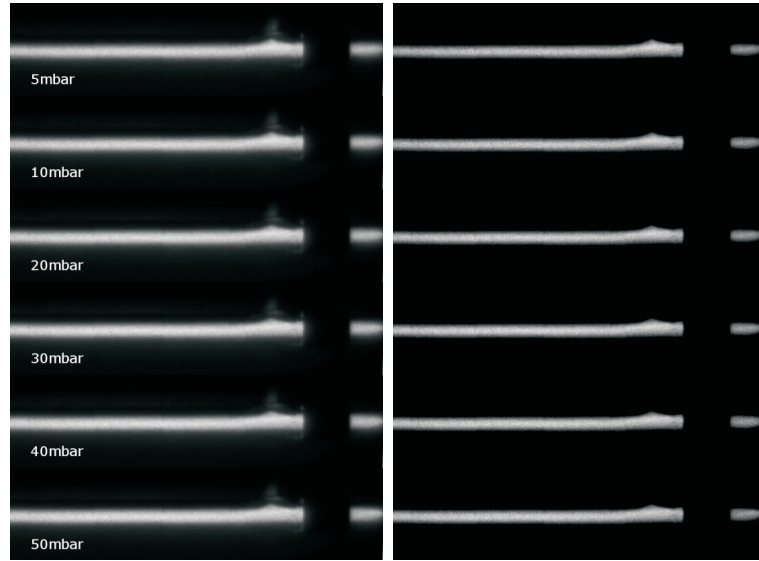

Figure 3.8: On the left hand side: discharge ICCD images for 5 work pressures, normalized in intensity. On the right hand side: the same images with removed pixels with the lowest 10% of intensity.

rather similar.

The deposited energy has a cupola shape with a relatively flat maximum between 20
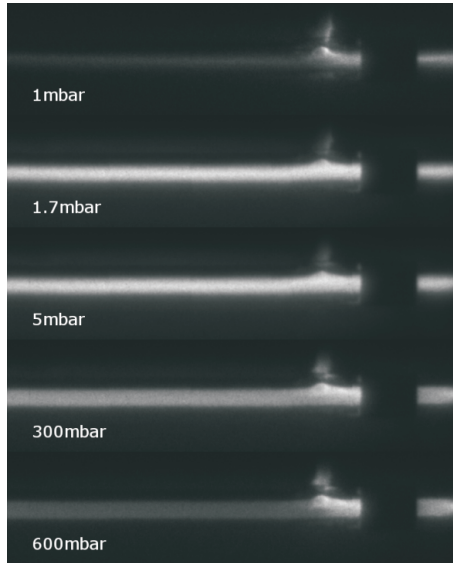
Figure 3.9: ICCD images of the discharge for a whole set of investigated pressures (1-600 mbar).

and 70 mbar. This curve, together with ICCD fast imaging, were a ground to choose the work pressure between 5 and 50 mbar. It is seen from the Figure that in the first pulse, maximum deposited energy is 13 mJ, this corresponds to 32.5% of the energy stored in the incident pulse (W_0 = 43 mJ). After two subsequent pulses, the percentage of the deposited energy increases to 60% (24 mJ) and practically does not change after the third pulse.

Preliminary ICCD fast imaging (figures 3.8 and 3.9) demonstrates a uniform emission from the discharge for work pressure region (5–50 mbar). As far as the images were taken with the gate of 2 ns, they reflect the emission of the second positive system of molecular nitrogen at the moment of taking the image and (for the lowest pressures) a few nanoseconds or tens of nanoseconds before. It is also must be taken into account that emission distribution in the cross–section has not yet been analyzed. Nevertheless, the preliminary conclusion is that the discharge demonstrates relatively uniform spatial structure.

It should be noted that for extra–low levels of deposited energy, less than 10% of the incident pulse, the discharge transforms to a non–uniform with glow concentrated near the high voltage electrode or between the high voltage electrode and side tube for a gas input. This fact is clearly seen in the figure 3.9 for the lowest (1 mbar and lower) and highest (600 mbar) pressures.

3.2.3 FIW velocity and electric field measurements

The data obtained by capacitive gauge, were used to calculate the axial electric field value and the velocity of a fast ionization wave propagation. It was assumed that the spatial sensitivity function of a capacitive detector is equal to a delta–function, or, what is the same, that the electric field does not change drastically on the scale of a sensitivity function of a capacitive detector, typically equal or close to the diameter of the grounded

screen.
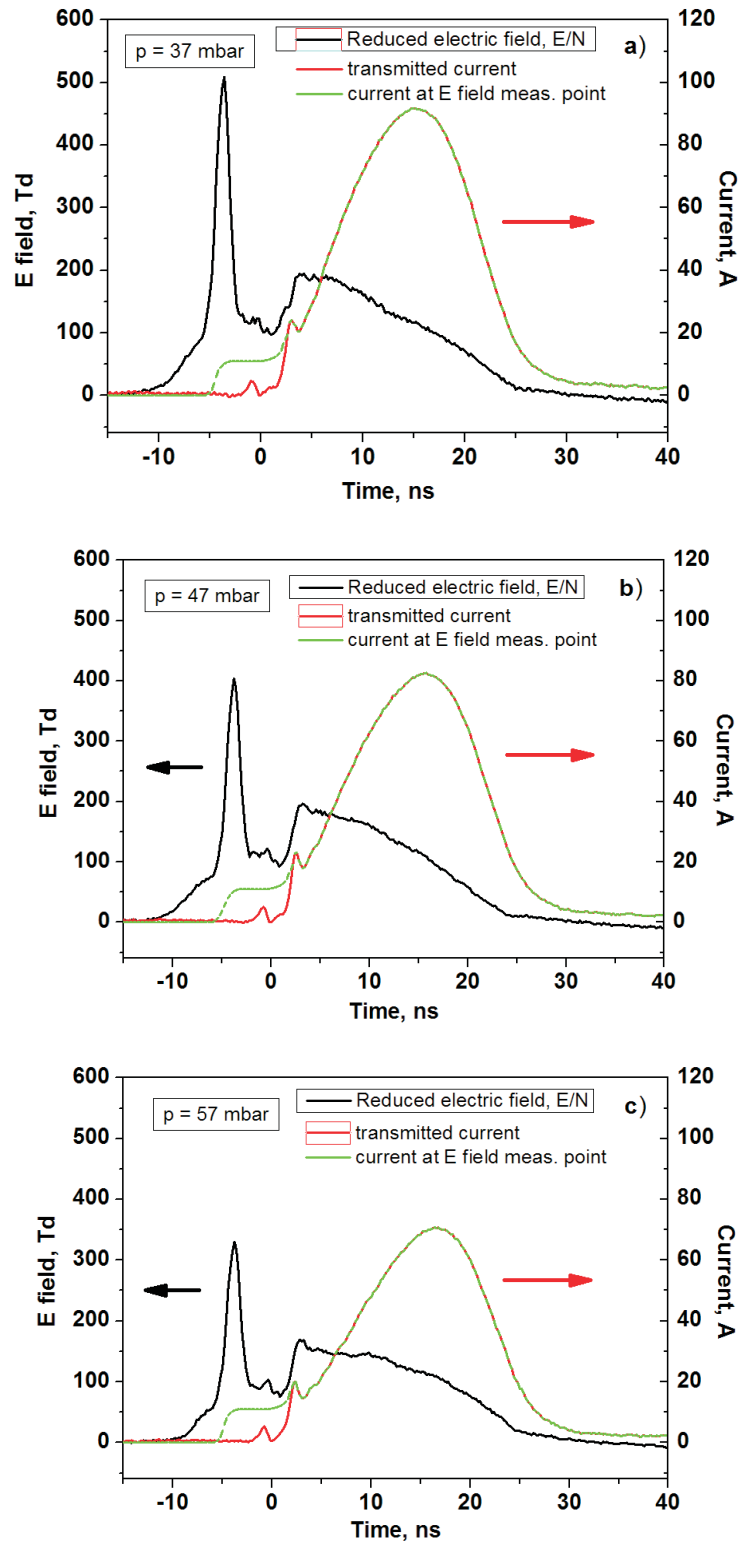
Figure 3.10: Electric field dynamics for different pressures at a distance $x = 5$ cm form the high–voltage electrode (in the middle of the discharge gap) for the first incident pulse. U=+11 kV in the cable.

The measured electric field values are represented in figure 3.10. It is clearly seen that two peaks of the electric field are observed. The first one, high and narrow, corresponds to the front of the ionization wave. The second observed peak of the electric field is formed about 5 ns after the front peak. It corresponds to the stage when the discharge gap is closed already by the FIW front; current and energy input are maximal on this stage.

The velocity of a fast ionization wave propagation in a capillary tube as a function of gas pressure is given by figure 3.11. For the given pressure range, a smooth slightly changing curve with maximum is observed for the velocity, the velocity is equal $1.3 - 1.4$ cm/ns.
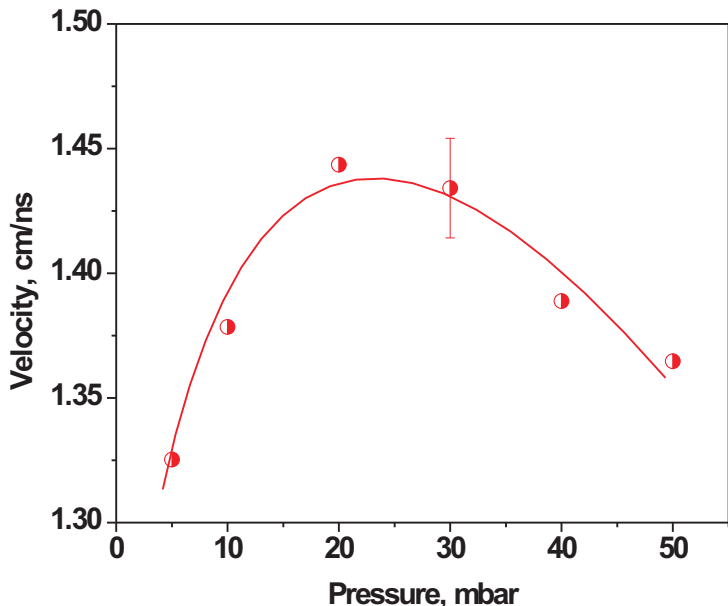
Figure 3.11: Velocity of a fast ionization wave propagation as a function of gas pressure.

3.2.4 Emission spectroscopy; measurements of rotational temperature

For each experiment, the spectra in the wavelength range 347–359 nm were taken to calculate rotational and vibrational temperatures. The spectra were treated using Specair code [21], and the quality of the approximation as well as the level of the error are clearly seen from the figure 3.12, were the rotational temperature value was determined as $T_{rot} = 1700 \pm 100$ K.

The only information obtained from the approximation of the vibrational temperature is that (i) the typical vibrational temperatures in the discharge are between 4000 and 5000 K; (ii) some increase of vibrational temperature is observed in the near afterglow, at $t = 1$ μs, with a subsequent relaxation to $3000 - 4000$ K at $t = 2$ μs and at longer times. Still obtained data seem to be rather scattered and do not give clear experimental trends. On the contrary, obtained rotational temperature values present a very clear
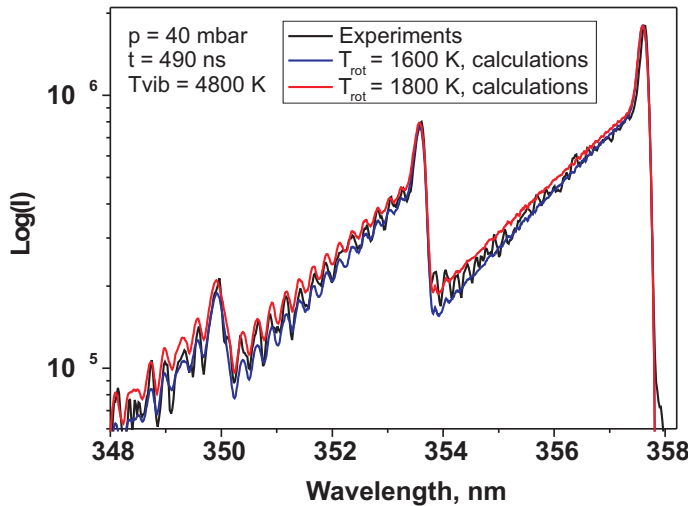
Figure 3.12: Typical emission for the wavelength treated for T_{rot} calculations; Specair calculations and comparison with experimental data.
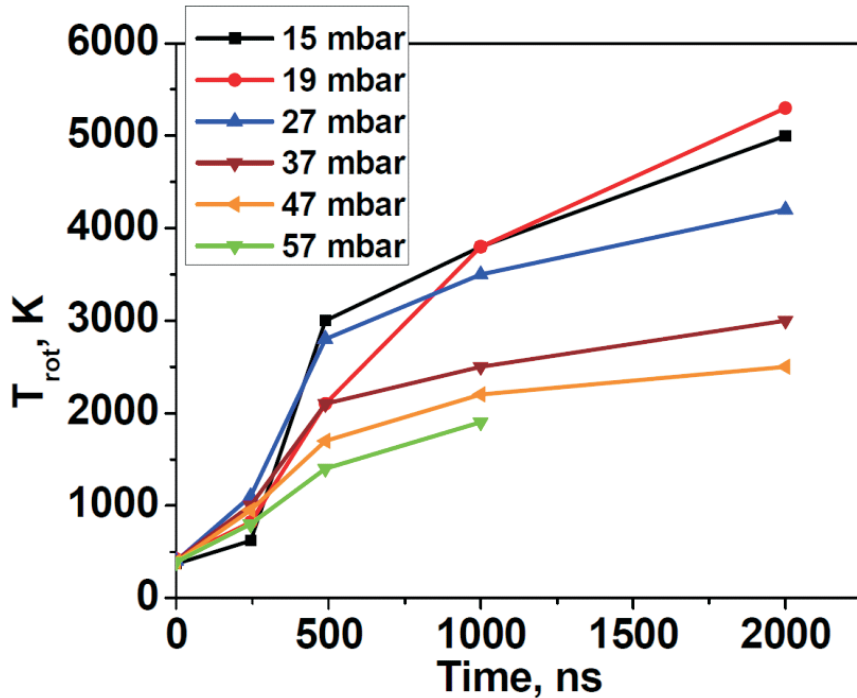
Figure 3.13: Rotational temperature T_{rot} determined on the basis of experimental measurements for a wavelength range between 347 and 359 nm.

trends (see figure 3.13)) except the data for $P = 10$ mbar. The additional check showed that the spectral data for 10 mbar are similar to those at other pressures, no artifacts were observed. If to summarize, all experimental regimes demonstrate significant (up to 5000 K) increase of a rotational temperature. Significant difference in behavior is still observed for $5 - 20$ mbar ("high" rotational temperatures) and $30 - 50$ mbar ("low" rotational temperatures). The most sharp increase is observed between the second and the third nanosecond pulses, at $t \approx 500$ ns.
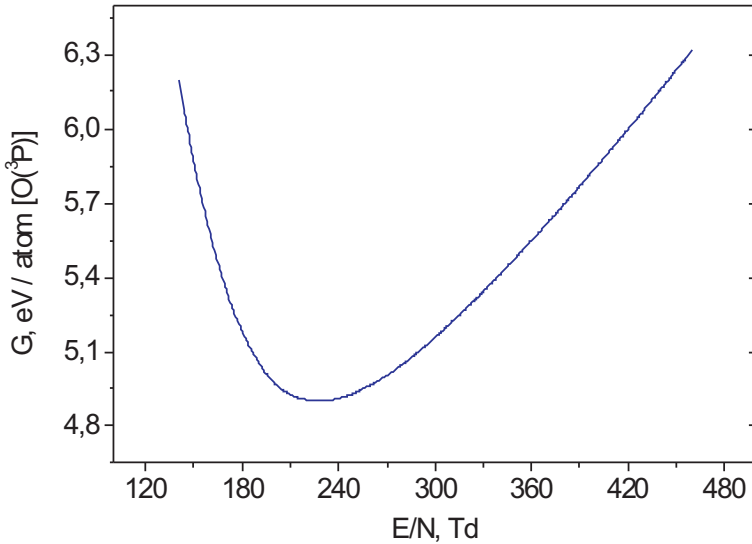
Figure 3.14: Energy efficiency of O(^{3}P) production in air, G, as a function of a reduced electric field E/N.

3.3 Discussion

Typical hydrodynamic times for the considered interval of temperatures $T = 2000-4000$ K are $\tau_g > 40 - 50$ μs for the meddle point of the discharge gap, $L = 5$ cm. This means that, from the point of view of hydrodynamics, for the times considered in our experiments ($t \leq 2$ μs)the gas density ρ_0 can be considered as a constant value.

Fig. 3.14 represents the energy efficiency of O(^{3}P) production in air, G, as a function of a reduced electric field E/N. The calculations are made with the help of BOLSIG+ code [26] assuming that the quenching of excited nitrogen states, $N_2(A^3\Sigma_u^+)$, $N_2(B^3\Pi_g)$ and $N_2(C^3\Pi_u)$, leads to dissociation of molecular oxygen. It is clearly seen that the energy efficiency is minimal at $E/N = 150 - 360$ Td. Within this interval, $G = 5 - 5.5$ eV/atom. Thus, in air (N_2:O_2=4:1) at energy inputs higher than 1.5 eV/molecule and reduced electric field $E/N = 150 - 360$ Td the major pat of molecular oxygen will dissociate.

Let us estimate a typical time of V–T relaxation of the vibrational energy stored in molecular nitrogen, $N_2(v)$. For gas pressure $P = 30$ mbar and total O_2 dissociation, the atomic oxygen density is equal to [O(^{3}P)]$\approx 3 \cdot 10^{17}$ cm^{-3}. According to [40], the rate constant of V–T relaxation of $N_2(v)$ on O–atoms comprises $k_{VT} = (5 - 6) \cdot 10^{-13}$ cm^{3}s at gas temperatures $T = 3000 - 4000$ K. This leads to the conclusion that a typical time of a V–T relaxation is longer than 5 μs and, under considered conditions, the influence of V–T relaxation can be neglected for $t < 2$ μs.

Quenching of electronically excited states $N_2(A^3\Sigma_u^+, B^3\Pi_u, C^3\Pi_u)$ of nitrogen by oxygen molecules is a dominant mechanism of fast gas heating at electric fields E/N lower than 400 Td. For high energy release and high dissociation degree in the discharge, kinetics of energy relaxation will change, namely quenching by atoms will become a primary quenching mechanism. Reactions of quenching of N(^{2}D,^{2}P), O(^{1}D,^{1}S) atoms and of $N_2(A^3\Sigma_u^+, B^3\Pi_u, C^3\Pi_u)$ molecules by atomic oxygen and nitrogen must be considered as

important candidates to be the leading process of the kinetic scheme. Their quenching leads to significant energy liberation into translational temperature.

A model of a fast gas heating under conditions of strong energy release and strong oxygen dissociation has been developed by Dr. Popov (Moscow State University) in continuation to previously developed models [1, 40]. Figure 3.15 represents, as a results of calculations, a part of the discharge energy spent to fast has heating, *vs* reduced electric field, E/N. The calculations are made for air for different degrees of dissociation of oxygen $\delta = 1 - [O_2]/[O_2]_0 = 0.5\,[O(^3P)]/[O_2]_0$. It is clearly seen that decrease of the electric field from $E/N = 160$ Td to $E/N = 40$ Td decreases the part of energy to gas heating for all values of the dissociation degree, δ. This can be explained by decrease of the part of the discharge energy spent to excitation of the electronic levels of atoms and molecules, and, consequently, with higher energy spent to vibrational excitation, $N_2(\nu)$.
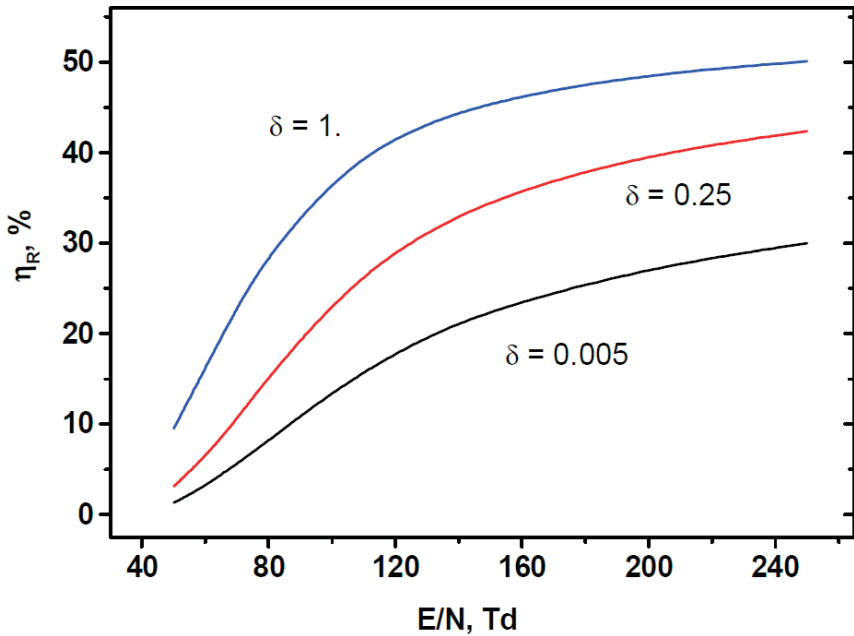
Figure 3.15: Part of the discharge energy spent to fast has heating, as a function of reduced electric field, E/N. The calculations are made for air for different degrees of dissociation of oxygen (see text for the explanations).

To compare the suggested theoretical model with the data of experiments, a few estimates of gas heating, ΔT, were made for each of the three discharge pulses. The estimates were made for the pressure $P = 47$ mbar. Deposited energies for the subsequent pulses are equal to 14.3, 10.4 and 2.2 mJ respectively. This corresponds, under given dimensions of the capillary, to volumetric energy inputs $W_{1,2,3} = 0.62, 0.45, 0.1$ eV/molec. The effective value of the electric field Eeff/N was calculated on the basis of the measured $E/N(t)$ profile

$$\frac{E_{eff}}{N} = \frac{\int_0^\tau j_e(t) \cdot E(t)dt}{N \cdot \int_0^\tau j_e(t)dt},$$

(3.3)

40

where $j_e(t)$ is the conduction current in the middle of the capillary. For given experimental conditions, the value $E_{eff}/N = 120$ Td has been obtained. This value was used for the further estimates.

The calculations were made assuming that quenching of $N_2(A^3\Sigma_u^+, B^3\Pi_u, C^3\Pi_u)$ states of molecular nitrogen takes place mainly on oxygen molecules leading to their dissociation. Energetic efficiency of production of atomic oxygen at $E/N = 120$ Td is equal to $G = 14$ (14 O-atoms for 100 eV of the deposited energy). So, the oxygen dissociation degree after the first voltage pulse will be equal to $\delta = 0.22$ (which corresponds to O–atoms density about $1.2 \cdot 10^{17}$ cm^{-3}), after the second and the third one — $\delta = 1$. Using the dissociation values, obtained theoretically, the estimates of the temperature increase, $\Delta T_1 = 516$ K, $\Delta T_2 = 742$ K, $\Delta T_3 = 240$ K (after first, second and third pulses), have been obtained from the calculated curves $\eta_R(E/N)$ (Figure **??**) and experimental data for deposited energy. It was taken into account that the adiabatic coefficient, $\gamma = C_p/C_v$, changes with increase of oxygen dissociation degree. The appropriate experimental data are $\Delta T_1 = 950 - 390 = 560$ K, $\Delta T_2 = 1700 - 950 = 750$ K, $\Delta T_3 = 2200 - 1700 = 500$ K.

Similar comparison for $P = 57$ mbar gives for calculations $\Delta T_1 = 426$ K, $\Delta T_2 = 612$ K, $\Delta T_3 = 188$ K, and for the experimental results $\Delta T_1 = 800 - 390 = 410$ K, $\Delta T_2 = 1400 - 800 = 600$ K, $\Delta T_3 = 1900 - 1400 = 500$ K. The results of calculations are in a good coincidence with the experiments for the two first pulses. The difference in calculated ΔT_3 and measured ΔT_3 temperature increase can be explained by additional gas heating in reaction $N(^4S) + NO = N_2(\nu = 4, 5) + O(^3P)$, which was not taken into account when plotting the dependence $\eta_R(E/N)$ presented in Figure 3.15.
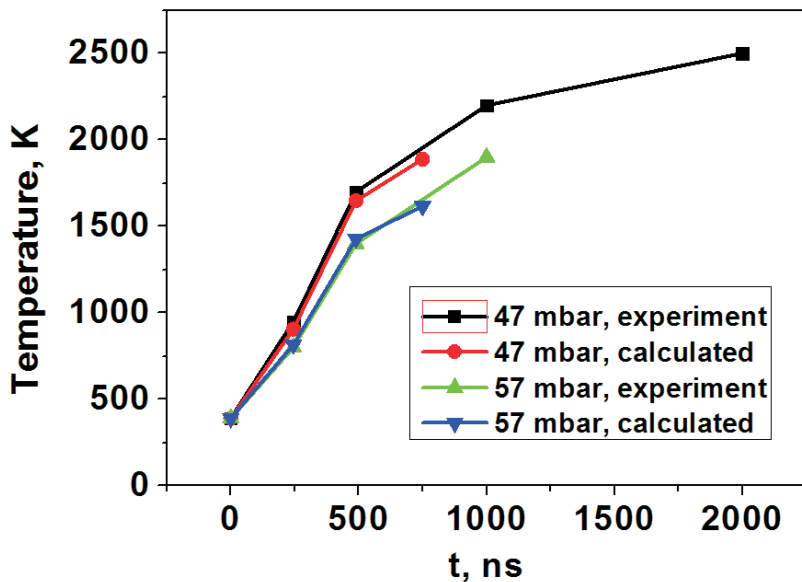
Figure 3.16: Deposited energy for the first pulse and for all the pulses. Comparison of experiments and preliminary numerical modelling.

Figure 3.16 represents comparison of calculated and measured temperature increase. It is seen that the coincidence is quite reasonable for all considered range of parameters.

3.4 Conclusions

So, the experimental data on fast ionization wave (FIW) development in capillary discharge have been obtained to verify the developed model of fast gas heating under the conditions of high electric field and spatially uniform discharge. Experiments have been performed in synthetic air for gas pressures between 10 and 60 mbar with more broad observations of the discharge itself, between 1 and 850 mbar. The data demonstrate significant increase of rotational temperature in the afterglow, $1-2$ μs after the discharge. Electric field values reach a few kV/cm in the discharge front and hundreds–thousand kV/cm after the front. Data on incident, transmitted and reflected current, electric field and temperature increase were obtained for 6 different gas pressures.

For all observed pressures, the electric field increases and decreases sharply in the front, corresponding to a breakdown stage, that is to the closing of the gap between the two electrodes. The width of the field peak is about 1.5–2 ns, and the field reaches at least 300–500 Td in the peak. Velocity of the ionization front propagation on this stage is equal to 1.3–1.4 cm/ns. After the closing of the gap, the field decreases, and a zone of minimal values of the electric field corresponds to a back wave and establishment of a a stationary potential at the low voltage electrode connected to a long cable. Then, in the zone of actively flowing current, the typical field values are within a range 100–200 Td. This corresponds to active dissociation and excitation of electronic levels. In the early afterglow of the discharge, within 1-2 microseconds after the pulse, a strong gas heating, up to thousands of K, is observed.

A model of the fast gas heating, developed for peculiar conditions of fast energy release in the discharge and strong dissociation degree, demonstrates a good coincidence with the measured gas temperatures at first two pulses, although in the third pulse the experimentally observed temperature is higher than predicted by theory. The obtained data, together with developed kinetic model, give a basis for description of the fast gas heating by short pulse discharges at high electric fields and high energy release at moderate pressures and high dissociation degree.

Chapter 4

Cavity ring–down spectroscopy. Measurements of $N_2(A^3\Sigma_u^+)$ density in afterglow of nanosecond discharge

4.1 Introduction

The work performed at Laboratoire EM2C (CNRS/Ecole Centrale Paris) has consisted in setting up the advanced diagnostic techniques to probe the concentration of metastable $N_2(A^3\Sigma_u^+)$ in the discharge. This technique was developed in previous studies at EM2C [42] and was adapted for use in the new reactor. Laser Cavity Ring-Down (CRD) absorption by N_2 $(A^3\Sigma_u^+)$ in the afterglow of a nanosecond discharge (time scale $2-200$ μs) has been measured for the following vibrational transitions (ν' , ν''): (2,0), (3,1), (4,2) and (5,3). Experiments were performed in pure nitrogen and in synthetic air for gas pressures of 3, 6, and 9 mbar. The corresponding absorption spectra have been obtained and the results can be converted into densities of the absorbing states using spectral simulations with the spectral line-by-line radiation SpecAir software. A first series of results has been obtained for the N_2 $(A^3\Sigma_u^+)$, nu''=0 absolute densities.

4.2 Cavity ring–down spectroscopy. Experimental setup.

Cavity Ring–Down Spectroscopy (CRDS) has been applied in the past twenty years to the detection of trace species and for plasma diagnostics [43]. One of its most attractive features is its very high sensitivity. Under conditions of weak absorption, the radiation intensity of a light source (e.g. lasers, lamps) $I(\nu)$ transmitted through a homogeneous gas sample is given by the Beer–Lambert law:

$$I(\nu) = I_0(\nu) \exp(k(\nu)l_{abs}), \tag{4.1}$$

where $I_0(\nu)$ is the incident intensity, k is the absorption coefficient, and l_{abs} is the absorption length. The absorption coefficient $k(\nu)$ is linked to the lower state number density, N_1, of the absorbing species by:
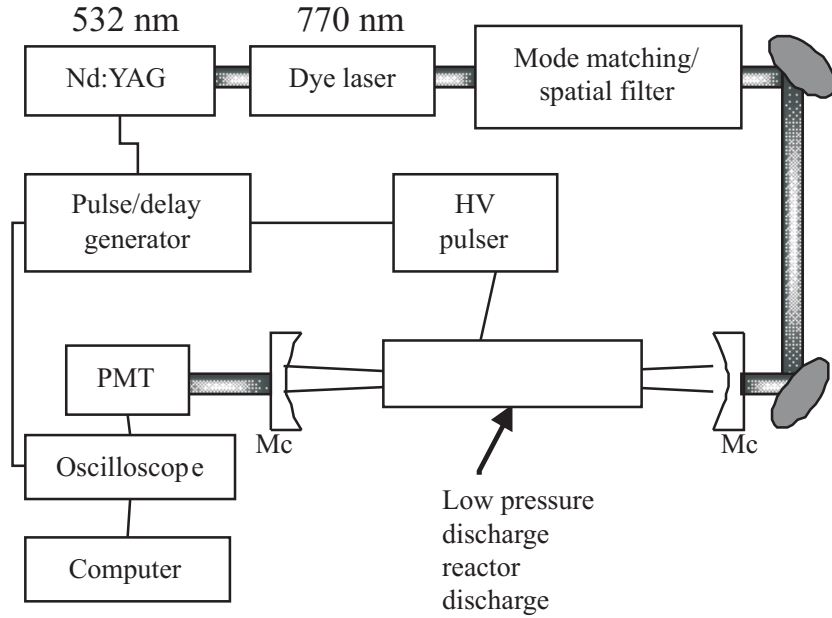
Figure 4.1: Schematic of the CRDS setup (Mc: mirror cavity)

$$k(\nu) = S(T)\varphi(\nu)N_1, \tag{4.2}$$

where $S(T)$ is the line strength of a specific absorption line at temperature T and $\varphi(\nu)$ is the normalized absorption coefficient profile function ($\int \varphi(\nu)d\nu = 1$). Thus, knowing the line strength and measuring the absorption coefficient absolute densities are obtained.

Reduced number densities and small plasma volumes (small l_{abs}) require advanced absorption techniques. Several approaches can be used to improve the detection sensitivity. One of the most effective techniques, CRDS using high–finesse optical cavities, allows for effective km–absorption lengths even in very small detection volumes.

In pulsed CRDS, a laser pulse is coupled into an optical cavity formed usually by two highly reflective mirrors. Each time the pulse reaches one of the mirrors a small fraction of the light leaks out. At the exit of the cavity a train of pulses decaying in time can be recorded with a photomultiplier tube (PMT). When the laser is tuned to an absorption transition of the species present inside the cavity, the decay of pulses is faster. The difference of the decay times, τ, for on– and off–resonance measurements is proportional to the absorption coefficient [43]:

$$k(\nu) = \frac{L}{cl_{abs}} \left(\frac{1}{\tau_{off-res}} - \frac{1}{\tau_{on-res}} \right), \tag{4.3}$$

where c is the speed of light and L is the cavity length. Equation (4.3) is valid if the density of the absorbing species is constant during the decay time. In [44, 45] it was shown that CRDS can be used for density measurements even if the species densities change during the ring–down time. Temporal resolutions of ms and μs respectively, were achieved. Recently we have shown that $N_2(A^3\Sigma_u^+)$ density can be measured with resolution down to $20 - 50$ ns [42]. The temporal evolution of the species density is given by the following expression:

Table 4.1: Ranges of the various spectral scans, and wavelengths selected for the temporal measurements

Transition (B,A)	Wavelengths, nm	Line position, nm
2-0	769.5-770.1	769.730
3-1	762.23-763.03	762.525
4-2	744.28-744.88	744.580
5-3	736.28 - 737.1	736.595

$$N_1(t) = \frac{1}{S(T)\varphi(\nu)} \cdot \frac{L}{cl_{abs}} \frac{d}{dt}\left(\ln \frac{I_{off-res}}{I_{on-res}}\right), \tag{4.4}$$

where $I_{off-res}$ and I_{on-res} are the decay intensities measured at different wavelengths corresponding to off– and on–resonance, respectively. The derivative of the logarithm of the ratio of these functions must be calculated, and based on spectroscopic data the temporal evolution of the density is obtained.

The setup for CRDS to diagnose the fast thermochemistry in the reactor is shown in Fig. 4.1. The discharge cell consists of a quartz tube with hollow metal electrodes (the diameter of the orifice in each electrode is 5 mm), the distance between electrodes is 20 cm, and the tube diameter is 9 mm. High–voltage pulses of 10 kV amplitude and 30 ns duration with pulse repetition rate 2 Hz were used. The tube is connected to two glass side tubes with valves to pump and fill the system with a gas. The end plates of the glass tubes are the CRDS mirrors separated by 78 cm. The working pressures were 3–9 mbar. All the experiments were performed with a gas flow (synthetic air or pure nitrogen) with typical flow rate 10–30 sccm, enough for mixture renewing between high–voltage pulses. The uniformity of the discharge between the electrodes has been checked, it was proved that the discharge is mainly confined between the electrodes without significant penetration to the side tubes.

The CRDS cavity consisted of two plano-concave mirrors (Los Gatos Research) of reflectivity R ¿ 99.7 % and radius of curvature $r = 0.5$ m. The beam of a tunable pulsed dye laser, Continuum ND 6000, pumped with a Precision PL 8010 Nd:YAG laser was used to initiate the cavity ring–down signal. The repetition frequency used of both laser and discharge was equal to 2 Hz. The delay between the high–voltage discharge and probe laser pulse was adjusted with the help of Berkeley Nucleonics 555 four channel gate and delay generator.

For each vibrational level, a scan of the laser wavelength in the appropriate region was performed with a spectral step of 5 pm. This procedure allowed us to select the strongest and most isolated absorption rotational lines. All measurements of the temporal behavior of $N_2(A^3\Sigma_u^+)$ were then performed at the fixed wavelengths indicated in Table 4.1.

Absorption in the 2–0 vibrational transition of first positive ($A^3\Sigma_u^+ \rightarrow B^3\Pi_g$) nitrogen system was used to get the population of zero vibrational level of $N_2(A^3\Sigma_u^+)$. The CRD signal was measured at the maximum of the unresolved $Q_1(22)$ and $Q_3(16)$ lines structure at the wavelength of 769.945 nm. Because, typically for dye lasers, the laser pulse–to–pulse intensity varies significantly, we averaged 50 signals for each regime.

The typical experimental CRD signals with and without discharge are presented in

Fig. 4.2. When $N_2(A^3\Sigma_u^+)$ molecules present in the system, the CRD signal decay occurs faster, and the decay time gives us information about the concentration of the absorber $N_2(A^3\Sigma_u^+,\ v=0)$.

Experimental setup allowed us to vary the delay between high-voltage pulse, where production of $N_2(A^3\Sigma_u^+)$ occurs, and laser pulse, so the concentration could be measured in a wide region (hundreds of μs). The typical decay time in empty cavity was close to 2 μs, and this parameter determines our temporal resolution. Thus, the fast processes (a few μs) of $N_2(A^3\Sigma_u^+)$ formation were beyond the limits of our investigations.

The absorption line FWHM was determined mainly by the Doppler broadening, which is in our case is $1.8 - 2.1$ pm (depending on the temperature in the afterglow). These values are significantly higher than the collisional broadening, which is $0.1 - 0.4$ pm for the working pressures of 3-9 torr.

The laser FWHM was 6 pm, which is greater than the absorption line width. In this case the classical mono–exponential approximation of CRD signal

$$I(t) = I_0 \cdot \exp\left[-\frac{c}{L}\left((1-R) + k(\nu_0)l_{abs}\right)t\right] \tag{4.5}$$

is not applicable, because we need to take into account not only absorption coefficient $k(\nu_0)$ at the line intensity maximum (or at any other point where measurements were performed), but all the coefficients along the contour of the line, each with its own laser intensity $I(\nu)$ (detailed information about this aspect of CRDS could be found, for example, in [46]). Thus, CRD signal is not exponential any more, and should be described by the following equation:

$$I(t) = \sum_m I_0(\nu) \cdot \exp\left[-\frac{c}{L}\left((1-R) + k(\nu)l_{abs}\right)t\right], \tag{4.6}$$

where the summation goes over all cavity modes. The free spectral range of cavity in our case is approximately 0.4 pm, so we have enough longitudinal modes under the absorption line contour to replace summation by integration. Moreover, because of signal averaging, we have a displacement of mode position from pulse to pulse because of mirrors microvibration, so we can treat modes pattern as a quasicontinuum.

Numerical code was written to simulate this multi-exponential approximation, the results are presented in Fig. **??**. Good correlation between experimental and simulated spectrum was obtained in a wide range of absorption coefficients (which corresponds to different delays between the discharge and laser pulse).

4.3 Absorption coefficients

The experiments were carried out changing the delay between the discharge and a laser pulse, so that we were able to trace the decay of the absorption coefficients. Obtained absorption coefficients K, directly proportional to the $N_2(A^3\Sigma_u^+,\ v=0,1,2,3)$ density, are shown in Fig. 4.3, 4.5, 4.7 and 4.8 for synthetic air and in fig. 4.4, 4.6, refn22 and 4.10 for pure nitrogen.

Coming back to the complex procedure of the CRD decay treatment taking into account non–monoexponential behavior of emission decay in laser cavity, it should be mentioned that at low absorption, for time intervals $t > 15$ μs for air and $t > 75$ μs for
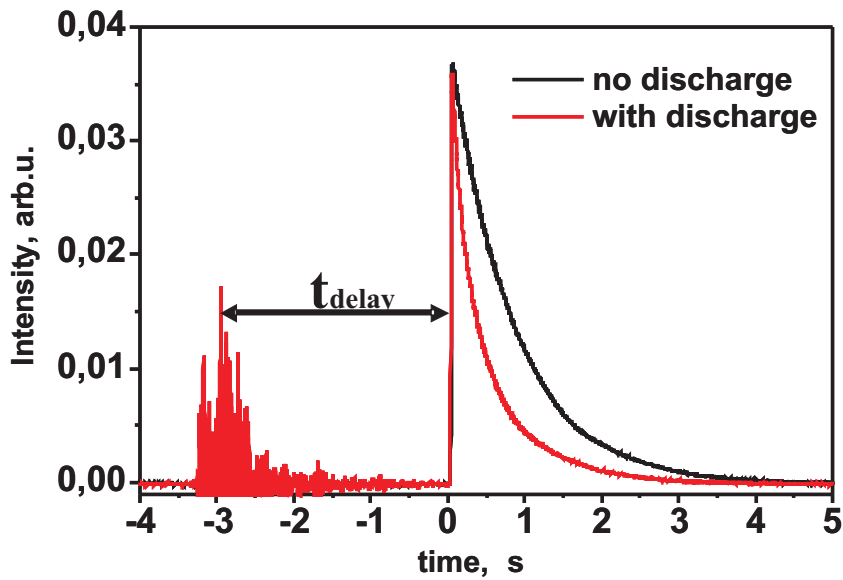
Figure 4.2: Typical CRD signal with and without discharge)
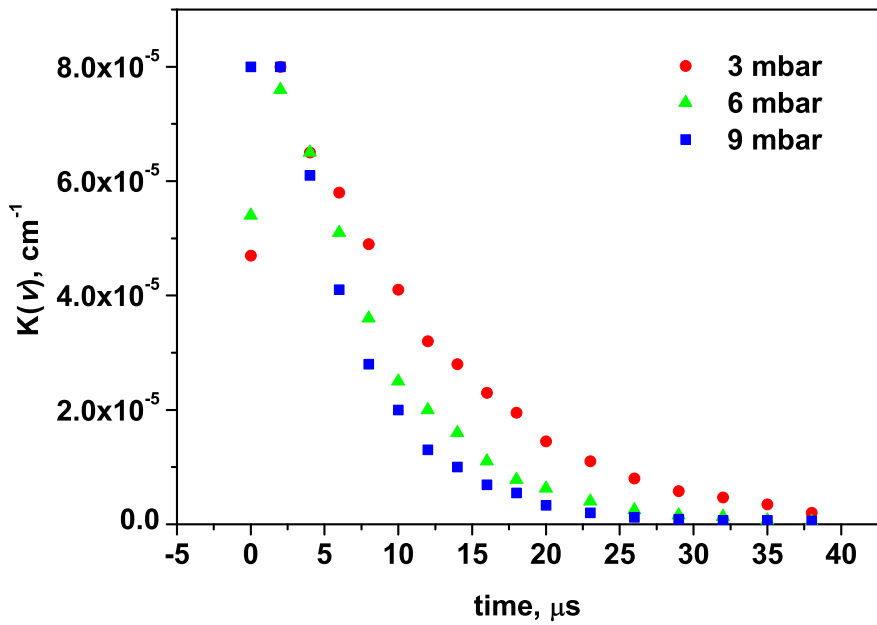
Figure 4.3: Absorption coefficient for $N_2(A^3\Sigma_u^+, v=0)$ in air

nitrogen, the decay is monoexponential, and simple procedure of data treatment gives the same absorption coefficients. This can be considered as an additional check of the validity of obtained K values.

Figs. 4.3 and 4.4 present the absorption coefficient for $0-2$ transition in air and nitrogen. The decay in air occurs significantly faster (with typical times 10-20 μs, depending on the pressure) than in the nitrogen because of effective $N_2(A^3\Sigma_u^+, v=0,1,2)$

47

quenching on the oxygen molecules. The decay rate increases with pressure. In nitrogen, concentration decay goes slower (40 μs) and weakly depends on pressure. If plot in $(1/K, t)$ coordinates, the dependence becomes close to linear. This fact indicates that the main channel of $N_2(A^3\Sigma_u^+)$ quenching in the pure nitrogen is the reaction between two $N_2(A^3\Sigma_u^+)$ molecules: $N_2(A^3\Sigma_u^+) + N_2(A^3\Sigma_u^+) = N_2(C^3\Pi_u, B^3\Pi_g) + N_2(X)$.

Density as a function of time is rather similar to $1 - 3$ (Figs 4.5 and 4.6) and $2 - 4$ (Figs 4.7 and 4.9) transitions, the absorption coefficient is the highest for the second vibrational level.

4.4   SpecAir software: new capabilities

To perform modeling of the measured absorption spectra, we used the SpecAir software in its version 3.0 that was just released (see Figure 4.11). The previous version had a lower temperature limitation of 1000 K; which did not allow modeling the spectra obtained in the present work since in our case the rotational temperature is certainly less than 400 K. Thus, with the previous version we had only been able to check the line positions and identify the transitions in the experimental spectra.

With the new version, all temperatures (T_{rot}, T_{vib}, T_{el} and T_{tr}) can be varied independently even at low temperatures, thus making it possible to determine the parameters of the discharge. For example, for a given vibrational transition, we can vary the rotational temperature in order to get the best fit with the experimental spectrum. In addition, absolute densities of the absorbing levels can now be determined.

Many other changes were made in the new version. The analysis of experimental
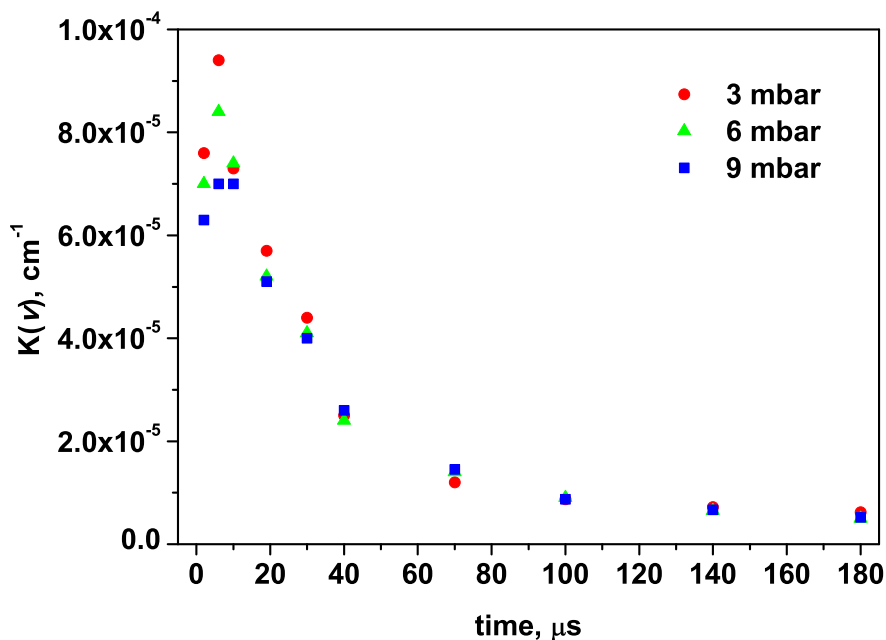
Figure 4.4: Absorption coefficient for $N_2(A^3\Sigma_u^+$, v=0) in nitrogen
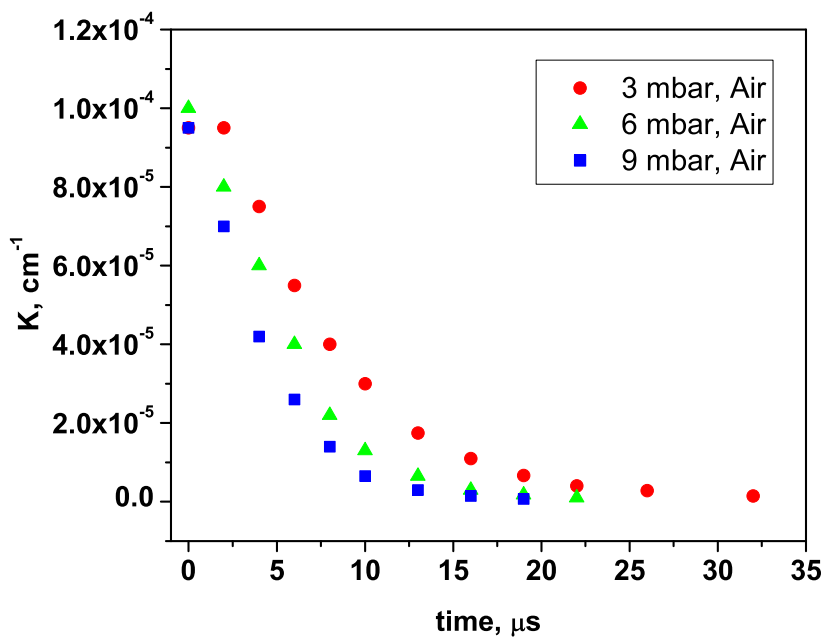
Figure 4.5: Absorption coefficient for $N_2(A^3\Sigma_u^+, v=1)$ in air
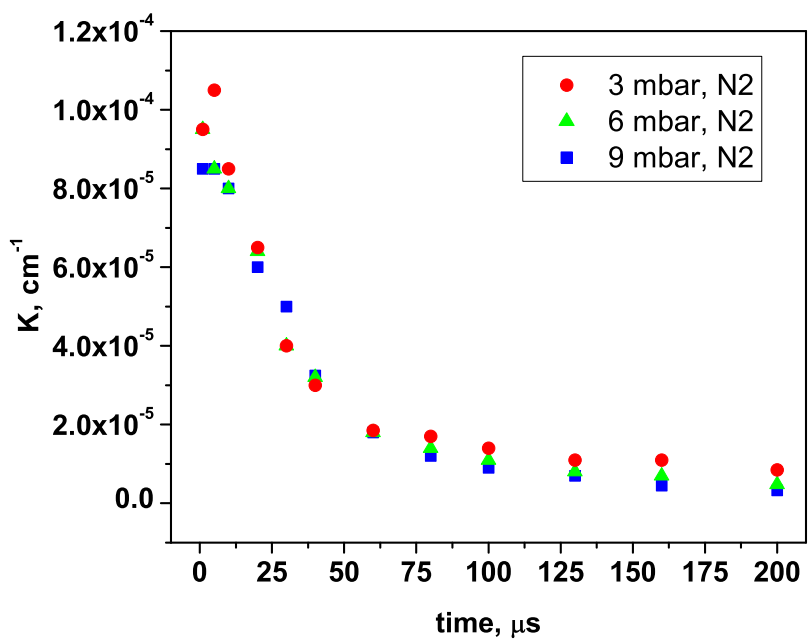
Figure 4.6: Absorption coefficient for $N_2(A^3\Sigma_u^+, v=1)$ in nitrogen

49
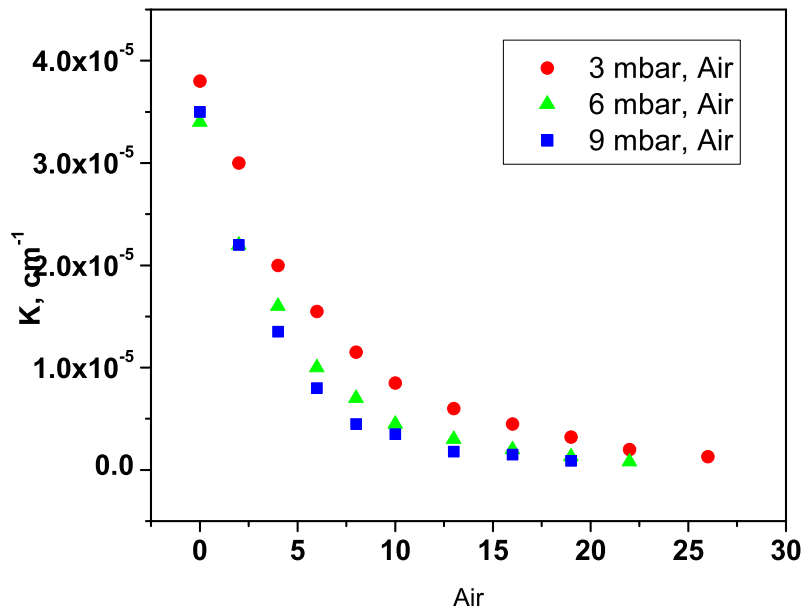
Figure 4.7: Absorption coefficient for $N_2(A^3\Sigma_u^+, v=2)$ in air
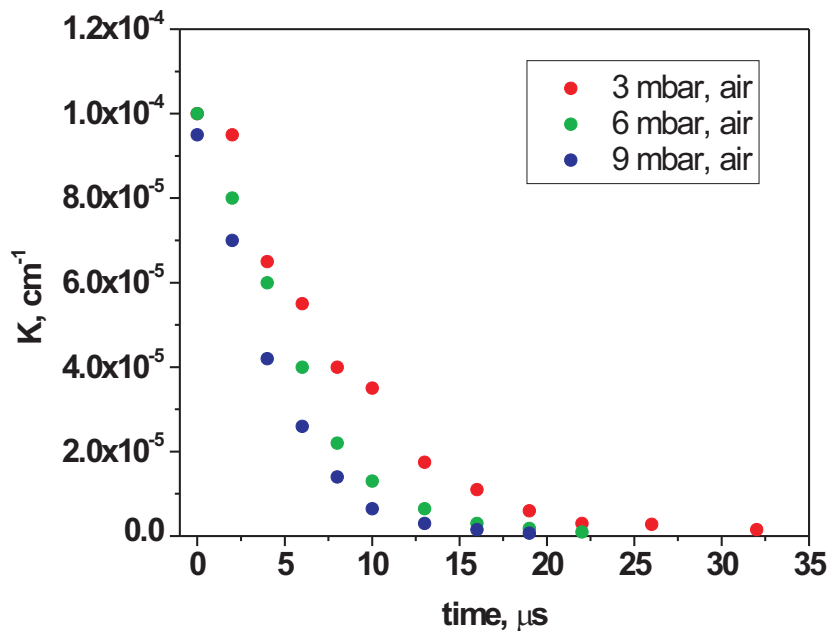
Figure 4.8: Absorption coefficient for $N_2(A^3\Sigma_u^+, v=3)$ in air

spectra is simplified by the ability to import experimental spectra inside SpecAir, allowing

50

fast and effective comparison of the simulations with the experiment. In addition, a new
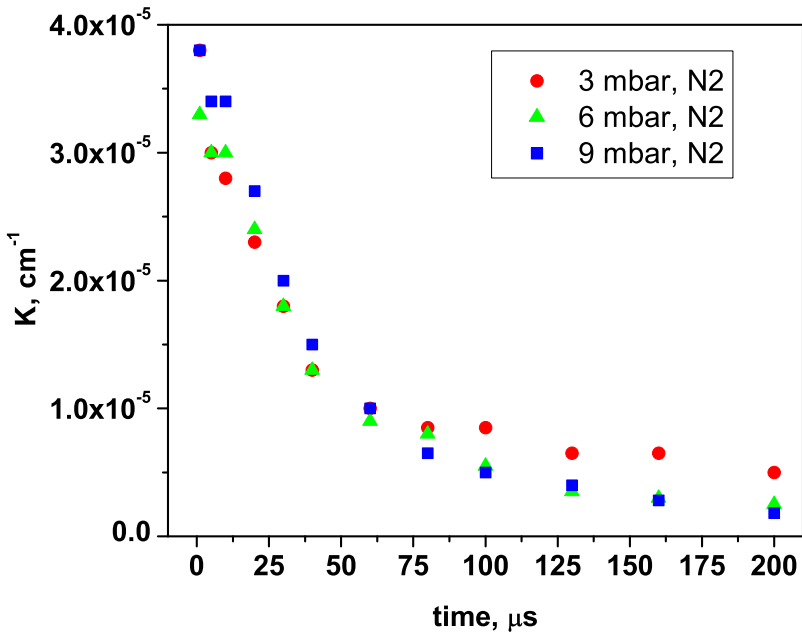
Figure 4.9: Absorption coefficient for $N_2(A^3\Sigma_u^+, v=2)$ in nitrogen
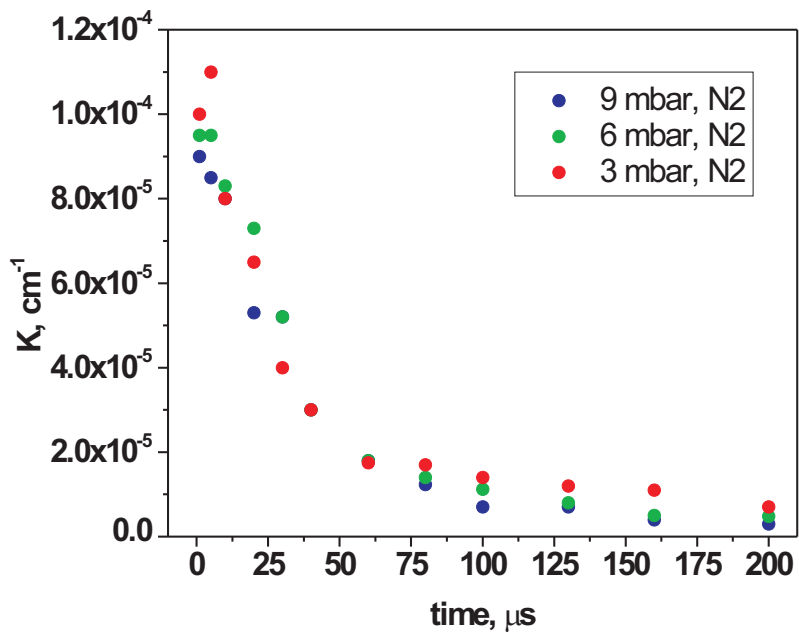
Figure 4.10: Absorption coefficient for $N_2(A^3\Sigma_u^+, v=3)$ in nitrogen

"Fit spectrum" option allows automatic fitting of the bands to determine the various temperatures and densities.

Another function allows the user to import the actual instrumental function of the experimental apparatus. The previous version of the code was limited to trapezoidal slit functions, which may give inaccuracies in the fits.

Finally, the densities of all electronic states are provided for each fit in the body of the software, at the bottom of the screen. Using this data, we can relate the absorption coefficient k of $N_2(A^3\Sigma_u^+)$ transitions to the absolute densities of the corresponding absorbing levels (see next section).

4.5 Quantitative analysis of the (2,0) vibrational transition

Using SpecAir3.0, we have modeled the absorption spectrum of $N_2(B^3\Pi \leftarrow A^3\Sigma_u^+)$ (2,0) transition. In comparison with (3,1) and others, this transition is practically not encroached by rotational lines coming from other vibrational transitions. In this case, the simulated spectrum (normalized) weakly depends on the vibrational temperature. The analysis procedure then consists in searching for the best fit for the rotational lines, and then to refine the fit by adjusting the vibrational temperature.

Simulations were run in the wavelength region of $\lambda = 769.5 - 770.1$ nm. The instrumental function (mostly due to laser broadening) was chosen as trapezoidal with a base of 20 pm and a top 4 pm. At this point, it is not necessary to resort to a more accurate instrumental broadening function because the experimental spectra have only to 3 to 4 points per rotational line.

First, the dependence of the spectrum on vibrational temperature was investigated (see Figure 4.12) The relative intensities of lines remain practically the same for different vibrational temperatures and are solely a function of the rotational temperature. Still, a
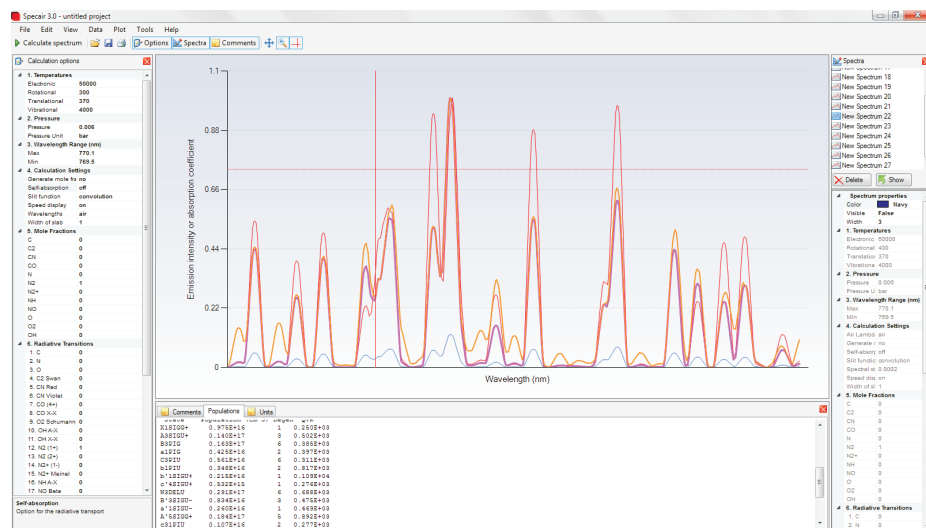
Figure 4.11: SpecAir 3.0. typical window

few lines (indicated by red arrows on the graph), such as the line at 769.68 nm, are seen to depend strongly (several times) on the vibrational temperature, probably because they belong to another vibrational transition. Still, these few lines are present in experimental
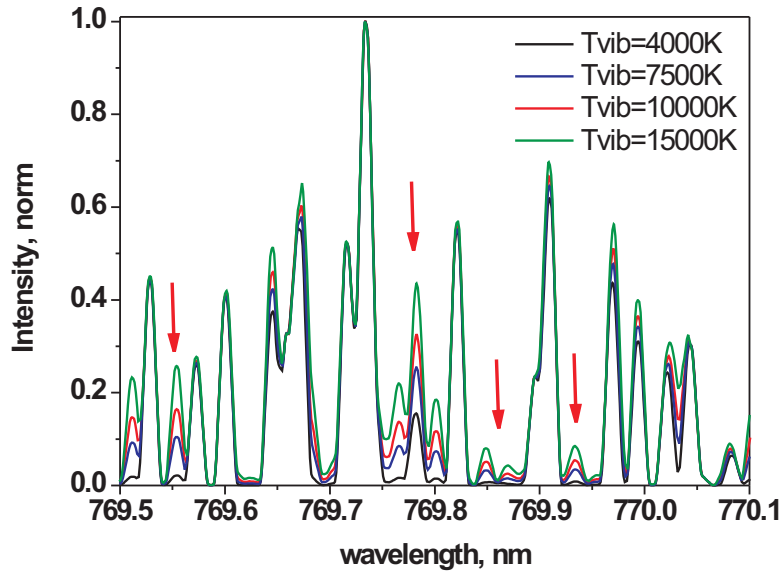
Figure 4.12: Dependence of line's relative intensities on vibrational temperature
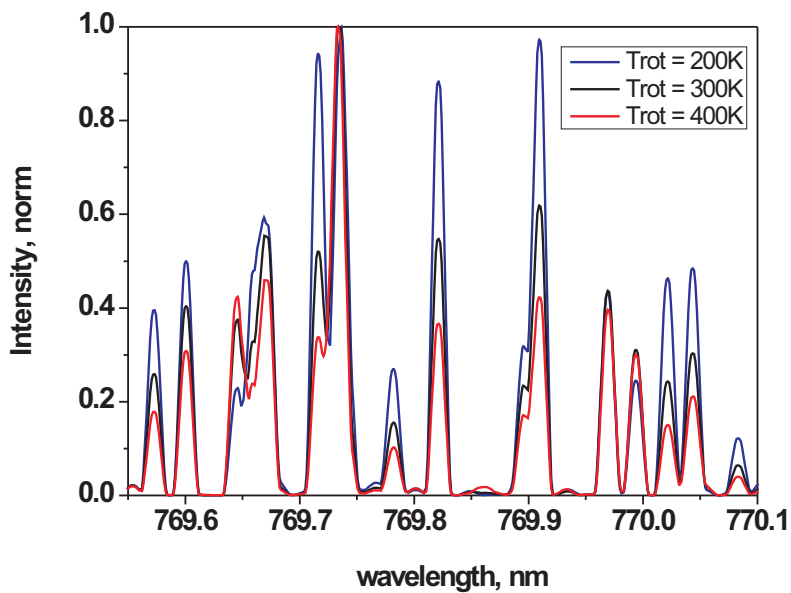
Figure 4.13: SpecAir simulation for different rotational temperatures (200 K, 300 K, 400 K), and a fixed vibrational temperature of 4000 K

53

spectrum (see Figure 4.14), that's why we choose and set temperature T_{vib} equals to 10000 K.

Then we start to vary the rotational temperature, try to find best fit with experimental spectrum. Figure 4.13 shows the dependence of the line intensities in this spectral region on the rotational temperature, which is very strong. The best fit was found with T_{rot} equals to 300 K (Figure 4.14). A reasonable coincidence is observed. The difference between experimental and simulated spectra is, probably, primarily due to poor resolution of spectrum - as we mentioned, 3 points per line is not enough for modeling of laser pulse shape and cannot provide high accuracy for the absolute value of the peak. For example, the difference between modeling and experiment for the line at 769.92 nm can easily be attributed to inaccurate convolution. Another reason is that in the experiments we have non–Boltzman distribution of species, especially for vibrational levels, which cannot be taken into account in SpecAir.

So, rotational temperature $T_{rot} = 300$ K was chosen to obtain the absolute concentration of $N_2(A^3\Sigma_u^+)$ $\nu"$=0 species. This value is reasonable, because at our conditions (pressure is 3 to 9 mbar) the time between collisions is approximately 100 ns, so after 2 μs (when the spectrum measurements were taken) RT-relaxation should equalize translational and rotational temperatures. And translational temperature, as it was shown by emission measurements, lies within the range of 300-380 K.

The next step is to obtain the absolute value of the absorption coefficient $k(\nu)$ by adjusting the electronic temperature T_{el} in SpecAir. Figure 4.14 shows the best fit of the absolute absorption coefficient $k(\nu)$. This coefficient is proportional to the density of $N_2(A^3\Sigma_u^+)$ in vibrational level $\nu"$, according to:
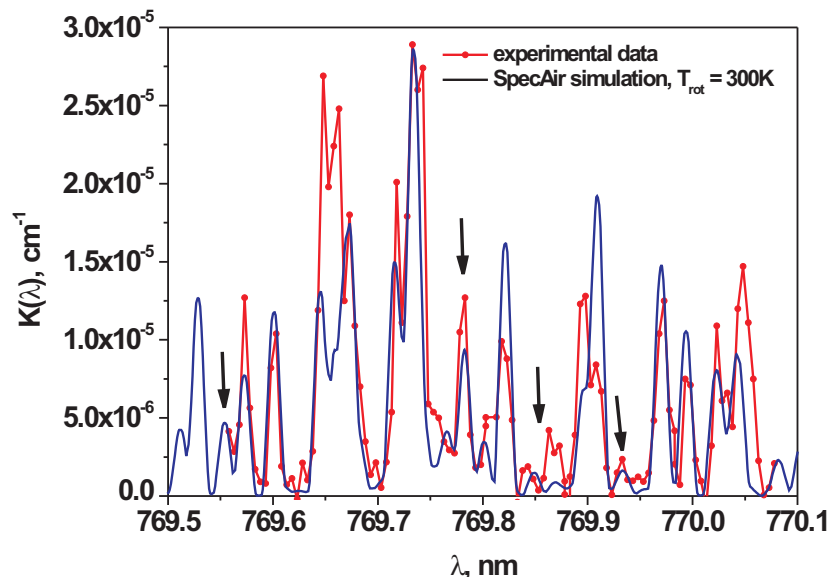
Figure 4.14: Fitting of experimental spectrum with the SpecAir simulation, $T_{rot} = 300$K, $T_{vib} = 10000$ K

Table 4.2: Vibrational term energy $G(\nu)$ for vibrational levels $0 - 15$ and relative populations $n(\nu)$ for different vibrational temperatures.

ν	$G(nu)$, cm^{-1}	$n(\nu)$, %, $T = 10^3$ K	$n(\nu)$, %, $T = 10^4$ K
0	726.98	87.22	18.39
1	2160.02	11.08	14.96
2	3565.25	1.46	12.22
3	4942.68	0.20	10.02
4	6292.28	0.03	8.25
5	7613.93	$4.3 \cdot 10^{-3}$	6.82
6	8907.48	$6.68 \cdot 10^{-4}$	5.66
7	10172.71	$1.08 \cdot 10^{4}$	4.72
8	11409.32	$1.82 \cdot 10^{-5}$	3.95
9	12616.97	$3.20 \cdot 10^{-6}$	3.32
10	13795.25	$5.86 \cdot 10^{-7}$	2.80
11	14943.69	$1.12 \cdot 10^{-7}$	2.37
12	16061.76	$2.24 \cdot 10^{-8}$	2.02
13	17148.87	$4.68 \cdot 10^{-9}$	1.73
14	18204.35	$1.02 \cdot 10^{-9}$	1.48
15	19227.50	$2.35 \cdot 10^{-10}$	1.28

$$k(\nu) = S(T) \cdot \phi\nu \cdot N, \tag{4.7}$$

where $S(T)$ is the line strength of a specific absorption line at temperature T, ϕ is the normalized absorption coefficient profile function, and N is the density of level ν". Thus, with this procedure, absolute densities for $N_2(A^3\Sigma_u^+)$, ν" can be obtained.

SpecAir provides as an output the total density of $N_2(A^3\Sigma_u^+)$, i.e. with all vibrational levels populated according to a Boltzmann population distribution at the fitting temperature T_{vib}. The density of $N_2(A^3\Sigma_u^+)$ ν"=0 then corresponds to the Boltzmann fraction in nu"=0, which can be determined from the following equation:

$$N_2(A^3\Sigma_u^+)(\nu'' = 0) = N_2(A^3\Sigma_u^+)_{\text{total}} \cdot \frac{\exp(-\frac{\text{hc}G(\nu''=0)}{\text{kT}_{\text{vib}}})}{\sum_{\nu''} \exp(\frac{\text{hc}G(\nu'')}{\text{kT}_{\text{vib}}})} \tag{4.8}$$

where $G(\nu'')$ stands for the vibrational term energy which is obtained using the Klein-Dunham expression:

$$G(\nu'') = \omega_e(\nu + \frac{1}{2}) - \omega_e\xi_e(\nu + \frac{1}{2})^2 + \omega_e y_e(\nu + \frac{1}{2})^3 - \omega_e z_e(\nu + \frac{1}{2})^4 \tag{4.9}$$

Table 4.2 gives the values of the vibrational term energy $G(\nu'')$ for different vibrational levels and their relative populations $n(\nu'')$ at 1000 K and 10000 K. For a vibrational temperature equal to 10000 K, the number density of particles in the zeroth vibrational level is 18% of the total $N_2(A^3\Sigma_u^+)$ density.

The final results for the decay rate are presented in Figures 4.15 and 4.16. The peak value of $N_2(A^3\Sigma_u^+)$, ν"=0 just after the discharge is approximately the same for air and
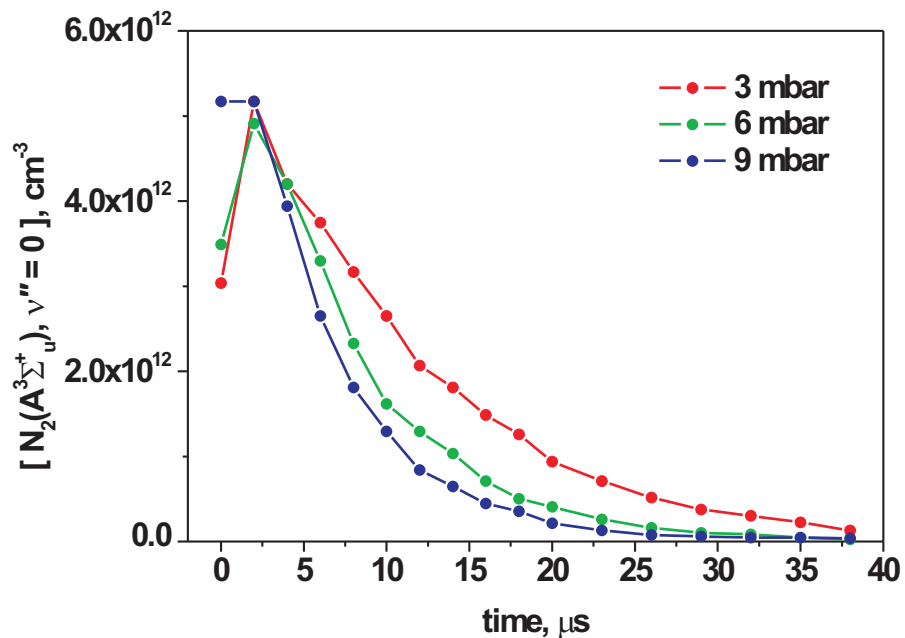
Figure 4.15: Absolute values of $N_2(A^3\Sigma_u^+, v=0)$ density in synthetic air
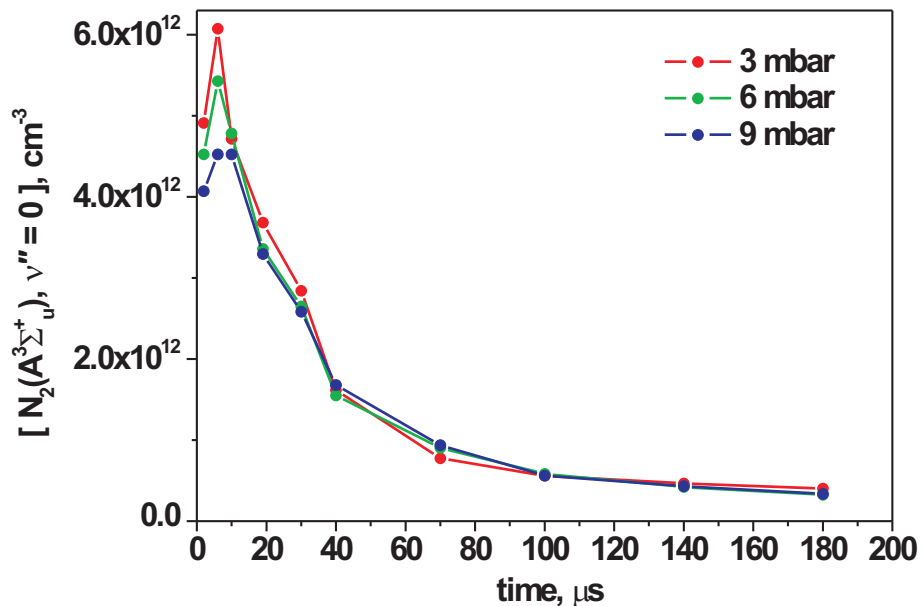
Figure 4.16: Absolute values of $N_2(A^3\Sigma_u^+, v=0)$ densities in nitrogen

nitrogen and corresponds to $(5-6) \cdot 10^{12}$ cm^{-3}.

4.6 Conclusions

The experimental setup and diagnostic system were suggested, constructed and adjusted for cavity ring–down measurements of metastable stages of nitrogen in the afterglow of a nanosecond discharge.

Absorption coefficients have been obtained for 4 vibrational transitions as a function of time (within a range of $0 - 200$ μs) and pressure ($3 - 6$ mbar) for synthetic air and pure nitrogen. The experiments demonstrate that $N_2(A^3\Sigma_u^+, v = 0)$ density decay in air is much faster than in nitrogen because of quenching by oxygen.

Using the latest version of the SpecAir code, a fit of the experimental absorption spectrum of the (2,0) transition was obtained. The simulation yields a rotational temperature close to room temperature. Based on this simulation, the absolute density of the $N_2(A^3\Sigma_u^+)$ ($\nu"=0$) vibrational level was inferred. The density of $N_2(A^3\Sigma_u^+)$ ($\nu"=0$) just after the discharge (2 μs) is approximately equal to $(5-6) \cdot 10^{12}$ cm^{-3}, both for synthetic air and nitrogen.

Chapter 5

Time–resolved electric field measurements in 1–5 atm nanosecond surface dielectric discharge. Ignition of combustible mixtures by surface discharge.

5.1   Introduction

During the last decades, a special attention to ignition and combustion initiation by nonequilibrium low–temperature plasma is observed [47]. The experiments and calculations are carried out for different initial gas parameters, for gas pressures from units of Torr [3] to atmospheric pressure [48] or higher, and for gas temperatures from ambient temperature [49] to the temperatures near the ignition threshold [50]. Different mechanisms concerning ignition by nonequilibrium plasma are widely discussed [51].

A few evidences of high–pressure ignition by nanosecond discharges are given in the literature [48, 49, 52, 53] are presented in the literature.

Paper [48] presents the results of an experimental study of the efficiency of the ignition of propane-air mixtures by a high voltage repetitively pulsed nanosecond gas discharge (10 kV, 10 ns, 30 kHz) for the pressure range $0.35 - 2.0$ bar. The discharge is localized between a two metal electrodes in a point–to–plane geometry with a 1.5 mm interelectrode distance. The measured minimal energy for ignition was found to decrease with the pressure. A significant reduction of the ignition delay and a decrease of the overall combustion duration were obtained by using a burst of high–voltage pulses. In this paper, authors demonstrate a high efficiency of a nanosecond spark mode, when a breakdown occurs between two electrodes of the discharge system, and relatively low efficiency of the first, "streamer" stage, when no high current between two electrodes is observed.

In a recent study [49] a nanosecond discharge (a few tens of ns, rise time 2–3 ns, 40-60 kV) was generated in a 16 mm gap, between a point of 100 μm radius and a grounded plane. In pure dry air, the discharge demonstrated a diffuse regime which became more and more filamentary when propane was added. In the filamentary regime, the ignition of propane-air mixtures and the propagation of a self-sustained flame was

obtained with a single nanosecond pulse. The preliminary LIF OH measurements in discharge at $P = 1$ atm in synthetic air with 0.5 % of propane addition are presented. OH–mapping demonstrates a presence of significant amount of OH radicals on the axis of the discharge gap 6.5 μs after the discharge.

High–frequency high–voltage discharge is used in [52] to ignite H_2:air mixtures containing from 10 to 50 % of hydrogen. The streamer low–current (units of mA) discharges are produced within a rod/plane electrode configuration with a gap of 40 mm inside an optical accessible ignition cell. The sinusoidal alternating voltage with a peak voltage of up to 20 kV is generated by a resonating air–cored coil in combination with a frequency generator and a power amplifier. The number of voltage cycles and the voltage amplitude can be defined using the frequency generator. Depending on the resonance frequency of the coil, the voltage alternates with a frequency between 600 and 750 kHz. The authors report 2D maps of OH density taken by LIF technique. They compare the results to numerical simulations of ignition by a local equilibrium source of heat and come to the conclusion that the flame velocity in the radial direction (perpendicular to a streamer channel) does not practically depend upon a source of heat, while the ignition volume and energy are strongly influenced by a streamer geometry.

Paper [53] presents a multi–point ignition initiated by 12 ns and 50 kV pulses in 1 atm C_2H_2:air mixture at the equivalence ratio 1.1. The ignition is realized in open–electrode coaxial system by a single nanosecond pulse. Measurements of a rotational temperature by measuring and fitting the emission of molecular nitrogen in the afterglow of the discharge (about 100 ns later) show that gas remains cold (300 ± 60 K). The authors compare two flame images obtained for the ignition by a commercial spark (105 mJ, 10 μs, 15 kV) and nanosecond discharge (70 mJ, 12 μs, 54 kV) ignition. At time instant $t = 6$ ms after the ignition, a flame diameter is equal to 74 mm for spark ignition and 93 mm for nanosecond discharge ignition. A multi–point character of the ignition is clearly seen.

The aim of the present paper is to study a nanosecond discharge ignition in a multi–point configuration caused by a set of streamers originating in a surface DBD geometry and, on the basis of data obtained electric field measurements, to analyze possible mechanisms of initiation of combustion in such a system.

5.1.1 Experimental setup

The scheme of the experimental setup is given by figure 5.1. The discharge cell was made of stainless steel and had 4 optical windows (quartz or glass 1 cm in thickness and 5 cm in diameter). For the combustion experiments, one of the windows was replaced with a dump volume separated from the discharge chamber by a 12–μm diaphragm made of metallized dacron film. The electrode system was connected to the high–voltage generator via 25 m coaxial 50 Ohm cable. Calibrated back current shunt was installed between the high–voltage generator and the discharge cell to measure the amplitude and the shape of a high–voltage pulse. The shunt was composed of low inductive resistances, soldered into the break of the cable shield, and it was connected to the LeCroy WaveRunner 400 MHz oscilloscope.

The discharge chamber could be either pumped up to the pressure of $6 \cdot 10^{-2}$ Torr or filled in with synthetic air up to the pressure of 10 atm. The chamber was connected to rotational pump and to the cylinder with synthetic air or combustible gas mixture. In

each experiment the chamber was evacuated and then filled up to the pressure of interest. Low pressures (less than 10 Torr) were measured by Pfeiffer capacitive vacuum gauge, high pressures (more than 1 bar) were measured by SCM capacitive manometer. Synthetic air (80% N_2, 20% O_2 Air Liquide, impurities did not exceed 3 ppm) or C_2H_6:O_2=2:7 mixture were used for the experiments.
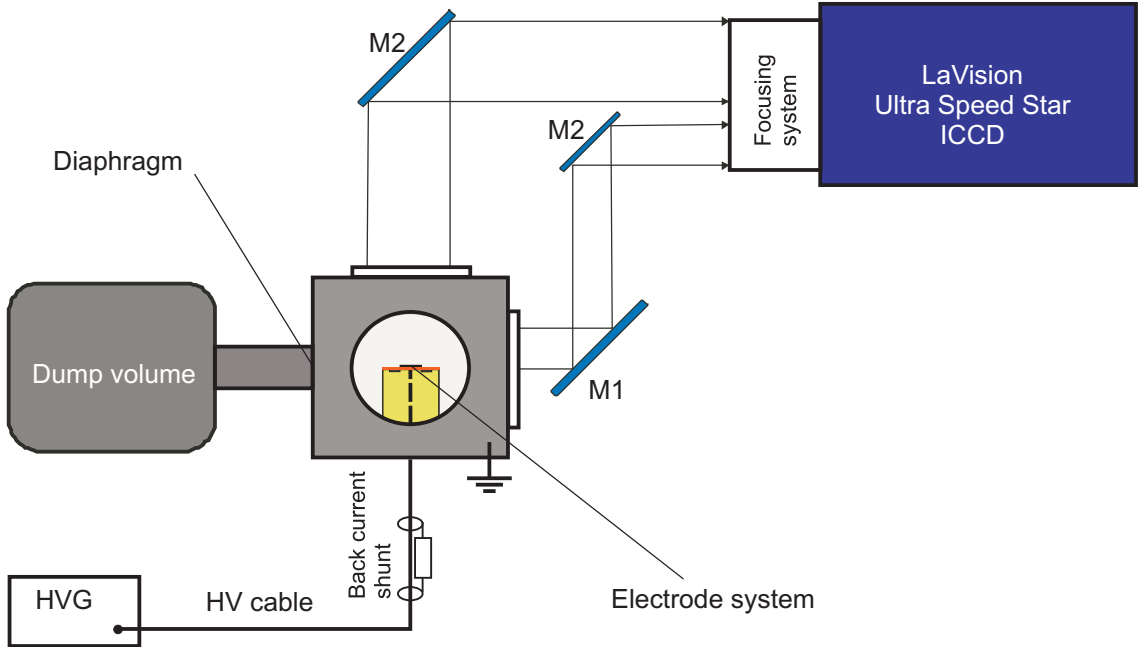
Figure 5.1: Scheme of the experimental setup, the configuration used for the combustion experiments. HVG is a high voltage generator.

Two electrode systems represented schematically by figure 5.2 were used in the experiments. In the coaxial electrode system of the surface dielectric barrier discharge (see figure 5.2(a)), a high voltage pulse was applied to the central coaxial electrode which is connected to a disk electrode made of brass. For the measurements of the reduced electric field, the disk was replaced by an aluminum foil 50 μm in thickness and 20 mm in diameter. The discharge was initiated from the edge of the high–voltage electrode.

The aluminium foil electrode covered the 0.4 mm polyvinylchloride (PVC) dielectric layer under which the ground electrode was located. The ground electrode was made from aluminium, its inner diameter equals to the outer diameter of the high–voltage foil electrode, and its outer diameter was equal to 46 mm. Dielectric film (0.4 mm polyvinylchloride (PVC) layer) covered the low voltage electrode.

In spark configuration used for the combustion experiments, the electrodes were two metal rods 6 mm in diameter (see figure 5.2(b)). One of the rods served as a high–voltage electrode and another was grounded. Two screws of 3 mm in diameter with pin tips pointed to each other were driven in high–voltage and grounded rods. The discharge gap between the pin tips was 2 mm.

Typical shape of the high voltage pulse on the high-voltage electrode in the absence of discharge is shown in figure 5.3. For the ICCD visualisation of the discharge, both positive and negative polarity pulses were used. Electric field measurement was made for a positive polarity pulse, and initial stage of combustion was studied for the negative
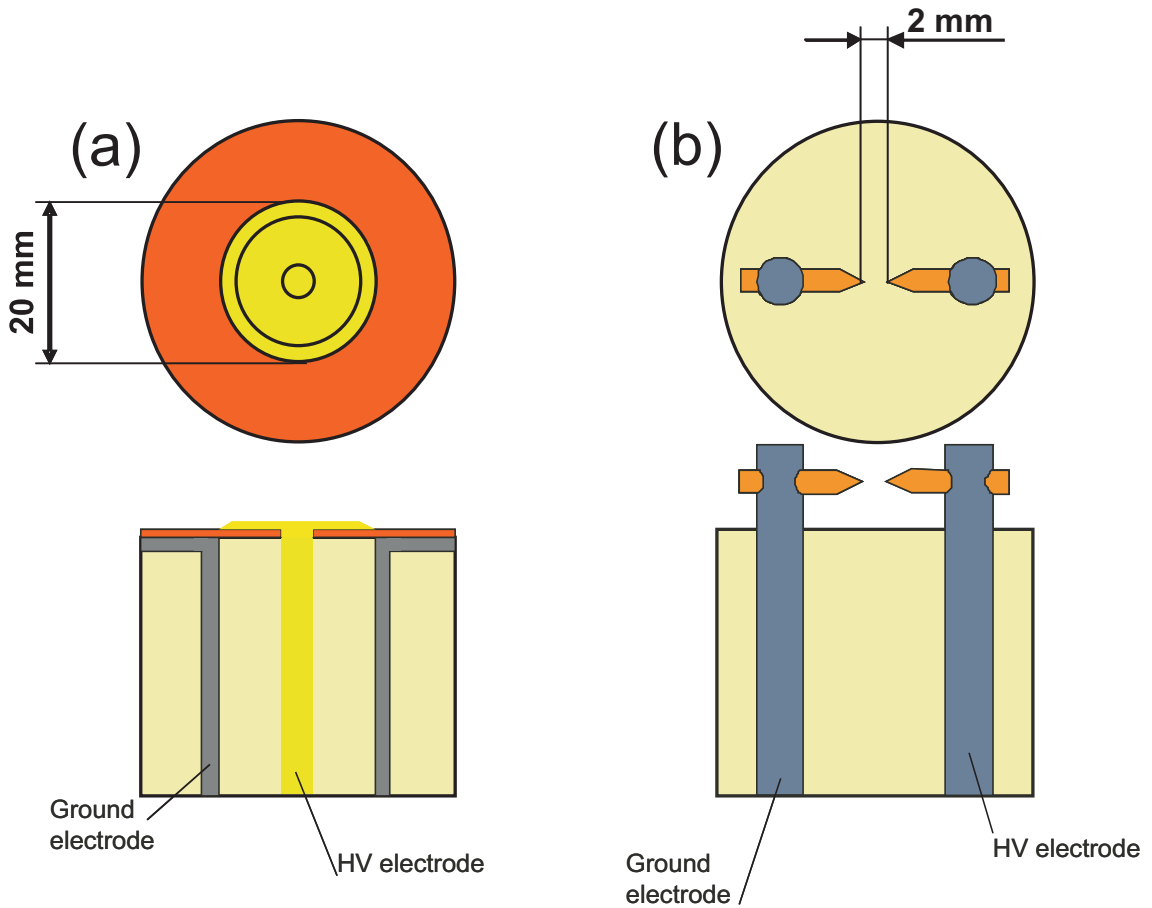
Figure 5.2: Scheme of the electrode systems used in the experiments. (a) the electrode configuration for a surface nanosecond dielectric barrier discharge, (b) the electrode configuration for a nanosecond spark discharge.

polarity of high voltage pulse.

5.1.2   ICCD imaging

To study the spatial structure and the development of the surface discharge, 2D map of emission integrated over the wavelength range 300–800 nm was measured with a PicoStar HR12 (La Vision) ICCD camera. The discharge image was focused onto a photocathode of a camera with a system of UV lenses. Camera gate was equal to 0.5 ns. Both for high-current open electrode nanosecond discharges [16, 54] and for dielectric barrier discharges [55], the main emission in this spectral range is due to transitions of the second positive system of molecular nitrogen. For air, the quenching time is determined by collision of excited nitrogen molecules with molecular oxygen, the rate constant is equal to $k = 2.7 \cdot 10^{-10}$ cm^3/s [56]. So, the efficient life time of $N_2(C^3\Pi_u)$ is 0.7 ns for 1 atm and 0.14 ns for 5 atm. For typical velocities of propagation less than a few cm per nanosecond, this means that ICCD imaging reflects adequately the spatial structure of the discharge. The CCD camera and the intensifier were synchronized with the high–voltage generator. The position of a camera gate was checked with a coaxial photocell with response time 0.2 ns.
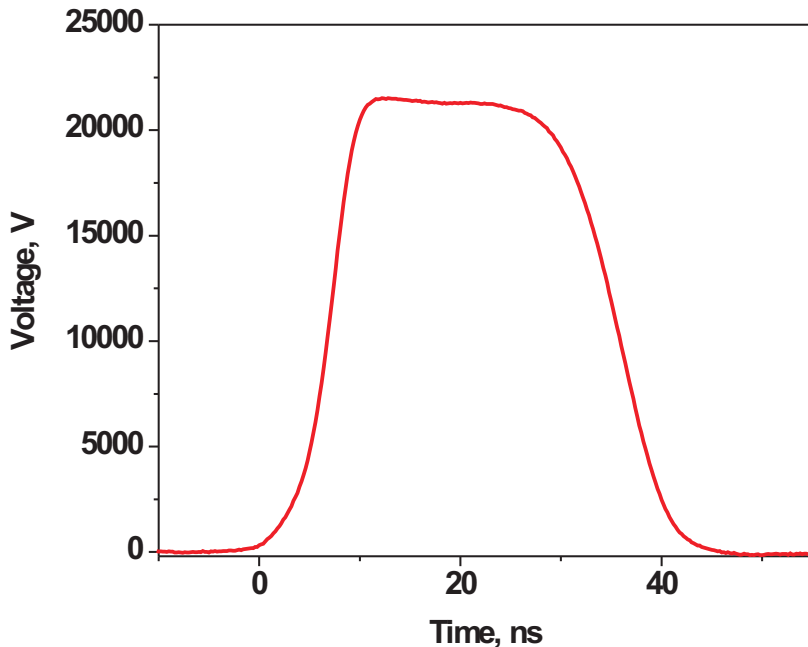
Figure 5.3: Typical high voltage pulse, a signal from the back current shunt.

5.1.3 Measurements of ratio of the emission bands

Two molecular bands with significantly different cross-sections and thresholds of excitation by an electron impact, namely 0–0 vibrational transitions of the second positive (337.1 nm) system of molecular nitrogen and of the first negative (391.4 nm) system of molecular nitrogen ion were used for the analysis of the electric field behaviour. The details of the procedure can be found elsewhere [57, 58, 55] and will be discussed later.

The emission was focused to the entrance slit of monochromator by UV lens. Nanosecond photomultiplier tube (PMT) RTC XP2020 was installed on the output slit of the monochromator. In the experiments the TRIAX 320 scanning monochromator was used (2400 m^{-1} grating, 1.3 nm/mm dispersion). PMT signal was registered by Le Croy WaveRunner 400 MHz oscilloscope with input impedance of 50 Ohm. Time resolution of the system was about 2 ns. Broad–band glass filter was used to reduce emission intensity in UV spectrum range (at the wavelength of 337.1 nm) to perform the measurements of both molecular bands at similar PMT voltages.

For relative intensity calibration of the optical system at 337.1 nm and 391.4 nm an ORIEL 3000 deuterium lamp with a 30 W power was used. A wide range of PMT power voltage (600 − 1000 V) was used to check the signal linearity and to reduce a possible error in the calibration coefficient.

The ring plastic diaphragm was installed 3 mm above the dielectric layer coaxially to the electrode system. It allowed us registration of emission only from a narrow area of the dielectric surface, i.e. to obtain field measurements along the radius of electrode system. Four ring diaphragms were used in the experiments. The diafragms selected the rings 20 ± 1, 26 ± 1, 32 ± 1 or 38 ± 1 mm in diameter; so the width of the optical region

62
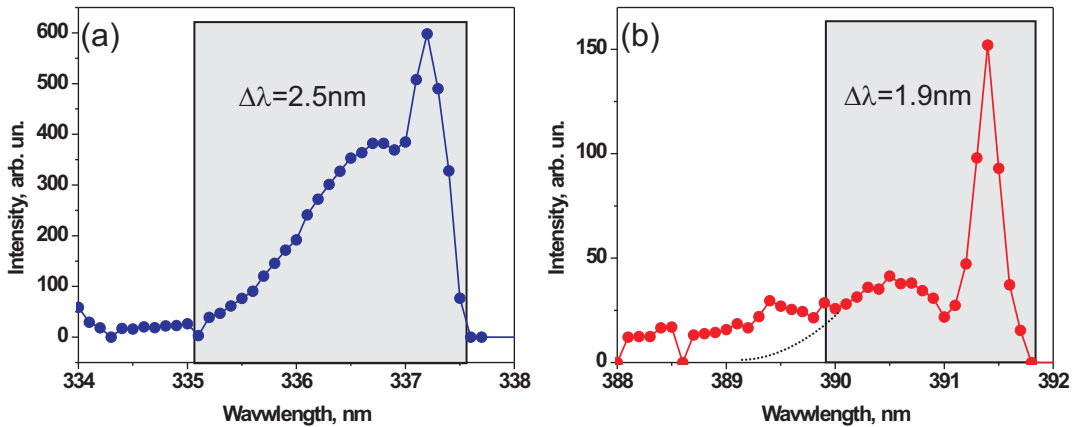
Figure 5.4: Emission spectra of 0-0 transitions of the second positive (left) system of molecular nitrogen and first negative (right) system of molecular nitrogen ion. Grey squares give the spectral region registered in the experiments.

selected by each diaphragm was equal to 2 mm.

The entrance slit of the monochromator was set up to the value of 2.5 mm for registration of N_2 second positive system emission and 1.9 mm for registering of N_2 first negative system emission. For the second positive system, all the rotational structure was registered, as it is indicated in figure 5.4, and for the first negative system of molecular nitrogen ion the data at low wavelengths were cut to avoid the overlapping with the spectrum of 3–6 vibrational transition of the second positive system of molecular nitrogen ($\lambda = 389.5$ nm). The last fact caused the error not more than 5–10% in determination of the total intensity of emission of the first negative system of molecular ion.

5.1.4 Connection between ratio of the emission bands and electric field

To relate a ratio of the emission bands to the electric field, a detailed analysis of papers [57, 59, 60, 58] have been made.

Paper [57] presents measurements of intensity ratios of first negative and second positive systems of molecular nitrogen in non–self–sustaining DC discharge in a parallel–plane gap. Emission intensities of two transitions of the second positive system ($N_2(C^3\Pi_u$, v=0) $\rightarrow N_2(B^3\Pi_g$, v=0), $\lambda = 337.1$ nm, $N_2(C^3\Pi_u$, v=2) $\rightarrow N_2(B^3\Pi_g$, v=5), $\lambda = 394.3$ nm) and a transition of the first negative system ($N_2^+(B^2\Sigma_g^+$, v=0)$\rightarrow N_2^+(X^2\Sigma_g^+$, v=0), $\lambda = 391.4$ nm) are measured for reduced electric field range $150 - 5000$ Td. The paper presents also the results of calculations of other authors [61, 62, 63]. The observed difference between the calculations and experimental results is significant, up to an order of magnitude at low E/N values. The authors of [57] do not discuss the details of numerical calculations. In later paper [58] they analyze the collisional quenching rates of molecular nitrogen ion $N_2^+(B^2\Sigma_g^+, v = 0)$, available in the literature, and demonstrate that using the quenching rates given by [56] it is possible to obtain a very good agreement between the experimental data obtained in [57] and numerical modeling.
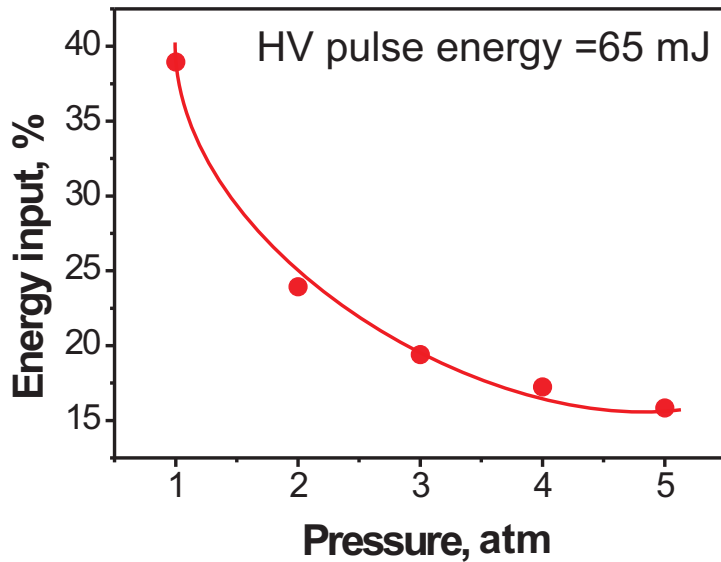
Figure 5.5: Typical high voltage pulse, a signal from the back current shunt.

Paper [59] discuss possible influence of the three–body conversion process $N_2^+(B^2\Sigma_u^+)+N_2+M\rightarrow N_4^+$ on the data on emission ratio for two considered molecular bands, pointing out that at high pressures this process may lead to a significant decrease of $N_2(B^2\Sigma_u^+)$ emission and, consequently, the experimental data can be misinterpreted without taking this into account. Details of the experimental data on emission bands ratio *vs* pressure given in [60] prove that there is no influence of a three–body reaction of conversion at the conditions of experiments published in [57], the measured ratios of two spectral bands at fixed E/N do not depend upon pressure within the pressure range $10-100$ kPa. Possible reasons for the negligible role of a three-body reaction are discussed, namely (i) the fact that the rate constant of the reaction has been measured at low pressures and can decrease with a gas pressure; (ii) the fact that the rate constant can decrease with the value of reduced electric field, (iii) the fact that the discussed reaction rates were determined for the ground state of N_2 molecular ion, not for electronically excited state. In [58] the authors consider also the three–body reaction of quenching of $N_2^+(B^2\Sigma_u^+)$ by molecular oxygen and show that, for experimental conditions of [57], the influence of the three–body quenching is within the limits of uncertainties of measurements.

So, for treatment of our experimental data, for each time moment, a ratio of emission signals, $I_{391.4}/I_{337.1}$ was determined. The only process of excitation considered was an excitation by a direct electron impact, what is typical for the nanosecond discharges [15, 16, 20]. We assumed that quenching processes were two–body quenching reactions with N_2 and O_2 for both considered electronic states. Under these conditions, the ratio $I_{391.4}/I_{337.1}$ is connected to reduced electric field by an expression from [57]:

$$R_{391/337}\left(\frac{E}{N}\right) = 46\exp\left[-89\left(\frac{E}{N}\right)^{-0.5}\right] \cdot 0.065\exp\left[-402\left(\frac{E}{N}\right)^{-1.5}\right]. \qquad (5.1)$$

64

5.1.5 Measurements of combustion initiation

To perform optical measurements and observations of combustion experiments, three optical windows of the discharge chamber were used. Two windows were on the opposite sidewalls and one was on the top side of the chamber above the electrode assembly. A system of three mirrors was mounted in order to perform instant imaging of flame propagation from top view and side view (see figure 5.1 for details). LaVision Ultra Speed Star ICCD was used for high–speed photography. The camera allowed to take 16 photos with a minimal exposure time of 0.5 μs and a minimal time of 1 μs between frames. The camera triggering was synchronized with a high–voltage pulse. All 16 exposures and frames were adjusted manually.

5.2 Results and discussion

5.2.1 Deposited energy and discharge morphology

The energy input into discharge, calculated for the positive high voltage pulse on the basis of a difference between incident and reflected current pulses, is given by figure 5.5. It is clearly seen that the energy input at 5 atm is more than two times lower than at 1 atm at the same amplitude of the high-voltage pulse. It should be noted that at fixed gas pressure $P = 1$ atm the increase of high voltage amplitude from 6 to 11 kV in the cable (12 to 22 kV on the high–voltage electrode) leads to increase in deposited energy from 5 to 22 mJ. Subsequent reflections of the pulse from high–voltage generator and from the discharge cell (1–2 reflections where the energy input is still significant) can add not more than 50 % of energy deposited in the first pulse.

The ICCD images of the discharge have been taken for both positive and negative polarities for 1, 3 and 5 atm, 22 kV pulse amplitude on the electrode. The examples of the discharge morphology are given by figures 5.6 and 5.7. For all the pressures studied, a simultaneous (within a gate of 0.2 ns) start of streamers from the high–voltage electrode is observed. This is similar to observations of a nanosecond discharge at atmospheric pressure in ambient air [64, 65] for a linear electrode geometry (so–called "plasma actuator" configuration). Pictures of the discharge development for different polarities are rather similar. If for the sinusoidal 50 Hz voltage the surface dielectric barrier discharge is bright and filamentary during a positive half–period of the applied voltage, and weak and more diffuse during a negative half–period [55, 66], the observed difference between the polarities for the nanosecond discharge is rather qualitative then quantitative. The most distinctive differences between nanosecond surface dielectric barrier discharges at positive and negative polarities are the following: (i) higher brightness of the images for negative polarity; (ii) more uniform emission "along" the streamers, that is no so well–defined "head" or "channel" observed at positive polarity; (iii) more "fine" structure in the direction perpendicular to the streamers propagation, that is more streamers per unit length of the circumference observed for a positive polarity.

Let us consider ICCD images at $P = 1$ atm in detail. For the negative polarity of the high–voltage electrode, the discharge starts within a few first nanoseconds as a "synchronous" propagation of streamers in radial direction; the intensity of the emission along each streamer is practically constant (see f.e. figure 5.6 a, time instant equal to
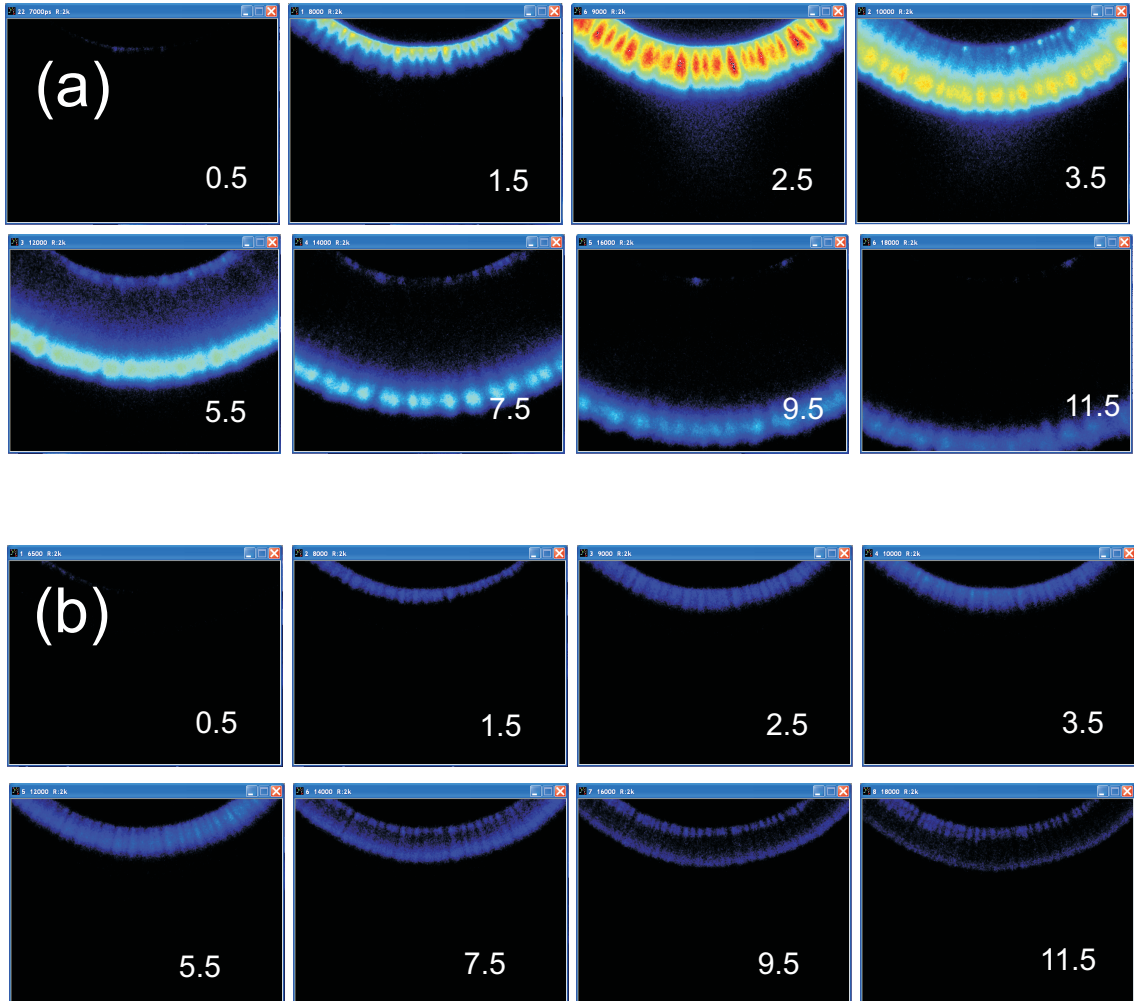
Figure 5.6: ICCD images of the surface discharge development. A sector about 90° is shown, the high–voltage electrode is at the top of the image. $P = 1$ atm, $|U|$=22 kV on the electrode.(a) negative polarity of the high–voltage pulse; (b) positive polarity.

2.5 ns). With the development of streamers, their "channels" become less bright compared to the "heads" (figure 5.6 a, time instant 5.5 ns), and then the emission from the "heads" of the streamers is only observed (11.5 ns). During this phase, the velocity of the discharge propagation remains practically constant, about 1.2 mm/ns. It should be noted that we did not follow the trailing edge of the pulse in these experiments. For positive polarity, the picture is similar, but the velocity of the propagation of the streamers in radial direction is a few times slower, the intensity of emission is lower, and the stage of uniform emission along the streamer is longer and more pronounced (figure 5.6 b). Finally, two equally bright zones are observed, one on the edge of the electrode and another one corresponding to the "heads" of the streamers.

With pressure increase at fixed pulse amplitude, the main features of the discharge development remain the same. Streamers start simultaneously from the high–voltage electrode and propagate along the dielectric surface over the hidden grounded electrode strictly in radial direction. The emission intensity distribution between streamers remains uniform. The only observed regime where some streamers become brighter than the others
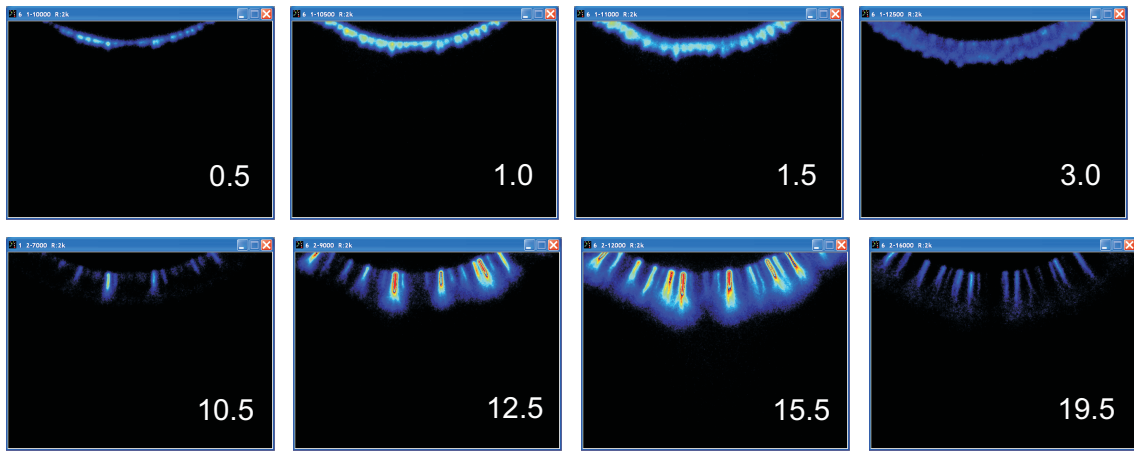
Figure 5.7: ICCD images of the surface discharge development. A sector about 90° is shown, the high–voltage electrode is at the top of the image. $P = 5$ atm, negative polarity, $U = -22$ kV on the electrode.

corresponds to positive polarity discharge at $P = 5$ atm and time instants $t > 10$ ns (see figure 5.7).

5.2.2 Electric field

The emission behavior with time in the surface DBD discharge is rather complicated. The example of time–resolved synchronized emission of two different transitions, $N_2(C^3\Pi_u,$ v=0) $\rightarrow N_2$ $(B^3\Pi_g,$ v=0), $\lambda = 337.1$ nm, and $N_2^+(B^2\Sigma_g^+,$ v=0)$\rightarrow N_2^+(X^2\Sigma_g^+,$ v=0), $\lambda = 391.4$ nm is given by figure 5.8 for the edge of the high–voltage electrode (figure 5.8 a) and 3 mm apart (figure 5.8 b). The emission signals are normalized so that for both transitions the amplitude of the first peak corresponding to the leading edge of the high–voltage pulse is equal to unity.

If to analyze the emission and the electric field, it is clearly seen that the emission of nitrogen molecule ($\lambda = 337.1$ nm) is observed on the trailing edge of the high–voltage pulse near the electrode (figure 5.8 a) while no emission is observed 3 mm apart (figure 5.8 b). Emission of molecular nitrogen ion ($\lambda = 391.4$ nm) is very small for both cases. This means that the electric field is maximum on the leading edge, then the second peak, less intensive, is observed on the trailing edge, decaying when discharge propagates in the radial direction.

For the second pulse, reflected from the discharge setup, then from the high–voltage generator, and coming back at approximately 280 ns (in these experiments, we used a cable 27 m in length between the discharge setup and a high–voltage generator), the emission structure is even more complicated. The ratio $R_{391.4/337.1}$ at the leading edge of the second pulse, $t > 270$ ns is evidently less than for the first pulse (0 ns $< t <$ 40 ns), while at the trailing edge emission of molecular ion can be even stronger than the emission of nitrogen molecule (see for example figure 5.8 a).

It should be noted that presented measurements do not allow analysis of the direction of the electric field, while the spatial structure of filaments in the surface DBD discharge is rather 3–dimensional. Here, a comparison with comprehensive numerical modeling would

be useful for detailed analysis of the electric field behavior.

For further analysis, only the first peak of the electric field, corresponding to the leading edge of the first pulse, will be considered.
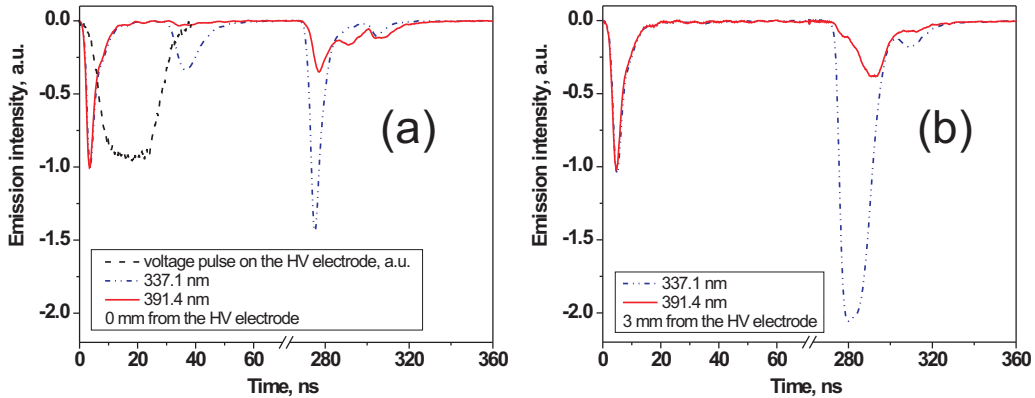
Figure 5.8: Emission oscillograms: (a) edge of the high–voltage electrode; (b) 3 mm apart. Solid red line: $\lambda = 337.1$ nm, dashed blue line: $\lambda = 391.4$ nm, dashed black line: high–voltage pulse on the electrode in arbitrary units. The emission plots are normalized so that for both transitions the amlitudes of the first peak are equal to unity.

Figures 5.9–5.10 represent values of the reduced electric field $(E/N)_{eff}$ taken at the time instant when the emission of molecular nitrogen ion ($\lambda = 391.4$ nm) reaches the maximum value. This corresponds to $t_{eff} = 4 - 6$ ns, depending upon gas pressure. A term "peak reduced electric field" will be used hereinafter to designate $(E/N)_{eff}$ in spite of the fact that peak detected values are somewhat $(20 - 25\ \%)$ higher and correspond to $t = 0$ ns.

Spatial distribution of $(E/N)_{eff}$ is shown in the figure 5.9 for gas pressure $P = 1$ atm. The electric field is minimum on the edge of the high–voltage electrode (about 300 Td), then it increases. It should be noted that the emission intensities are maximal near the electrode and decrease with the distance from the electrode, while the reduced electric field remains constant. The picture is similar for all investigated pressures.

Evolution of peak electric field with pressure is shown in the figure 5.10. The E/N_{eff} value on the edge of the high–voltage electrode remains the same for all the pressures and equal to 350 ± 50 Td. The peak electric field decays significantly, from 570 to 400 Td, when the pressure increases from 1 to 4 atm.

Measurement of time–resolved ratio of intensities of emission at 391.4 and 337.1 nm for the first peak of emission gives the following results: for different distances from the high-voltage electrode, for different pressures and voltage amplitude we observe (i) elevated values (peak) of reduced electric field during first 5 ns of the discharge development; (ii) relatively high values of reduced electric field (hundreds of Td) behind the front, during approximately 20 ns. The examples of reduced electric field behavior with time are given in the figure 5.11.

High electric fields ($E/N > 300$ Td) are observed in the experiments after the discharge front, up to $t \approx 20$ ns, even near the high-voltage electrode. The ionization frequency at
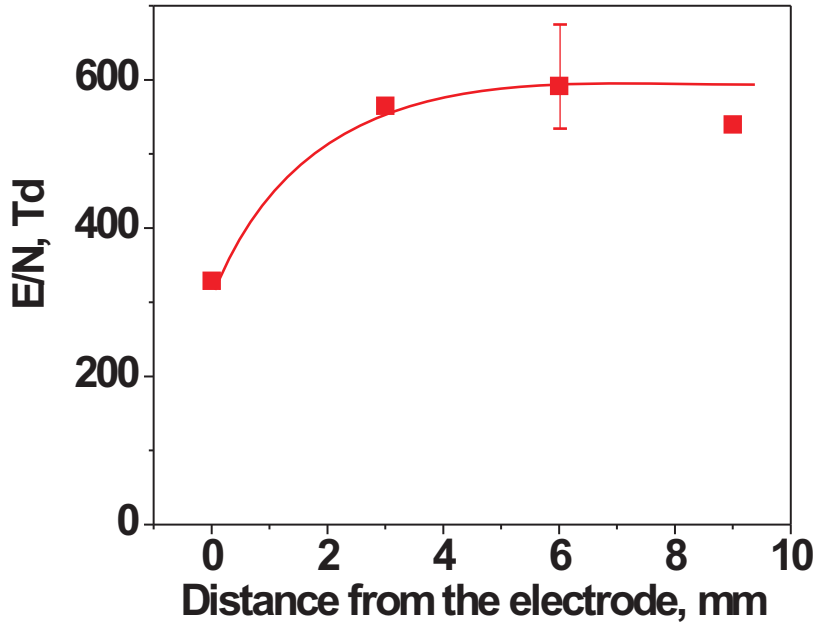
Figure 5.9: Reduced electric field E/N_{eff} *vs* distance from the high–voltage electrode for $P = 1$ atm. Values of E/N_{eff} are taken at the time instant corresponding to peak of emission of molecular nitrogen ion at $\lambda = 391.4$ nm. $U = 22$ kV on the electrode.

$E/N > 300$ Td and $P = 3$ atm is $\nu_{ion} > 6 \cdot 10^{10}$ s^{-1} [68]. At these parameters the electron density and specific deposited energy would reach enormously high values $n_e = 10^{18}$ cm^{-3} and $\eta > 10^3$ eV/mol, respectively, during 20 ns. One of the possible explanations is that so high electric fields are realized in a narrow gap between a plasma channel and dielectric surface. In papers [69, 70] by means of numerical modeling it is found that the width of this gap can be as small as $\delta \approx (1 - 2) \cdot 10^{-3}$ cm. Thus, a Townsend discharge with high E/N values and low electron densities can be observed between a dielectric and a streamer channel. The initial electrons are desorbed from the dielectric surface and drift to the streamer channel, though their density remains small. In an indirect way, this assumption is confirmed by the fact that electric field behind a streamer front caused by a nanosecond voltage pulse in a free space, in the absence of dielectric, is significantly smaller than in the streamer head. Taking parameter δ from [70] and assuming that a density of the electrons desorbed from the surface of dielectric is equal to $n_s = 10^2$ cm^{-3}, for $E/N = 600$ Td and $P = 3$ atm one can obtain $\nu_{ion} \cdot \delta/v_{dr} \approx 15$, and the final density of electrons near the streamer body may reach $3 \cdot 10^8$ cm^{-3} at the condition that the deposited energy there does not exceed 10^{-5} eV/mol. So, the electron density may be enough to give some non–zero input to emission at the conditions of high electric field.
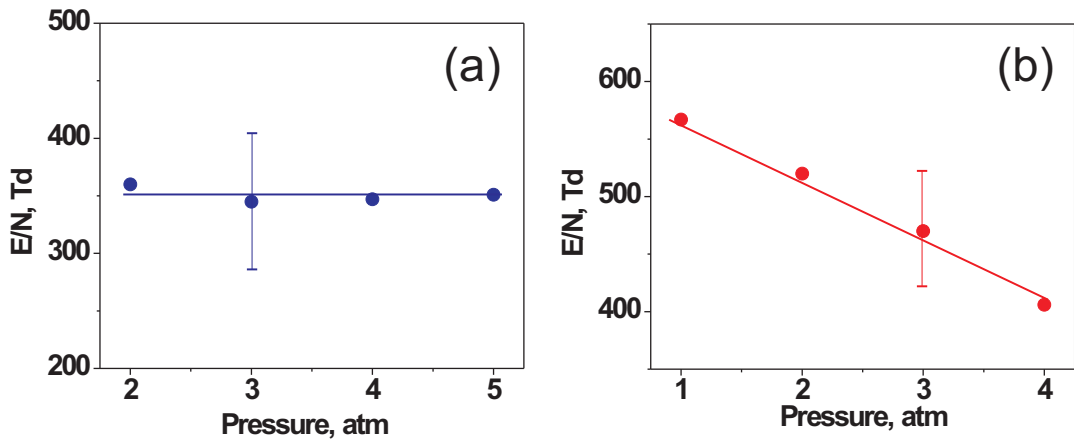
Figure 5.10: Reduced electric field E/N_{eff} *vs* gas pressure, for the edge of the high–voltage electrode (a) and 3 mm apart (b). Values of E/N_{eff} are taken at the time instant corresponding to peak of emission of molecular nitrogen ion at $\lambda = 391.4$ nm. $U = 22$ kV on the electrode.

5.2.3 Electric field measurements at different polarities and ICCD imaging at high HV pulse amplitudes

As far as the final aim of the investigation of high pressure sliding DBD discharge is its application for initiation of combustion, the region of initiat=l parameters has been extended, namely (i) the electric field were measured for different polarities; (ii) the ICCD imaging was performed for a broad range of high-voltage pulse amplitude, from 24 to 60 kV on the high–voltage electrode.

Figure 5.12 represents the dependence of the electric field evolution near the edge of HV electrode at different pressures and different pulse polarities. The experiments were performed is dry air. The voltage amplitude of for the experiments represented by black solid lines was equal to 24 kV on HV electrode. Rise front time was 0.5 ns, pulse duration was 20 ns. Dashed red lines in the fig. 5.12 and 5.13 represent the experiments with +20 kV on HV electrode (front rise time 2 ns, pulse duration 30 ns) at 10 Hz frequency.

The reported results describe the first 5 ns of the discharge. Typically the electric field reaches its maximum and then it decreases to the minimum value and than rises again. It is clearly seen that the maximal electric fields are higher for positive polarity pulses. It must be also noted the maximal electric field decreases with pressure (1–3 atm) and then remains approximately the same for the pressure range 3–5 atm.

Figures 5.13 and 5.14 represent the electric field evolution at 3 mm and 6 mm from HV electrode for different pressures and pulse polarities. Comparison of the Figures shows that the electric field (both maximal and minimal) for positive polarity pulses is higher at 3 mm from HV electrode than at 0 mm. At the same time the electric field corresponding to the negative polarity pulses at 1 atm is lower at 3 mm from HV electrode than at 0 mm from HV electrode. But at 2 atm the situation is opposite, i.e. the electric field is higher at 3 mm from HV electrode than at 0 mm.

Figure 5.14 demonstrates that the highest values of the electric field occur near the
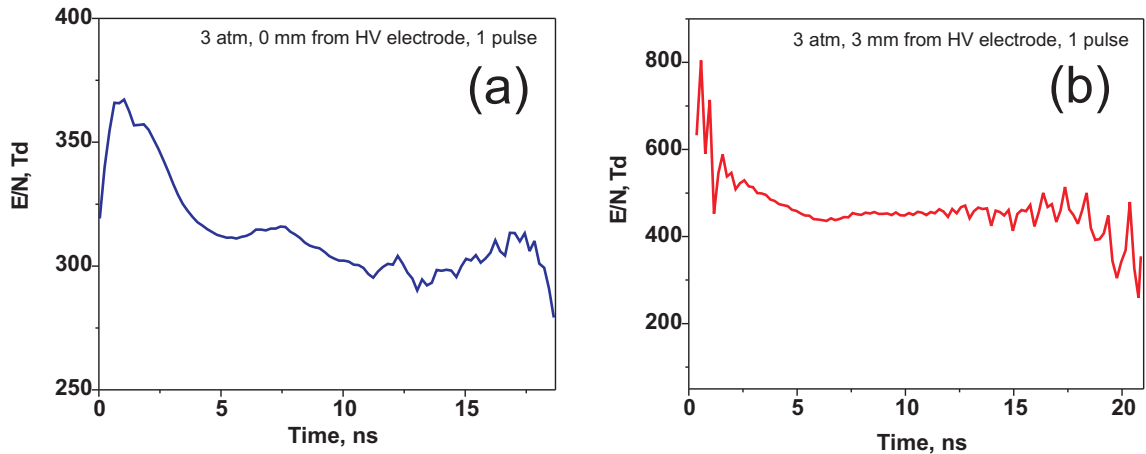
Figure 5.11: Temporal behavior of the reduced electric field for $P = 3$ atm the edge of the high–voltage electrode (a) and 3 mm apart (b). $U = 22$ kV on the electrode.

edge of grounded electrode, i.e. at longer distance from HV electrode. These results confirm that the both maximal and minimal electric fields are higher for positive polarity pulses. It should be also noticed that the electric field at 6 mm from HV electrode for positive polarity at 2 atm is higher than for 1 atm. The dependencies of the electric field at 6 mm for higher pressures are not presented because of low signal of the emission intensity at 391.4 nm.

As it was discussed above, the difference in the electric field values for positive (400-600 Td) and negative (about 200 Td) polarity of the high–voltage electrode can be due to the fact that, according to modern numerical simulations, surface discharge initiated from the negative polarity electrode, does not stick the dielectric surface; plasma parameters in this region are close to parameters of Townsend discharge with high E/N values and low electron densities. As a result, the "summary" of relatively high intensity ion emission from the gap and relatively high molecule emission from the streamer can be observed, giving an "averaged" high value of the electric field.

To follow the discharge transformation with pressure and/or voltage amplitude, ICCD imaging in 250-800 nm spectral range was made for a negative polarity pulse, for synthetic air (24–55 kV amplitude on the electrode, 1–5 atm) and for Ar (24 kV amplitude, 3 and 5 atm pressure). The ICCD camera gate was 2 ns, and the delay between the beginning of the discharge and the ICCD gate was shifted to obtain a time history of the discharge development.

For argon, the emission lasted at least hundreds of nanoseconds; additional spectral analysis is needed to identify the origin of the emission. For air, short life–time emission of the second positive system of molecular nitrogen was observed; the emission pulses behavior with time corresponded to the pulses of current.

Both for air and for nitrogen, the discharge develops in a radial direction, from the high–voltage electrode along the dielectric (PVC) surface. The thickness of the discharge is not higher than a few millimeters.

Typical ICCD images for the discharge in air are given by figure 5.15. Black circle in the center of the image corresponds to the high–voltage electrode 20 mm in diameter. Two forms of the discharge were observed in air: at low pressures and low voltages discharge
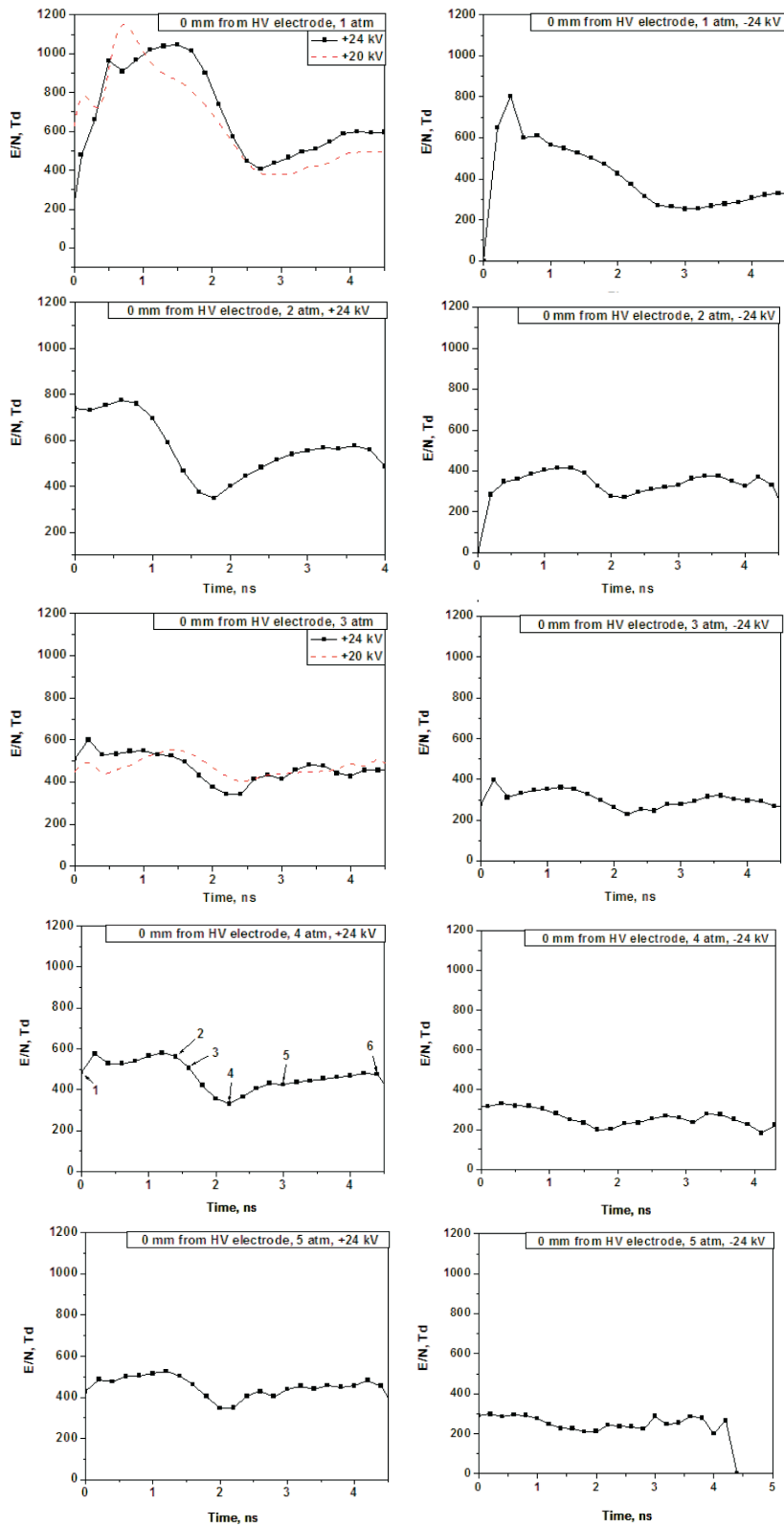
Figure 5.12: Comparison of the electric field evolution near the HV electrode for the different pressures and polarities. Synthetic air.
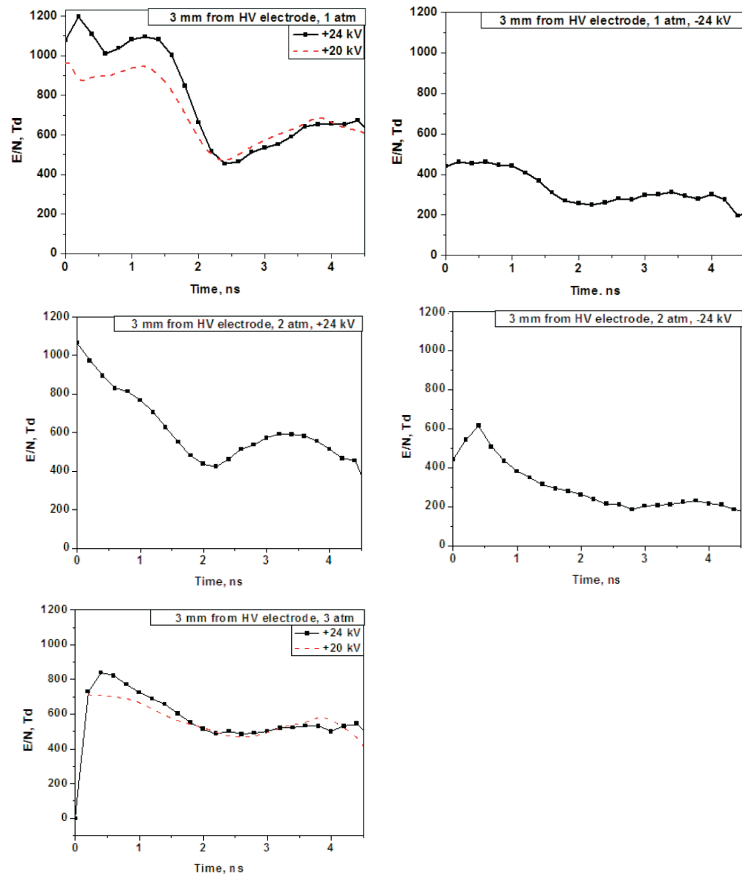
Figure 5.13: Comparison of the electric field evolution at 3 mm from HV electrode for the different pressures and polarities. Synthetic air.
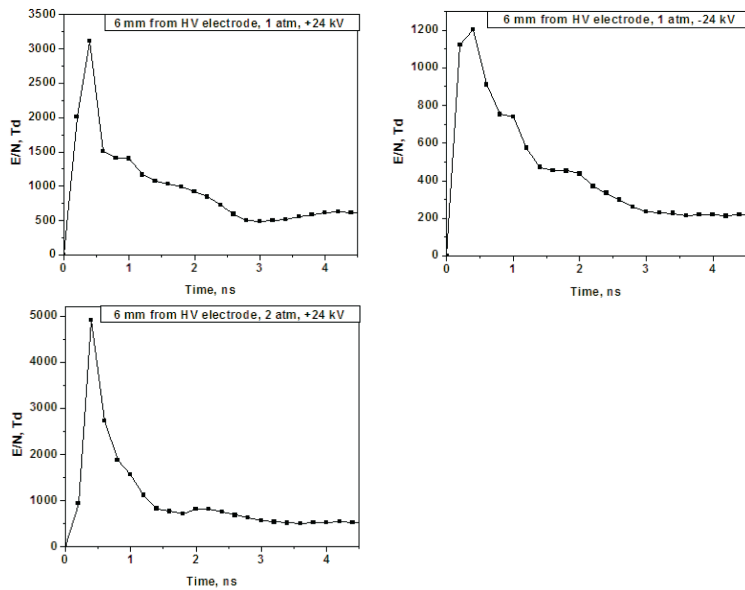
Figure 5.14: Comparison of the electric field evolution at 6 mm from HV electrode for the different pressures and polarities. Synthetic air.
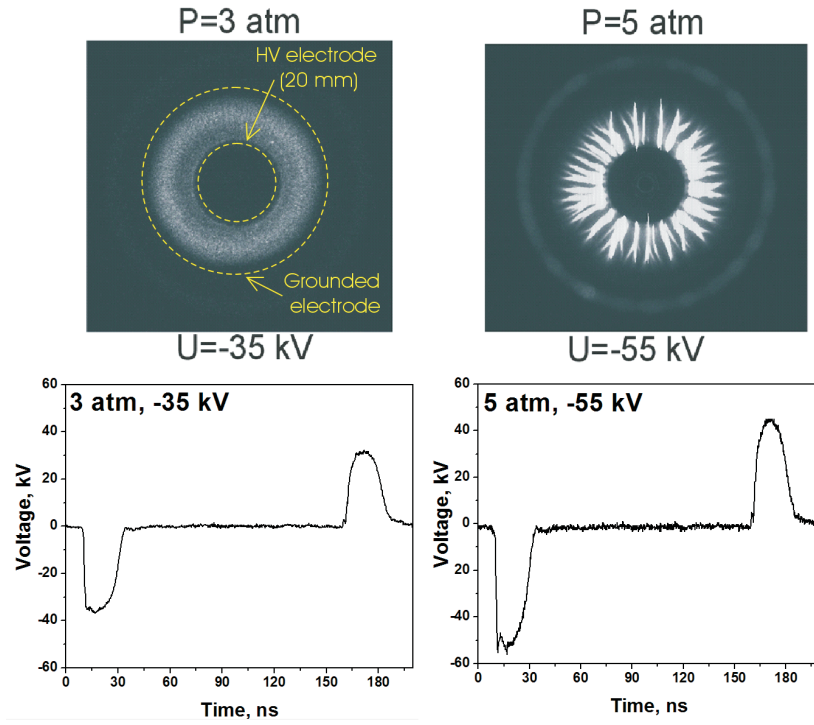
Figure 5.15: ICCD images: diffusive and filamentous modes. Camera gate is 2 ns. Back current shunt oscillograms. Synthetic air.
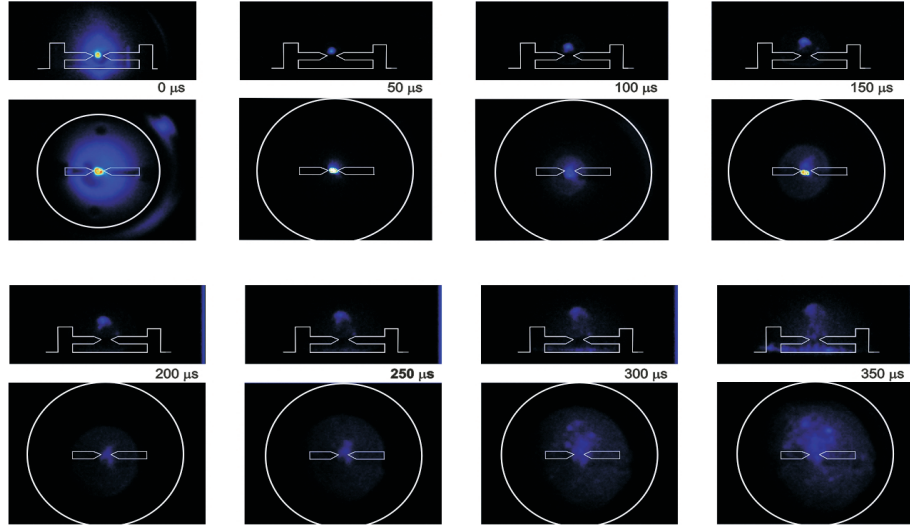
Figure 5.16: ICCD images of C_2H_6:O_2=2:7 mixture ignition by a nanosecond spark discharge [67].

developed as a quasi–uniform structure with a central symmetry relative to the center of the electrode (photo on the right). With pressure/voltage increase, a bright structure has been observed (photo on the left). To check the nature of the discharge, the back current shunt signals were analyzed. It follows (and it is illustrated by oscillograms given by figure 5.15) that there is no electrical gap closing for any of the considered discharge form, so both discharge forms correspond to low–current streamer regime. It is also

74
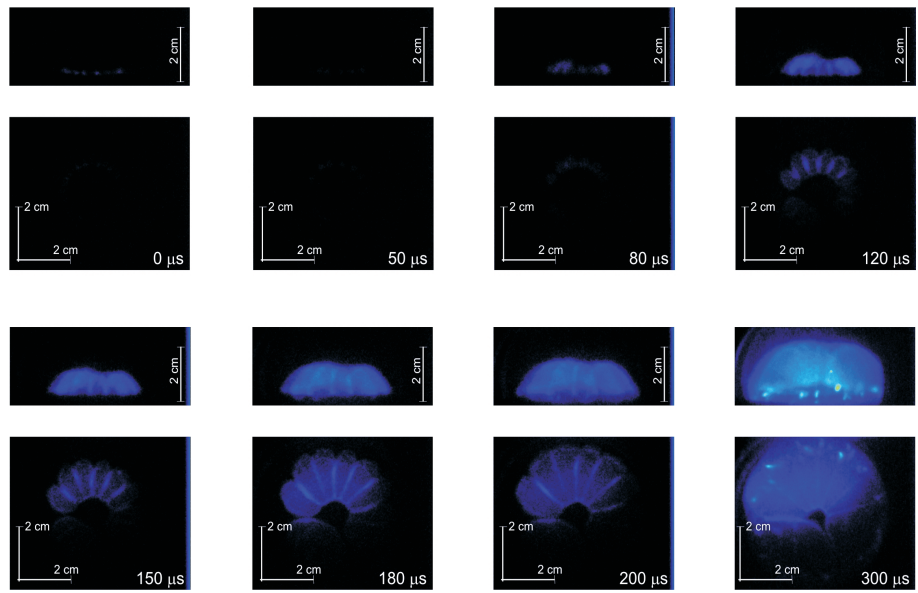
Figure 5.17: ICCD images of C_2H_6:O_2=2:7 mixture ignition by a nanosecond surface dielectric barrier discharge [67].
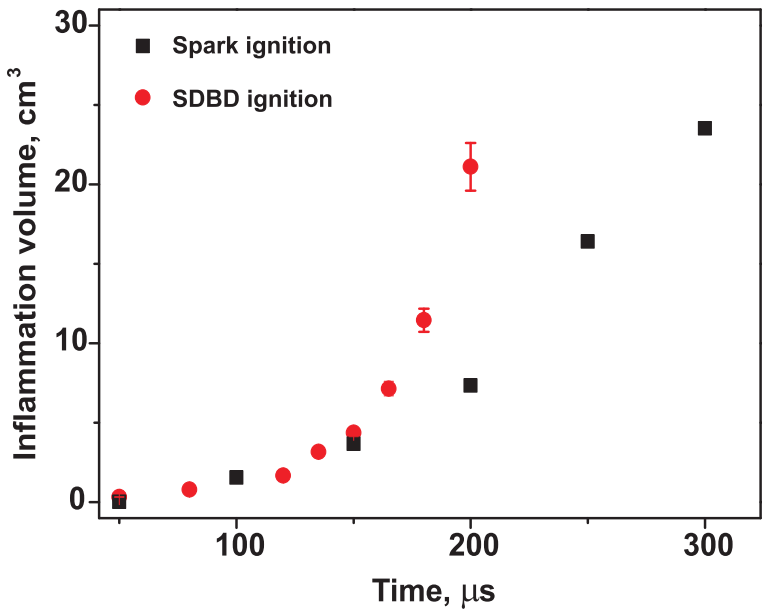
Figure 5.18: Volume of the emission initiated by combustion process, for a nanosecond spark and nanosecond DBD initiated by high–voltage pulse with identical parameters.

important to mote that, at high pressures and high amplitudes, the channels are bright starting from the first nanoseconds of their development from the high–voltage electrode, when the gap is definitely not closed. The threshold for discharge transition to a high emission intensity form depends upon pressure: at 3 atm the transition is observed at –53 kV, at 5 atm it is observed at about –40 kV.

For Ar, experiments at 3 and 5 atm at –24 kV of the voltage amplitude were performed. The discharge in Ar is brighter than discharge in air; the structure of the discharge and

75
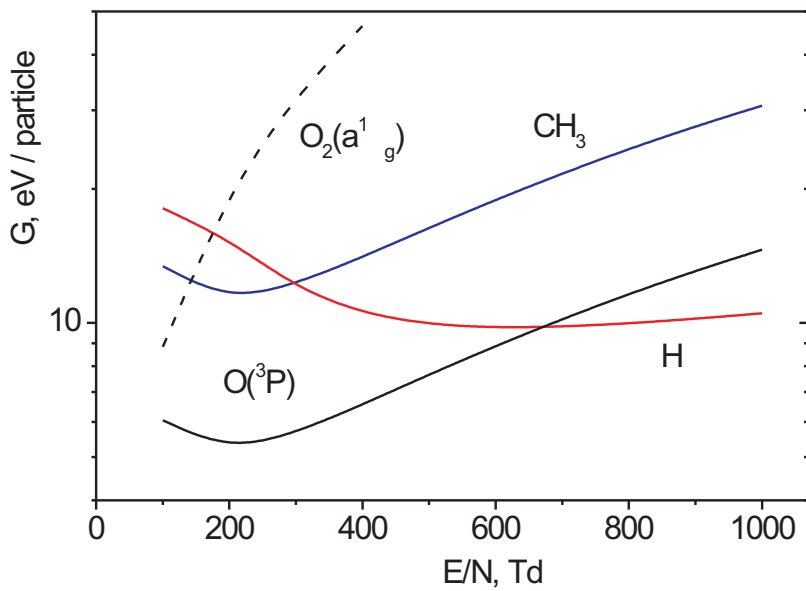
Figure 5.19: Energy efficiency of production of different active species in C_2H_6:O_2 stoichiometric mixture as a function of E/N.
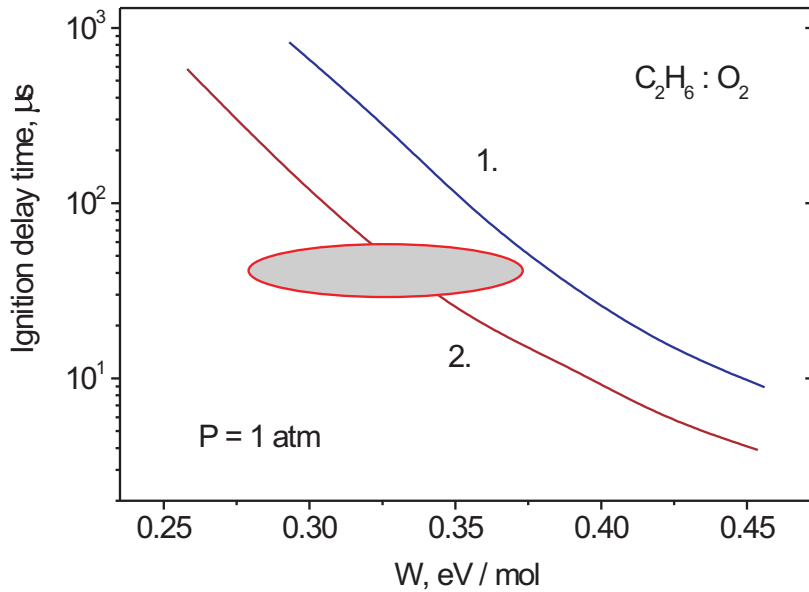
Figure 5.20: Ignition delay time for C_2H_6:O_2 stoichiometric mixture as a function of a specific deposited energy η: 1 — "equilibrium" mode, all energy goes to gas heating at $t = 0$; (2) — "non–equilibrium" mode (see text for explanations). Marked region corresponds to experimental conditions of the present work.

peculiarities of the development are quite similar.

5.2.4 Initiation of combustion at initial ambient temperature. Non–diluted combustible mixture.

To investigate the efficiency of a nanosecond surface DBD to initiate a combustion, stoichiometric C_2H_6:O_2=2:7 mixture at initial pressure $P = 1$ atm was used for the experiments. At ambient temperature, no autoignition is observed. The same shape and amplitude of the high–voltage pulse were used to ignite the spark or sliding DBDs. The energy of the incident pulse was kept the same, 110 mJ. The subsequent development of combustion process was observed with the help of ICCD camera. The sensitivity of the camera was the same for the experiments with spark and surface dielectric barrier discharges.

ICCD images of ignition in spark and DBD configurations of the electrodes are presented in the figures 5.16–5.17. For each frame, side view and top view are presented. As far as ICCD camera allowed to take 16 frames with a programmed time delay, all images correspond to a single–shot event. Time delays are indicated near each pair of images. The camera gate for all the frames is equal to 0.5 μs. The process investigated in the time interval 0–350 μs, so that combustion wave not reaches the chamber walls yet. The combustion front velocity is approximately equal to $7 \cdot 10^3$ cm/s, which is close to the laminar flame velocity in this mixture.

The configuration of electrode system for spark nanosecond discharge is shown in the figure 5.16. The configuration of the DBD is clear from the images presented in the figure 5.17, black circle in the center on the top views represents a high–voltage electrode. Comparison of the figures 5.16 and 5.17 demonstrates that at the stage of the discharge, bright emission spot is observed between the electrodes of the spark gap system while the emission from the surface DBD is hardly seen. This corresponds to the idea that energy deposited in the discharge gap between two open electrodes is significantly higher than the energy deposited in a DBD configuration.

Then, for the two configurations of the electrodes, two different scenaios are observed. For the spark gap configuration, the flame propagates radially from the single point of the initiation located between the electrodes. A "floating" emission spot is observed when look from the side, the spot moves to the top of the image. This effect can be connected to the interaction between the PRESSURE wave and the surface ("basement") of the electrode system. At $t = 300$ μs, local non–uniformities are observed within a combustion wave.

For the surface DBD configuration, combustion starts simultaneously in the manifold of points (see ICCD images for 50 and 80 μs). Comparing the images obtained at later time instants ($180-200$ μs) with the very first image (0 μs) corresponding to the discharge emission, it can be concluded that combustion starts in the centerline of each "petal", and bright emission regions at hundreds of microseconds correspond to the overlapping of separated combustion waves. For the surface DBD, the combustion starts near the surface, and then we observe a "floating" combustion wave enveloping all the surface of the electrode covered with dielectric (the surface where the radially directed streamers were developed).

Comparison of inflammation volumes was performed by integrating the volume over

isolines of emission with the equal intensity. In spite of the higher energy input to the spark discharge, the propagation of the flame front starts in a similar way. But at $t > 150\ \mu$s the flame front initiated by a surface dielectric barrier discharge moves faster flame front initiated by a spark discharge. At $t = 200\ \mu$s, the volume ratio 2.9 is observed.

Under our experimental conditions, combustion starts near the high-voltage electrode (see figure 5.17). The ignition delay time is a few tens of microseconds, that is more than characteristic gas-dynamic time (which is in this case less than $\tau_g = 1 - 2\mu$s), therefore it is possible to calculate ignition at constant pressure. On the other hand the induction time is significantly less than both diffusion and heat conduction times for the channel $R_c = 0.03$ cm under $P = 1$ atm and $T < 1000$ K. This circumstance makes the uniform 0D model appropriate for the calculations.

To describe the discharge and afterglow kinetics in the $C_2H_6 : O_2 = 2 : 7$ mixture, the set of reactions presented in Table 1 was used. Electron impact excitation, ionization and dissociation rates were obtained from two-term approximation of Boltzmann equation with the help of Bolsig+ code. Cross-sections for O_2 and C_2H_6 molecules were taken from [71] and [72] respectively.

Table 5.1: System of reactions including charged and electronically-excited species in $C_2H_6 : O_2 = 2 : 7$ mixture

No	Reaction	k, cm^{-3}/sec	Ref.
R1	$e + O_2 \rightarrow O_2^+ + 2e$	k = k (E/N)	[71]
R2	$e + C_2H_6 \rightarrow C_2H_6^+ + 2e$	k = k (E/N)	[72]
R3	$O_2^+ + C_2H_6 \rightarrow C_2H_6^+ + O_2$	$1.2 \cdot 10^{-9}$	[73]
R4	$O_2^+ + e \rightarrow O(^3P) + O(^1D)$	$2.0 \cdot 10^{-7} \cdot (300/T_e)^{0.7}$	[24]
R5	$C_2H_6^+ + e \rightarrow C_2H_4(v) + 2H$	$7.4 \cdot 10^{-7} \cdot (300/T_e)^{0.5}$	[50]
R6	$e + C_2H_6 \rightarrow e + C_2H_5(v) + H$	k = k (E/N)	[72, 50]
R7	$e + O_2 \rightarrow e + O(^3P) + O(^3P)$	k = k (E/N)	[71]
R8	$e + O_2 \rightarrow e + O(^3P) + O(^1D)$	k = k (E/N)	[71]
R9	$O(^1D) + O_2 \rightarrow O(^3P) + O_2(b^1\Sigma_g,v)$	$3.2 \cdot 10^{-11} \cdot \exp(67/T)$	[24]
R10a	$O(^1D) + C_2H_6 \rightarrow C_2H_5 + OH$	$(0.3)4.4 \cdot 10^{-10}$	[73, 74]
R10b	$O(^1D) + C_2H_6 \rightarrow CH_3O + CH_3$	$(0.7)4.4 \cdot 10^{-10}$	[73, 74]
R11	$e + O_2 \rightarrow e + O_2(A, c, C)$	k = k (E/N)	[71]
R12	$e + O_2 \rightarrow e + O_2(b^1\Sigma_g)$	k = k (E/N)	[71]
R13	$e + O_2 \rightarrow e + O_2(a^1\Delta_g)$	k = k (E/N)	[71]
R14	$O_2(A) + O_2 \rightarrow O_2 + O_2(b^1\Sigma_g,v)$	$2.9 \cdot 10^{-13}$	[24]
R15	$O_2(A) + O(^3P) \rightarrow O_2(b^1\Sigma_g,v) + O(^1D)$	$9.0 \cdot 10^{-12}$	[24]
R16	$O_2(A) + C_2H_6 \rightarrow C_2H_6 + O_2(b^1\Sigma_g,v)$	$> 1.0 \cdot 10^{-12}$ (estimation)	p.w.
R17	$O_2(b^1\Sigma_g) + O_2 \rightarrow O_2(a^1\Delta_g) + O_2(v)$	$4.0 \cdot 10^{-17}$	[75]
R18	$O_2(b^1\Sigma_g) + C_2H_6 \rightarrow O_2(a^1\Delta_g) + C_2H_6(v)$	$3.6 \cdot 10^{-13}$	[75]
R19	$O_2(a^1\Delta_g) + O_2 \rightarrow O_2(v) + O_2(v)$	$2.0 \cdot 10^{-18}$	[75]
R20	$O_2(a^1\Delta_g) + C_2H_6 \rightarrow O_2 + C_2H_6(v)$	$1.8 \cdot 10^{-18}$	[75]
R21	$O_2(a^1\Delta_g) + HO_2 \rightarrow O_2 + HO_2*$	$2.0 \cdot 10^{-11}$	[76]
R22	$O_2(a^1\Delta_g) + H \rightarrow O(^3P) + OH$	$1.3 \cdot 10^{-11} \cdot \exp(-2530/T)$	[76]
R23	$O_2(a^1\Delta_g) + H \rightarrow O_2 + H$	$5.2 \cdot 10^{-11} \cdot \exp(-2530/T)$	[76]
R24	$O_2(v=1) + O(^3P) \rightarrow O_2(v=0) + O(^3P)$	$1.2 \cdot 10^{-12} \cdot (T/300)$	[34]
R25	$O_2(v) + C_2H_4 \rightarrow O_2(v=0) + C_2H_4(v)$	$P \cdot \tau_V = 1.2 \cdot 10^{-7}$ atm·s	[77]
R26	$O_2(v) + C_2H_6 \rightarrow O_2(v=0) + C_2H_6(v)$	$P \cdot \tau_V = 1.2 \cdot 10^{-7}$ atm·s	p.w.
R27	$C_2H_6(v) + C_2H_6 \rightarrow C_2H_6(v=0) + C_2H_6$	$P \cdot \tau_V = 1.5 \cdot 10^{-8}$ atm·s	[78]
R28	$C_2H_5(v) + C_2H_6 \rightarrow C_2H_5(v=0) + C_2H_6$	$P \cdot \tau_V = 1.5 \cdot 10^{-8}$ atm·s	p.w.
R29	$C_2H_4(v) + C_2H_4 \rightarrow C_2H_4(v=0) + C_2H_4$	$P \cdot \tau_V = (1\text{-}2) \cdot 10^{-7}$ atm·s	[78]

A considerable uncertainty should be noted on the the reaction products of electron-ion recombination of the $C_2H_6^+$ ion (reaction (R5) in Table 1) and the dissociation of C_2H_6 by electron impact (R6). In this work, similar to [50], it was assumed that these reactions lead to production of the atomic hydrogen. It should be also noted that in the mixture under consideration fast deactivation of the electronically exited $O(^1D)$ atoms

and $O_2(b^1\Sigma_g^+)$, $O_2(A^3\Sigma_u^+, C^3\Sigma\Delta_u, c^1\Sigma_u^-)$ molecules occurs. As a result, production of $O_2(a^1\Delta_g)$ molecules and vibrational excitation of C_2H_6 and O_2 (reactions (R10, R16, R17), Table 1) is observed. The reactions (R5) and (R6) can be a reason of the significant vibrational excitation of C_2H_4 and C_2H_5 molecules. The vibrational excitation of $O_2(\nu)$ and $C_2H_6(\nu)$ relaxes rapidly to the translational degrees of freedom during VV' - exchange processes and VT - relaxation. Typical time of the vibrational relaxation of $O_2(\nu)$ on C_2H_4 (R25) was measured in [77] for temperatures $T = 430 - 1350$ K. It was assumed here that the reaction (R26) has the same rate as (R25). From the data presented in Table 1, one can see that the relaxation times for $O_2(\nu)$, $C_2H_6(\nu)$, $C_2H_5(\nu)$, $C_2H_4(\nu)$ (see reactions (R24-R29)) are less than 1 μs what is significantly less than τ_g.

The calculated efficiency of production of chemically active particles for the considered gas mixture *vs* reduced electric field E/N is presented in figure 5.19. According to the calculations, more than half of the discharge energy is spent on dissociation. It was assumed that all other energy spent on electronic and vibrational excitation relaxes instantly to the gas heating. The last assumption is valid since a typical relaxation time under our conditions are less than τ_g.

The obtained data were used to calculate the density of chemically active species and the temperature after the nanosecond pulse discharge. The reduced electric field E/N and the specific deposited energy η were the given parameters during the calculations. Two cases were calculated: "equilibrium" mode, when all the energy of the discharge assumed to go directly to gas heating, and "nonequilibrium" mode when the energy goes to gas heating and to dissociation in proportion determined by E/N value.

Figure 5.20 presents calculated ignition delay time for $C_2H_6 : O_2 = 2{:}7$. Curve 1 corresponds to the "equilibrium" mode, that is to a gas preliminary heated by the discharge "without" participation of active species in combustion chemistry, and curve 2 corresponds to the "nonequilibrium" discharge mode for E/N=400 Td. Taking into account the non-equilibrium character of the discharge leads to the noticeable decrease of the induction time.

As it was previously mentioned the induction delay time observed in the experiments for $C_2H_6{:}O_2 = 2{:}7$ mixture is about $\tau_{ind} \approx 30 - 50$ μs. In the "equilibrium" case (discharge energy is "instantly" goes in gas heating) $\tau_{ind} \approx 30$ μs may be achieved with the deposited energy $\eta_{eq} \approx 0.4$ eV/mol. In nonequilibrium case for $E/N = 400$ Td the same time is obtained for $\eta_n \approx 0.35$ eV/mol.

Estimations of the specific deposited energy into the discharge channel give the following results. The total energy deposited in gas is equal to $W = 15$ mJ; the number of channels is $N \approx 15$ and a channel length can be taken equal to $d = 1$ cm. According to measurements [79], a radius of a streamer channel in air at atmospheric pressure is equal to $R_c = 0.025 - 0.03$ cm; similar values are obtained for stoichiometric hydrogen–air mixtures [80] mixtures. The experiments on surface dielectric barrier discharge in air give a similar value for R_c [81]. Supposing the specific deposited energy profile to be Gaussian with the half-width $d_0 = 3.5$ mm, which is similar to observations [13], a value $\eta_0 = 0.27 - 0.38$ eV/mol can be obtained near the electrode. This estimation is in a good agreement with the calculations results.

Thus, the induction delay time of $C_2H_6 : O_2 = 2 : 7$ mixture near the high-voltage electrode is a few tens of microseconds due to the discharge action, i.e. due to chemically active species production and gas heating. To obtain a reasonable agreement between nu-

merical modeling and the experiments, it is necessary to take into account the non–uniform distribution of the deposited energy along the streamer channels with the maximum near the high-voltage electrode.

5.2.5 Initiation of combustion at high initial pressures and moderate (700–1000 K) initial temperature. Preliminary RCM experiments.

One of positive outcomes of the current Project is the beginning of collaboration with Lille University, France (Dr. Pascale Desgroux and Dr. Guillaume Vanhove). Preliminary experiments, were the developed and investigated nanosecond radial surface DBD discharge was used for initiation of combustion at controlled conditions of a rapid compression machine (RCM), have been performed. The RCM combustion chamber was a cylinder 50 mm in diameter and 16 mm in height at Top Dead Center (TDC). Before compression, a gas in the reaction chamber was uniformly heated to a given initial temperatures. A piezoelectric pressure transducer, Kistler 601, was mounted in the side wall of the chamber 8 mm apart from the end plate. The delay between TDC and the discharge initiation was fixed to 2–3 ms, that is was significantly shorter than the autoignition delay time (60 ms and longer) and shorter that typical time of heat losses.
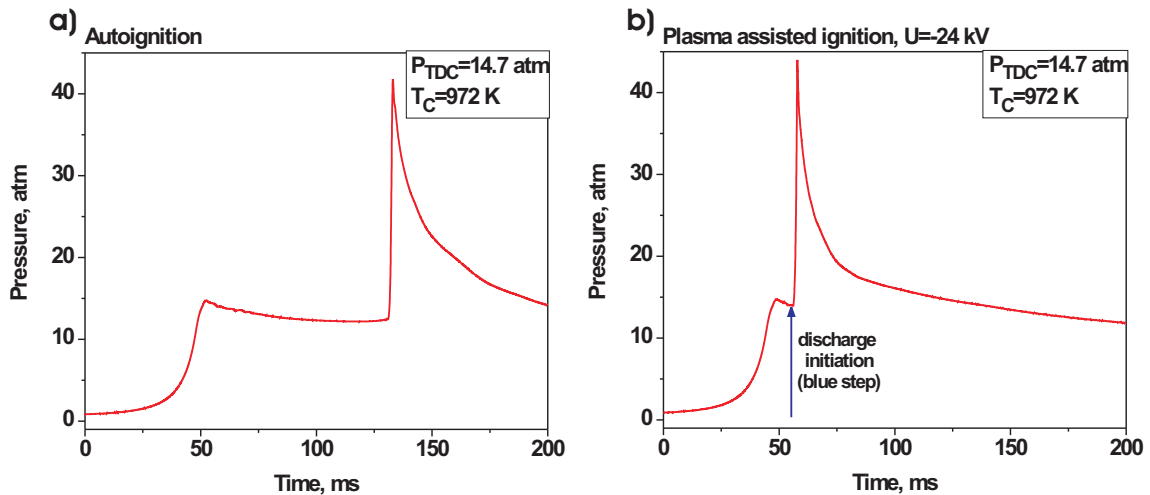
Figure 5.21: Comparison of the a) autoignition and b) plasma assisted ignition. Methane/oxygen stoichiometric mixture diluted by 71 % of argon (obtained in collaboration with Lille University withing French ANR Program).

A typical difference between autoignition and plasma assisted ignition pressure–time profiles is shown in Figure 5.21. It is clearly seen that for plasma assisted ignition, the discharge significantly decreases the ignition delay time, from tens of milliseconds to milliseconds, at typical deposited energy about 0.01–0.05 J. Two effects can be responsible for the observed decrease of the ignition delay time: multi–point ignition at the edge of the high–voltage electrode, caused by both the dissociation and temperature increase, and the following flame propagation; or a relatively volumetric ignition initiated by preliminary

80

quasi-uniform dissociation in the vicinity of the end plate; additional experiments are planned for the visualization of development of the combustion inside the combustion chamber.

5.3 Conclusions

Measurements of electric field in nanosecond pulsed DBD surface discharge of positive polarity in synthetic air in the pressure range of 1—5 atm has been performed. It was demonstrated that in the front of the discharge the electric field is rather high (500 Td and higher), then it decreases during a few nanoseconds but the absolute values remain still high (hundreds of Td) during the discharge.

Comparative measurements of electric field for different polarities of the discharge show that at negative polarity, the electric field values are much lower, about 200 Td. One of the possible explanations is a complex 3D structure of the surface DBD starting from the high–voltage electrode of a positive polarity: a gap between dielectric layer and a streamer can provide high values of electric field measured by emission spectroscopy.

A kinetic mechanism has been proposed to describe the nanosecond discharge action on C_2H_6:O_2 mixture at ambient initial temperature and at 1 atm pressure. The efficiency of a distributed surface DBD initiation of combustion with the production of radicals in the discharge and gas heating due to relaxation of energy from electronically excited species and/or recombination has been compared to the efficiency of thermal ignition for a case when all the energy goes immediately to heating of gas. It was shown that the ignition by nonequilibrium plasma is more efficient.

Preliminary experiments comparing autoignition and ignition by a nanosecond surface dielectric barrier discharge (SDBD) at conditions of high pressures and moderate temperatures have been performed as an outcome of the Project. It is shown that, at 10–50 mJ of deposited energy, significant, more than an order of magnitude, decrease of ignition delay time is possible.

Bibliography

[1] Popov N A 2001 Investigation of the mechanism for rapid heating of nitrogen and air in gas discharge *Plasma Phys. Rep.* **27(10)** 886

[2] Starikovskaia S M and Starikovskii A Yu, Plasma-Assisted Ignition and Combustion, in: Handbook of Combustion, Vol. 5: New Technologies, Lackner M, Winter F, Agarwal A K, eds. WILEY VCH Verlag GmbH & Co. KGaA, p. 71

[3] Adamovich I V, Choi I, Jiang N, Kim J–H, Keshav S, Lempert W R, Mintusov E, Nishihara M, Samimy M and Uddi M 2009 Plasma assisted ignition and high–speed flow control: non–thermal and thermal effects *Plasma Sources Sci. Technol.* **18** 034018 (13pp)

[4] Starikovskii A Yu, Nikipelov A A, Nudnova M M and Roupassov D V 2009 SDBD plasma actuator with nanosecond pulse–periodic discharge *Plasma Sources Sci. Technol* **18** 034015(17 pp)

[5] Miles R B, Opaits D F, Shneider M N, Zaidi S H and Macheret S O 2009 Non–thermal atmospheric pressure plasmas for aeronautic applications *Eur. Phys. J. Appl. Phys.* **47** 22802

[6] Aleksandrov N L, Kindysheva S V, Kosarev I N, Starikovskaia S M, Starikovskii A Yu 2009 Mechanism of ignition by non–equilibrium plasma 2009 *Proc. of the Combustion Institute* **32** 205

[7] Adamovich I V, Choi I, Jiang N, Kim J–H, Keshav S, Lempert W R, Mintusov E, Nishihara M, Samimy M and Uddi M 2009 Repetitively pulsed nonequilibrium plasmas for magnetohydrodynamic flow control and plasma–assisted combustion *Plasma Sources Sci. Technol.* **18** 034018 (13pp)

[8] Stancu G D, Kaddouri F, Lacoste D A and Laux C O Atmospheric pressure plasma diagnostics by OES, CRDS and TALIF 2010 *J. Phys. D: Appl. Phys.* **43** 124002 (10pp)

[9] Ono R, Teramoto Y and Oda T 2010 gas density in a pulsed positive streamer measured using laser shadograph *J Phys D.: Appl. Phys.* **43** 345203 (7pp)

[10] Kosarev I N, Aleksandrov N L, Kindysheva S V, Starikovskaia S M and Starikovskii A Yu 2008 Kinetics of ignition of saturated hydrocarbons by nonequilibrium plasma: CH_4–containing mixtures *Comb. and Flame* **154** 569

[11] Starikovskaia S M, Allegraud K, Guaitella O, Kosarev I N, Mintusov E I, Pendleton S J, Popov N A, Sagulenko P N, Rousseau A 2010 Surface discharges: possible applications for plasma–assisted ignition and electric field measurements *Proc. of 48th AIAA Aerospace Sciences Meeting, 4–7 January 2010, Orlando, Florida*, AIAA 2010–1587

[12] A. Flitti and S. Pancheshnyi S 2009 Gas heating in fast pulsed discharges in N_2-O_2 mixtures *Eur. Phys. J. Appl. Phys.* **45** 21001

[13] Aleksandrov N L, Kindusheva S V, Nudnova M M and Starikovskii A Yu 2010 Mechanism of ultra–fast heating in a non–equilibrium weakly ionized air discharge plasma in high electric fields *J. Phys. D: Appl. Phys.* **43** 255201(19 pp)

[14] Anokhin E M, Starikovskaia S M and Starikovskii A Yu 2004 Energy transfer in hypersonic plasma flow and flow structure control by low temperature nonequilibrium plasma *42nd AIAA Aerospace Sciences Meeting and Exhibit (Reno, NV, 710 January 2004)* paper AIAA-2004-674

[15] Vasilyak L M, Kostyuchenko S V, Kudryavtsev N N and Filyugin I V 1994 High–speed ionization waves at an electric breakdown *Phys.–Uspekhi* **163** 263

[16] Starikovskaia S M, Anikin N B, Pancheshnyi S V, Zatsepin D V and Starikovskii A Yu 2001 Pulsed breakdown at high overvoltage: development, propagation and energy branching *Plasma Sources Sci. Technol* **10** 344

[17] Anikin N B, Starikovskaia S M and Starikovskii A Yu 1998 The development of high velocity ionization wave in systems with various configuration of high–voltage electrodes *High Temperature* **36(6)** 969

[18] Mintoussov E, Lacoste D A, Pendleton S J, Popov N A, Stancu G D, Laux C O and Starikovskaia S M, *Proc. of ESCAMPIG 2010*, P1.39

[19] Anikin N B , Starikovskaia S M and Starikovskii A Yu 2002 Polarity effect of applied pulse voltage on the development of uniform nanosecond gas breakdown J. Phys. D: Appl. Phys. **35** 2785

[20] Pancheshnyi S V, Starikovskaia S M and Starikovskii A Yu 1999 Population of nitrogen molecule electron states and structure of the fast ionization wave *J. Phys. D: Appl. Phys.* **32** 2219

[21] Laux C O 2002 Radiation and nonequilibrium collisional–radiative models *in: Physico–Chemical Modeling of High Enthalpy and Plasma Flows* (von Karman Institute Lecture Series 2002–07, eds. Fletcher D, Charbonnier J–M, Sarma G S R and Magin T, Rhode–Saint–Genese, Belgium)

[22] Panchesnyi S V, Starikovskaia S M and Starikovskii A Yu 2000 Collisional deactivation of $N_2(C^3\Pi_u, v = 0, 1, 2, 3)$ states by N_2, O_2, H_2 and H_2O molecules *Chemical Physics* **262** 349

[23] Starikovskaia S M, Kukaev E N, Kuksin A Yu, Nudnova M M and Starikovskii A Yu 2004 Analysis of spatial uniformity of the combustion of a gaseous mixture initiated by a nanosecond discharge *Comb. and Flame* **139** 177

[24] Kossyi I A, Kostinsky A Y, Matveev A A and Silakov V P 1992 Kinetic scheme of the non-equilibrium discharge in nitrogen–oxygen mixtures *Plasma Sources Sci.Technol.***1(3)** 207

[25] Popov N A 2010 Evolution of the negative ion composition in the afterglow of a streamer discharge in air *Plasma Phys. Rep.* **36(9)** 828

[26] Hagelaar G J and Pitchford L C 2005 Solving the Boltzmann equation to obtain electron transport coefficients and rate coefficients for fluid models it Plasma Sources Sci. Technol. **14** 722

[27] Phelps A V and Pitchford L C 1985 Anisotropic scattering of electrons by N_2 and its effect on electron transport *Phys. Rev. A.* **31(5)** 2932

[28] Popov N A 2010 Mechanism of fast gas heating in nitrogen–oxygen discharge plasma *J. Phys. D: Appl. Phys.* (submitted)

[29] Aleksandrov N L and Kochetov I V 1987 Influence of vibrational excitation on rates of electronic processes in weakly ionized plasma of molecular gases and gas mixtures *Fizika Plazmy* **25(6)** 1062 (In Russian)

[30] Herron J T 1999 Evaluated chemical kinetics data for reactions on $N(^2D)$, $N(^2P)$, and $N_2(A^3\Sigma_u^+)$ in the gas phase *J. Phys. Chem. Ref. Data.* **28(5)** 1453

[31] Florescu A I and Mitchell J B A 2006 Dissociative recombination *Physics Reports* **430** 277

[32] Cao Y S and Johnsen R 1991 Recombination of N_4^+ ions with electrons *J. Chem. Phys.* **95** 7356

[33] Slovetskii D I 1980 *Mechanisms of Chemical Reactions in Nonequilibrium Plasma* (Moscow: Nauka) (in Russian)

[34] Capitelli M, Ferreira C M, Gordiets B F and Osipov A I 2000 *Plasma kinetics in atmospheric gases* (Springer)

[35] Golde M F and Moyle A M 1985 Study of the products of the reactions of $N_2(A^3\Sigma_u^+)$: the effect of vibrational energy in $N_2(A^3\Sigma_u^+)$ *Chem. Phys. Lett* **117** 375

[36] Piper L G 1987 Quenching rate coefficients for $N_2(a'^1\Sigma_u^-)$ *J. Chem. Phys.* **87** 1625

[37] Popov N A 2006 Simulation of a longitudinal glow discharge in a hot air flow at atmospheric pressure *Plasma Phys. Rep.* **32** 237

[38] Aleksandrov N L, Dyatko N A and Kochetov I V 1995 Rate of inelastic electron processes in a weakly ionized plasma in a nonstationary electric field *Plasma Physics Reports* **21(9)** 763

[39] Mintoussov E I, Pendleton S J, Gerbault F G, Popov N A, Starikovskaia S M 2011 Fast gas heating in nitrogen–oxygen discharge plasma. II. Energy exchange in the afterglow of a volume nanosecond discharge at moderate pressures *J. Phys. D: Appl. Phys.* **44** 285202 (13pp)

[40] Popov N A 2011 Fast gas heating in nitrogen–oxygen discharge plasma. I. Kinetic mechanism. *J. Phys. D: Appl. Phys.* **44** 285201 (16pp)

[41] Anikin N B, Starikovskaia S M, and Starikovskii A Yu 2001 Uniform nanosecond gas breakdown of negative polarity: initiation form electrode and propagation in molecular gases *J. Phys. D: Appl. Phys.* **34** 177—188

[42] G.D. Stancu, M. Janda, F. Kaddouri, D.A. Lacoste, C.O. Laux, "Time–resolved CRDS measurements of the $N_2(A^3\Sigma_u^+)$ density produced by nanosecond discharges in atmospheric pressure nitrogen and air", J. Phys. Chem. A, 114 (1), (2010), 201.

[43] K.W. Busch, M.A. Busch, 1999, Cavity ring–down spectroscopy an ultrafast absorption measurement technique, ACS symposium series.

[44] A.P. Yalin, R.N. Zare, C.O. Laux, C.H. Kruger, 2002, Appl. Phys. Lett. 81, 8, 1408.

[45] S.S. Brown, A.R. Ravishankara, H. Stark, 2000, J. Phys. Chem. A, 104, 7044.

[46] P. Zalicki and R.N. Zare, Cavity ring–down spectroscopy for quantitative absorption measurements, J. Chem. Phys., 102(7), (1995), 2708.

[47] Starikovskaia S M, Starikovskii A Yu 2010 Plasma assisted ignition and combustion*In: Handbook of Combustion* by Lackner M (Ed.), Winter F (Ed.), Agarwal A K (Ed.), Wiley-VCH, ISBN; 978-3527324491

[48] Pancheshnyi S V, Lacoste D A, Bourdon A, Laux C O 2006 Ignition of propane-air mixtures by a repetitively pulsed nanosecond discharge *IEEE Trans. on Plasma Science* **34 (6)** 2478—2487

[49] Bentaleb S, Tardiveau P, Jorand F, Jeanney P, Magne L, Pasquiers S 2011 Ignition of $N_2/O_2/C_3H_8$ mixtures by a single nanosecond pulsed discharge at atmospheric pressure, *Proc. of International Conference on Plasma Physics (ISPC)* Philadelphia, USA, 4—9 July 2011

[50] Kosarev I N, Aleksandrov N L, Kindysheva S V, Starikovskaia S M, Starikovskii A Yu, 2009 Kinetics of ignition of saturated hydrocarbons by nonequilibrium plasma: C_2H_6– to C_5H_{12}–containing mixtures *Combustion and Flame* **156** 221–233

[51] Starikovskiy A, Aleksandrov N 2011 Plasma–assisted ignition and combustion (2011) *In: Aeronautics and Astronautics* Ed by: Max Mulder. ISBN, 978-953-307-473-3

[52] Markus D, Hallermann A, Langer T, Paul M, Lienesch F 2011 Experimental investigation of the ignition by repetitive streamer discharges, *42nd AIAA Plasmadynamics and Lasers Conference*, 27–30 June 2011, Honolulu, Hawaii, AIAA 2011—3451

[53] Singleton D, Pendleton S J, Gundersen M A 2011 The role of non–thermal transient plasma for enhanced flame ignition in C_2H_4—air *J. Phys. D: Appl. Phys.* **44** 022001 (6pp)

[54] Pilla G, Galley D, Lacoste D A, Lacas F, Veynante D and Laux C O 2006 Stabilization of a turbulent premixed flame using a nanosecond repetitively pulsed plasma *IEEE Trans. on Plasma Sci.* **34(6)**, 2471—77

[55] Starikovskaia S M, Allegraud K, Guaitella O and Rousseau A 2010 On electric field measurements in surface dielectric barrier discharge *J. Phys. D.: Appl. Phys.* **43** 124007 (5pp)

[56] Pancheshnyi S V, Starikovskaia S M and Starikovskii A Yu 1998 Measurements of rate constants of the N_2 ($C^3\Pi_u$, $v' = 0$), and N_2^+ ($B^2\Sigma_u^+$, $v' = 0$) deactivation by N_2, O_2, H_2, CO and H_2O molecules in afterglow of the nanosecond discharge *Chemical Physics Letters* **29** 523–7

[57] Paris P, Aints M, Valk F, Plank T, Haljaste A, Kozlov K V, and Wagner H–E 2005 Intensity ratio of spectral bands of nitrogen as a measure of electric field strength in plasmas*J. Phys. D: Appl. Phys.* **38** 3894

[58] Paris P, Aints M and Valk F, 2009 Collisional quenching rates of $N_2^+(B^2\Sigma_g^+, v = 0)$, *Book of contributed papers of 17th Symposium on Application of Plasma Processes and Visegrad Workshop on Research of Plasma Physics* Liptovsky Jan, Slovakia, 17–22 January 2009, pp. 227—8

[59] Pancheshnyi S 2006 Comments on "Intensity ratio of spectral bands of nitrogen as a measure of electric field strength in plasmas", *J. Phys. D: Appl. Phys.* **39** 1708–10

[60] Paris P, Aints M, Valk F, Plank T, Haljaste A, Kozlov K V and Wagner H–E 2006 Reply to comments on "Intensity ratio of spectral bands of nitrogen as a measure of electric field strength in plasmas" *J. Phys. D: Appl. Phys.* **39** 2636–39

[61] Creyghton Y L M 1994 Pulsed positive corona discharges *PhD Thesis, Eindhoven University of Technology*

[62] Dyakov A F, Bobrov Yu K, Bobrova L N and Yourguelenas Yu V 1998 Streamer discharge plasma parameters determination in air on a base of a measurement of radiation of the molecular bands of nitrogen *Physics and technology of Electric Power Transmission* (Moscow: MPEI) pp. 219—33 (in Russian)

[63] Kim Y, Hong S H, Cha M S, Song Y–H and Kim S J 2003 Measurements of electron density by emission spectroscopy in pulsed corona and dielectric barrier discharges *J. Adv. Oxid. Technol.* **6** 17–22

[64] Starikovskii A Yu, Nikipelov A A, Nudnova M M and Roupassov D V 2009 SDBD plasma actuator with nanosecond pulse–periodic discharge *Plasma Sources Sci. Technol* **18** 034015(17 pp)

[65] Nudnova M M, Aleksandrov N L, Starikovskii A Yu, 2010 Influence of the polarity on the properties of a nanosecond surface barrier discharge in atmospheric pressure air *Fizika plasmu* **36(1)** 94—103

[66] Allegraud K, Guaitella O and Rousseau A 2007 Spatio–temporal breakdown in surface DBDs: evidence of collective effect J. Phys. D: Appl. Phys. **40** 7698—7706

[67] EOARD/CRDF Project RUP1–1513–MO–06, PIs Starikovskaia/Kosarev, 8th Quarter Report, 2009.

[68] Raizer Yu P 1991 Gas Discharge Physics (Berlin: Springer)

[69] Soloviev V R, Krivtsov V M, Konchakov A M and Malmuth N D 2008 Surface barrier discharge simulation in air for constant applied voltage it AIAA Meeting (Reno, NV, January 2008) AIAA 2008-1378

[70] Soloviev V R, Krivtsov V M, Surface barrier discharge modelling for aerodynamic applications 2009 *J. Phys. D: Appl. Phys.* **42** 125208 (13pp)

[71] Braginsky O V, Vasilieva A N, Klopovskiy K S, Kovalev A S, Lopaev D V, Proshina O V, Rakhimova T V, Rakhimov A T 2005 Singlet oxygen generation in O$_2$ flow excited by RF dis-charge *J. Phys. D: Appl. Phys.* **38** 3609–3625

[72] Hayashi M 1987 Electron collision cross sections for molecules determined from beam and swarm data // in: Pitchford L C, McCoy B V, Chutjian A, Trajmar S (Eds.), Swarm studies and in-elastic electronmolecule collisions *Springer-Verlag, New York* 167–187

[73] Magne L, Pasquiers S, Gadonna K, Jeanney P, Blin-Simiand N, Jorand F, Postel C 2009 OH kinetic in high-pressure plasmas of atmospheric gases containing C2H6 studied by abso-lute measurement of the radical density in a pulsed homogeneous discharge *J. Phys. D: Appl. Phys.* **42** 165203–165219

[74] Matsumi Y, Tnokura K, Inagaki Y, Kawasaki M 1993 Isotopic branching ratios and translational energy release of H and D atoms in reaction of O(^{1}D) atoms with alkanes and alkyl chlorides *J. Phys. Chem.* **97** 6816–6821

[75] Morozov I I, Temchin S M 1990 Kinetics of reactions of singlet oxygen in gaseous phase *Khimia Plasmy. M.: Energoatomizdat* **16** 39–67 (in Russian)

[76] Popov N A 2011 Effect of singlet oxygen O$_2$(a$^1\Delta_g$) molecules produced in gas dis-charge plasma on the ignition of hydrogen-oxygen mixtures *Plasma Sources Sci. Technol.* **20** 045002

[77] White D R 1965 Vibrational relaxation of oxygen by methane, acetylene, and ethy-lene *J. Chem. Phys.* **42** 2028–2032

[78] Holmes R, Jones G R, Pusat N 1964 Vibrational relaxation in propane, propylene and ethane *J. Chem. Phys.* **41** 2512–2516

[79] Pancheshnyi S, Nudnova M, Starikovskii A 2005 Development of a cathode-directed streamer discharge in air at different pressures: Experiment and comparison with direct numerical simulation *Phys. Rev. E.* **71** 016407–016418

[80] Langer T, Markus D, Lienesch F, Maas U 2010 Streamer discharges caused by high-frequency voltage leading to ignition of hydrogen/air mixtures *Combustion Science and Technology* **182** 1718–1734

[81] Sokolova M V, Kozlov K V, Krivov S A, Samoilovich V G, Tatarenko P A 2009 Investigation of sliding discharge emission in dry air *Pisma v Zhurnal Technicheskoi Fizik* **35** 22–28

Chapter 6

Summary

To study a fast gas heating, that is fast relaxation of energy from electronic to translational degrees of freedom, the experimental studies of parameters of a spatially uniform nanosecond discharge in air in a pressure range $3-9$ mbar have been made. Temporal behavior of the discharge current, reduced electric field E/N and specific deposited energy were measured. The data was used for development and verification of a numerical model of kinetics in the discharge. Due to the relatively small diameter of the discharge tube, the current density was high (160-200 A/cm^2). This provided high specific deposited energy $(0.1-0.13$ eV/molecule) at reduced electric fields of $200-400$ Td.

The evolution of gas temperature has been studied in the discharge and in the afterglow. The temperature was measured from the rotational structure of the second positive system of molecular nitrogen. The data in the afterglow was obtained with the help of additional nanosecond pulses of relatively low intensity. Thus, fast gas heating in an N_2:O_2=4:1 mixture has been measured for the first time with well–controlled electric fields and specific energy input during the discharge stage for $E/N = 200-400$ Td. The results prove that the main energy input to gas heating takes place at time typical for quenching of electronically excited states of molecular nitrogen.

The results of numerical calculations based on a given experimental electric current profile versus time are presented. The calculations were carried out in the framework of a 0D kinetic model, taking into account the detailed kinetics of charged and excited species. The calculated behavior of the electric field and specific deposited energy is in good agreement with the experiments, which proves that the model describes correctly electric field and processes of ionization.

The main energy release in the model takes place in reactions of quenching of electronically excited nitrogen molecules, such as $N_2(A^3\Sigma_u^+, B^3\Pi_g, C^3\Pi_u, a'^1\Sigma_u^-)$ by oxygen, quenching of excited $O(^1D)$ atoms by N_2, and in reactions of nitrogen and oxygen dissociation by electron impact. These processes provide more than 80% of total gas heating. An agreement between experimental data and results of calculations of gas temperature has been obtained for pressures 3, 6 and 9 mbar. The observed temperature increase in the afterglow is connected with the relaxation of electronic excitation, namely relaxation of $O(^1D)$ and $N(^2D)$ atoms and $N_2(A^3\Sigma_u^+, B^3\Pi_g, C^3\Pi_u, a'^1\Sigma_u^-)$ molecules. Typical times of these reactions do not exceed a few microseconds, which is why under our experimental conditions the main energy relaxation takes place during $50-100$ microseconds. During this time, about 24% of the discharge energy goes to fast gas heating.

The experimental data on fast ionization wave (FIW) development in capillary discharge have been obtained to verify the developed model of fast gas heating under the conditions of high electric field and spatially uniform discharge. Experiments have been performed in synthetic air for gas pressures between 5 and 50 mbar with more broad observations of the discharge itself, between 1 and 850 mbar. The data demonstrate significant increase of rotational temperature in the afterglow, $1-2$ μs after the discharge. Electric field values reach 300–500 Td in the discharge front and 100–200 Td after the front. Velocity of the ionization front propagation is equal to 1.3–1.4 cm/ns.Data on incident, transmitted and reflected current, electric field and temperature increase were obtained for different gas pressures. A model of the fast gas heating, developed for peculiar conditions of fast energy release in the discharge and strong dissociation degree, is verified on the experimental data. A good coincidence with the measured gas temperatures is shown for a consequent pulses for different gas pressures. The obtained data, together with developed kinetic model, give a basis for description of the fast gas heating by short pulse discharges at high electric fields and high energy release at moderate pressures and high dissociation degree.

The experimental setup and diagnostic system were suggested, constructed and adjusted for cavity ring–down measurements of metastable stages of nitrogen in the afterglow of a nanosecond discharge. Preliminary CRDS experiments demonstrate that $N_2(A^3\Sigma_u^+,$ $v = 0)$ concentration decay in nitrogen occurs significantly slower than in the air because of different kinetic mechanisms. Absolute data are obtained for $N_2(A^3\Sigma_u^+, v = 0)$ densities, reative data are available for $v = 1 - 3$.

Measurements of electric field in nanosecond pulsed DBD surface discharge of positive polarity in synthetic air in the pressure range of 1—5 atm has been performed. It was demonstrated that in the front of the discharge the electric field is rather high (500 Td and higher), then it decreases during a few nanoseconds but the absolute values remain still high (hundreds of Td) during the discharge. Comparative measurements of electric field for different polarities of the discharge show that at negative polarity, the electric field values are much lower, about 200 Td. One of the possible explanations is a complex 3D structure of the surface DBD starting from the high–voltage electrode of a positive polarity: a gap between dielectric layer and a streamer can provide high values of electric field measured by emission spectroscopy.

A kinetic mechanism has been proposed to describe the nanosecond discharge action on C_2H_6:O_2 mixture at ambient initial temperature and at 1 atm pressure. The efficiency of a distributed surface DBD initiation of combustion with the production of radicals in the discharge and gas heating due to relaxation of energy from electronically excited species and/or recombination has been compared to the efficiency of thermal ignition for a case when all the energy goes immediately to heating of gas. It was shown that the ignition by nonequilibrium plasma is more efficient. Preliminary experiments comparing autoignition and ignition by a nanosecond surface dielectric barrier discharge (SDBD) at conditions of high pressures and moderate temperatures have been performed as an outcome of the Project. It is shown that, at 10–50 mJ of deposited energy, significant, more than an order of magnitude, decrease of ignition delay time is possible.

Chapter 7

Acknowledgements

List of Figures